# PERIODIC REVERSE FLOW IN MICROCHANNEL EVAPORATORS

BY

HUIZE LI

DISSERTATION

Submitted in partial fulfillment of the requirements
for the degree of Doctor of Philosophy in Mechanical Engineering
in the Graduate College of the
University of Illinois at Urbana-Champaign, 2017

Urbana, Illinois

Doctoral Committee:

Research Professor Predrag S. Hrnjak, Chair
Professor Anthony M. Jacobi
Adjunct Assistant Professor Stefan Elbel
Professor J. Craig Dutton
Associate Professor Davide Del Col, University of Padova

# Abstract

Periodic flow reversal which is associated with boiling instabilities is a very commonly seen phenomenon in small scale heat removal applications, for instance, microchannel heat sinks for cooling of electronics. Due to the industry's strict requirement for thermal stability, previous research on flow instabilities in microchannels has been largely focused on heat sinks for electronic cooling. There is a lack of understanding of the effect of flow reversal in microchannel heat exchangers, which are used in air conditioning and refrigeration applications.

This thesis first presents the visualization of flow reversal in a microchannel as part of a realistic automotive evaporator. The flow regimes inside of the microchannel are recorded under both two phase feeding and liquid only feeding modes. In the two-phase feeding mode, churn, bubbly/slug, and annular flows occur alternatively, but the period of each flow regime is not constant. Flow reversal is only witnessed occasionally in the bubbly/slug flow regime. In the liquid feeding mode, only liquid and bubbly/slug flows are observed. Reverse flow occurs periodically. The duration of flow reversal is much shorter in the two-phase feeding mode than in the liquid feeding mode. Most likely it is due to higher upstream resistance caused by two-phase refrigerant feeding.

After confirming the existence of flow reversal in microchannel heat exchangers which are used in air conditioning applications, this thesis presents a newly developed mechanistic model of bubble dynamics in a single microchannel, which demonstrates how flow reversal is generated. The comparison between high-speed visualization of in-channel flow regimes and simulation results shows that this model is capable of capturing the transient flow regime and slug velocity inside of a single microchannel and predicting flow reversal. The model quantitatively demonstrates the mechanism of flow reversal. Within one periodic cycle, the evolution of flow regime, pressure distribution along channel length and mass flux at tube inlet are well correlated with each other. The local

pressure peak caused by the build-up of downstream flow resistance can cause a positive pressure gradient, which induces flow reversal.

In the third part of the thesis, the effects of channel geometries on flow reversal are presented. Multiple evaporators with different geometries are tested using R134a as the refrigerant. In each evaporator, the reversed vapor flow is vented out of the inlet header and the flow rate is measured. It has been found experimentally that under the same heat flux, superheat and channel length, the microchannel evaporator with smaller diameter generates more reversed vapor flow (per unit mass flow rate of supplied liquid refrigerant) at a higher frequency. A simulation generated by the aforementioned mechanistic model under the same condition demonstrates that smaller diameter creates more rapid growth of vapor slugs and allocates more flow resistance to the downstream section. As a result, the incoming flow is quickly decelerated and the positive pressure gradient ends up covering larger upstream areas, all of which leads to more vapor flow reversal at a higher frequency. Experiments also show that the microchannel evaporator with longer tubes (when diameter is the same) produces less reversed vapor flow (per unit mass flow rate of supplied liquid refrigerant) at a lower frequency, but flow reversal is less sensitive to channel length than to channel diameter. Simulation results reveals a similar pattern of flow regime and pressure development within one periodic cycle for channels with the same diameter but different lengths, confirming that flow reversal is less sensitive to channel length. Consistent with the experimental results, simulation also predicts less vapor flow reversal at a slower frequency in the longer channel. This is due to relatively more buildup of upstream resistance which is caused by a higher refrigerant velocity in the longer channel, especially at the beginning of a periodic cycle when large dryout area exists.

In the fourth part of the thesis, the effects of refrigerant thermophysical properties on flow reversal are presented. Four refrigerants (R134a, R1234yf, R245fa and R32) are tested in the same system. Heat flux and superheat are maintained the same. It has been found experimentally that R245fa which has similar heat of vaporization with R134a but much larger specific volume difference between vapor and liquid phase generates more reversed vapor flow volumetrically (per unit mass flow rate of supplied liquid refrigerant)

than R134a. A simulation generated by the aforementioned mechanistic model under the same conditions demonstrates that a larger specific volume difference generates more drastic growth of vapor slugs and concentrates more flow resistance to the downstream. As a result, more vapor flow reversal is generated at a higher frequency. Although the simulated frequency results are not validated by the experimental results, the predictions of the reversed vapor flow rates for R134a and R245fa are well confirmed by the experiments. Experiments using R134a, R1234yf and R32 show that the volumetric flow rate of reversed vapor (per unit mass flow rate of supplied liquid refrigerant) is not sensitive to heat of vaporization, although increasing heat of vaporization reduces the absolute volumetric flow rate of the reversed vapor. Frequency of flow reversal increases as the heat of vaporization of the refrigerant decreases. Simulation predictions are consistent with the experimental results. It is shown that the effects of heat of vaporization have similar magnitude on reverse vapor flow and supplied liquid flow, but smaller heat of vaporization creates more drastic vapor slug expansion which increases the frequency.

In the last part of this thesis, the effects of boiling instabilities on heat transfer performance of a microchannel heat exchanger are investigated. In the same facility as introduced in the first part of the thesis, two heat exchangers with identical heat transfer areas are employed. One of them is equipped with an artificial inlet restriction. The two heat exchangers are operated under identical conditions. The heat exchanger without artificial flow resistance is subject to more severe boiling instability and consequently generates four times more reverse vapor flow than the other one. The comparison of capacities under identical operating conditions reveals that more reverse flow helps to improve cooling capacity by up to 13.3%. Meanwhile, numerical simulations of bubble dynamics coupled with heat transfer are carried out for both heat exchangers. Results show that in the heat exchanger with more reverse flow, the refrigerant side heat transfer coefficients are enhanced, especially in the upstream part of a channel where the flow velocity is relatively low.

*To my love, Mufan Luo*

# ACKNOWLEDGEMENTS

My great gratitude first goes to my advisor Professor Predrag S. Hrnjak. His constant support and inspiring guidance made my work possible and productive at the University of Illinois at Urbana-Champaign (UIUC). His passion and devotion towards research influence me very deeply. I would also like to thank the members of my dissertation committee, Professor Anthony Jacobi, Professor Stefan Elbel, Professor J Craig Dutton and Professor Davide Del Col for their insightful inputs to my research.

I feel very fortunate to work in the Air Conditioning and Refrigeration Center (ACRC) among many talented and supportive peers. I would like to thank all of my colleagues, especially Hanfei Tuo, Yang Zou, Dolaana Khovalyg, Augusto Zimmerman, Neal Lawrence, Shenghan Jin, Jiange Xiao, Lili Feng, Rijing Zhao, Jiu Xu, Jun Li, Bill Davies and Bruno Kimura for the valuable discussions, as well as Jesus Sotelo and Andy Nagus for the help in facility construction. I also greatly appreciate the support provided by the industrial sponsors of ACRC. Their financial support and valuable technical input are essential to the accomplishment of this research.

Besides, I am very grateful for all the amazing friends that I have met during my entire PhD career. I expect the friendship with each one of them for many years to come. Among all, my girlfriend Mufan Luo gave me the most support and endless courage. It is her love that made this dissertation possible.

Last but not least, I want to express my great gratitude to my parents Guangjun Li and Qing Song who always love me and trust in me. They taught me how to become a man with integrity and showed me the value of hard work.

# TABLE OF CONTENTS

# LIST OF FIGURES

# LIST OF TABLES

# NOMENCLATURE

| | | |
|---|---|---|
| $A$ | heat transfer area | ($m^2$) |
| $Bo$ | Boiling number | (-) |
| $COP$ | coefficient of performance | (-) |
| $C_p$ | specific heat | $J \cdot K^{-1} \cdot kg^{-1}$ |
| $D$ | hydraulic diameter | (mm) |
| $Eo$ | Eotvos number | (-) |
| $f$ | friction factor | (-) |
| $F$ | force | (N) |
| $g$ | acceleration of gravity | ($m \cdot s^{-2}$) |
| $G$ | mass flux | ($kg \cdot m^{-2} \cdot s^{-1}$) |
| $h$ | specific enthalpy | ($J \cdot kg^{-1}$) |
| $h_{fg}$ | specific latent heat of vaporization | ($J \cdot kg^{-1}$) |
| $HTC$ | heat transfer coefficient | ($W \cdot m^{-2} \cdot K^{-1}$) |
| $k$ | thermal conductivity | ($W \cdot m^{-1} \cdot K^{-1}$) |
| $K$ | pressure loss coefficient | (-) |
| $L$ | length | (m) |
| $m$ | mass | (kg) |
| $\dot{m}$ | mass flow rate | ($kg \cdot s^{-1}$) |
| $Nu$ | Nusselt number | (-) |
| $P$ | pressure | (kPa) |

| | | |
|---|---|---|
| $\dot{q}$ | heat flux | ($kW \cdot m^{-2}$) |
| $r$ | radius | (m) |
| $R$ | ratio | (-) |
| $t$ | time | (s) |
| $T$ | temperature | ($^oC$) |
| $V$ | velocity | ($m \cdot s^{-1}$) |

## Greek

| | | |
|---|---|---|
| $\alpha$ | thermal diffusivity | ($m^2 \cdot s^{-1}$) |
| $\Delta$ | difference | (-) |
| $\varepsilon$ | roughness | (m) |
| $\rho$ | density | ($kg \cdot m^{-3}$) |
| $\sigma$ | surface tension | ($N \cdot m^{-1}$) |
| $\tau$ | time | (s) |
| $\phi$ | distribution rating parameter | (-) |

## Subscripts

| | |
|---|---|
| d | downstream |
| Darcy | Darcy coefficient |
| evap | evaporated |
| fric | friction |
| i | index |
| in | inlet |
| l | liquid phase |
| out | outlet |

| | |
|---|---|
| rel | relative |
| rev | reversed |
| sat | saturation |
| se | sudden expansion |
| sc | sudden contraction |
| u | upstream |
| v | vapor phase |

# Chapter 1 INTRODUCTION

## 1.1 BACKGROUND

Microchannel heat exchangers are widely used in air conditioning and refrigeration systems because of their compactness, enhancement of heat transfer performance both on the air and refrigerant sides and potential for charge reduction. However, microchannel heat exchangers suffer from the problem of refrigerant maldistribution, especially for evaporators (Hrnjak (2004), Kulkarni *et al*. (2004), Brix *et al.* (2009), Brix *et al.* (2010), Li and Hrnjak (2014a), Li and Hrnjak (2015a), Li and Hrnjak (2015b)). In order to avoid high refrigerant side pressure drop caused by reduced channel size, parallel tube structure is employed in microchannel heat exchangers, as shown in Figure 1-1. Multiple microchannel tubes are placed in parallel and combined by an inlet and an outlet header.

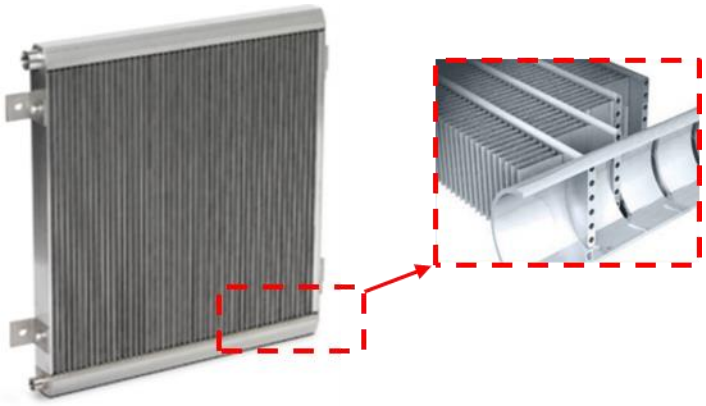

Figure 1-1 Structure of a microchannel heat exchanger

In the inlet header, it is hard to distribute two phase refrigerant evenly among parallel multiple microchannels. As a result, those channels, which are starved from liquid will have a large dryout region, resulting in lower cooling capacity. There are mainly three

reasons for refrigerant maldistribution: 1) two-phase separation in the inlet header, 2) unequal pressure drops along inlet and outlet headers, 3) flow reversal and boiling instabilities within channels. The first two causes are widely investigated in the literature (Hwang *et al.* (1988), Lee and Lee (2004), Vist and Pettersen (2004), Hwang *et al.* (2007), Ahmad *et al.* (2009), Ablanque *et al.* (2010), Byun and Kim (2011), Zou and Hrnjak (2013 a, b), Zou *et al.* (2014) and Li and Hrnjak (2013 and 2014b)), while the third cause remains largely unknown. Tuo and Hrnjak (2013a) is one of the very few studies in the literature that investigated flow reversal and boiling instabilities with microchannel heat exchangers that are used in air conditioning systems. The focus of previous research on flow instabilities in microchannels has been on heat sinks for small scale cooling applications, such as electronic cooling. The heat transfer and fluid flow conditions in these applications are significantly different from those in air conditioning systems.

Therefore, one of the focuses of this research is to experimentally investigate boiling instabilities and flow reversal in microchannel evaporators under conditions and geometries that are relevant to air conditioning applications. Meanwhile, a mechanistic model of bubble dynamics in microchannels will be developed and validated using the experimental results. This model will be able to predict the amount and frequency of flow reversal, which builds a quantitative relationship (not currently available in the literature) between flow reversal and given refrigerant thermophysical properties, channel geometries and operating conditions. Last but not least, the effect of boiling instabilities on heat transfer performance of microchannel heat exchangers will be explored.

## 1.2 STRUCTURE OF THE THESIS

Besides the introductory chapter, this thesis is organized in six chapters. Chapter 2 presents the state-of-art literature review of boiling instabilities in electronic cooling applications as well as air conditioning applications. Chapter 3 presents the visualization of the transient flow regimes (including flow reversal) in an aluminum microchannel as part of a realistic automotive evaporator. The typical flow regime development in direct expansion (DX) and revised flash gas bypass (FGBR) mode are analyzed. Chapter 4 presents a numerical model of multiple bubble dynamics inside of a diabatic channel. This model is used to demonstrate the mechanism of flow reversal. In Chapter 5, the effects of channel geometry (diameter and length) on flow reversal are investigated. In Chapter 6, the effects of refrigerant properties (specific volume difference between vapor and liquid and heat of vaporization) on flow reversal are studied. Chapter 6 demonstrates the effect of boiling instabilities and flow reversal on the heat transfer performance of an evaporator. Both experimental and simulated results indicate enhancement of heat transfer caused by flow reversal.

# Chapter 2 LITERATURE REVIEW

In this chapter, a state-of-the-art review including the most relevant research in the literature is presented. The literature review consists of four sections: 1) Background; 2) Experimental studies; 3) Numerical studies; and 4) Limitations of previous studies.

## 2.1 BACKGROUND

The flow regimes in microchannels are distinctively different from those in conventional size tubes. Chen *et al*. (2006) visualized the adiabatic flow regime (shown in Figure 2-1(1)) of two-phase R134a in vertical tubes with four inner diameters (1.10, 2.01, 2.88, 4.26 mm). They found out that 2 mm seems to be the critical diameter to distinguish macro and small channels for their operating condition based on the flow regime observation. In 2.88 mm and 4.26 mm diameter tubes, there are churn flow regimes with a very chaotic vapor-liquid interface. When the diameter reaches down to 2.01 mm, a less chaotic vapor-liquid interface was observed and confined bubble flow regime occurred under low pressure conditions, indicating that surface tension starts to play more important roles. Finally, when the diameter was 1.10 mm, confined bubble flow regime becomes prevalent under all pressures. Later on, in the same research group, Karayiannis *et al.* (2008) provided the visualization (shown in Figure 2-1(2)) of two-phase R134a flow in a tube with 0.52 mm diameter. Aside from the prevalence of confined bubble flow, another unique characteristic of the flow regime is the absence of dispersed bubble flow. Wu and Mudawar (2004) also mentioned that in microchannels, bubbly flow is hard to be sustained and slug flow will appear soon after incipient boiling.

Revellin and Thome (2007) observed very similar flow patterns (shown in Figure 2-1(3)) of two-phase R134a in a 0.5 mm diameter tube with Karayiannis *et al.* (2008), although they used different terminology to categorize the flow regimes.

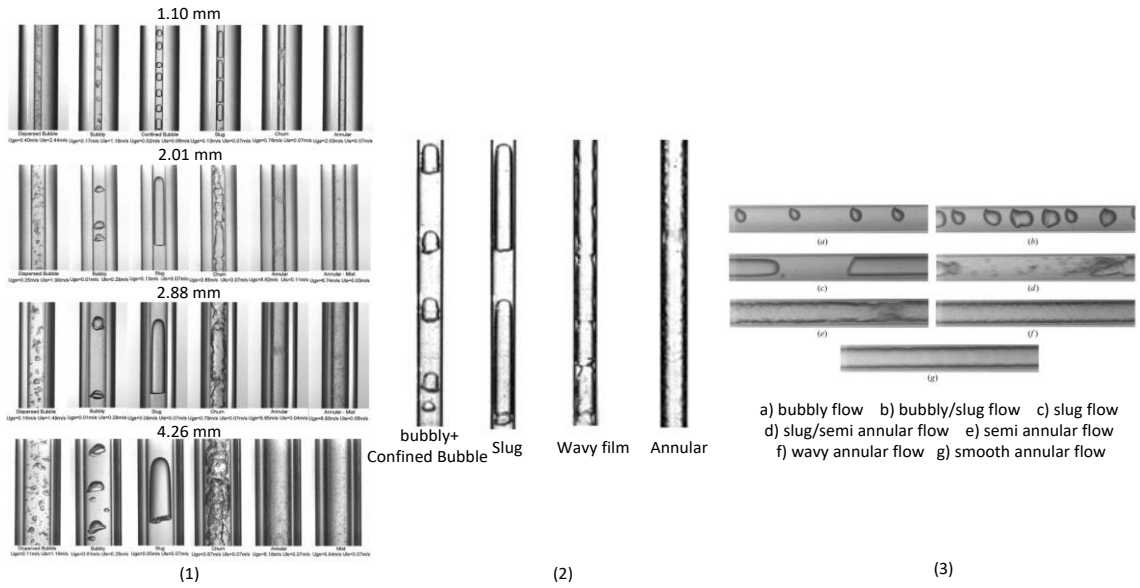


Figure 2-1 Flow regimes in microchannels found in the literature (Chen *et al.* (2006), Karayiannis *et al.* (2008) and Revellin and Thome (2007))

In small channels, a bubble can quickly grow to a size that is comparable with the channel diameter. In the confined bubble and slug flow regime, a bubble or vapor slug can only grow longitudinally. The rapid growth of a bubble or vapor slug creates a local pressure peak somewhere along the tube. If the local pressure peak is higher than the inlet pressure, the incoming flow will decelerate and even flow backward. Bergles and Kandlikar (2005) summarized two causes for flow instabilities in microchannels. The first one is upstream compressible volume instability, which is a density wave oscillation. The second one is excursive instability. One illustration of this type of instability can be found in a pressure drop-mass flux curve as shown in Figure 2-2. Under constant heat

flux, the mass flow rate decreases, as does the pressure drop, in the single phase liquid region. When boiling starts, the pressure drop increases, even though mass flux still decreases. The system starts to lose stability in the vicinity of the minimum pressure drop condition. At point c in Figure 2-2, perturbations caused by bubble ebullition can trigger the excursion from point c to point a. In addition to the two causes of instability proposed by Bergles and Kandlikar (2005), Kuo and Peles (2008) added another two, which are rapid bubble growth and critical heat flux (CHF). The instability caused by rapid bubble growth is associated with high superheat required for bubble nucleation and local pressure elevation during bubble growth. Critical heat flux is interconnected with compressible volume instability and excursion instability. Lower heat flux leads to a slower bubble formation process, which can moderate compressible volume instability and excursion instability. In turn, less oscillation can delay CHF conditions. Kandlikar (2005) and Karayiannis and Mahmoud (2016) also believe that rapid bubble growth and expansion is one major reason of boiling instabilities and flow reversal. Tadrist (2007) reviewed two-phase instabilities in narrow channels. He concluded that the mechanism for two-phase boiling instabilities in microchannels is the following: heat input causes rapid vapor recoil in the longitudinal directions within the channel; as the vapor generation decreases, the recoil forces are reduced and the channel is filled with liquid again. In Tadrist (2007), Brutin's PhD thesis (2003) was discussed in great detail. In that thesis, the author claimed that in a flow boiling situation, the boiling instabilities were determined by the competition between the vapor recoil effect (caused by rapid vapor expansion) and the inertia effect (imposed by pumps). The mechanistic model presented in Chapter 3 also follows the same idea.

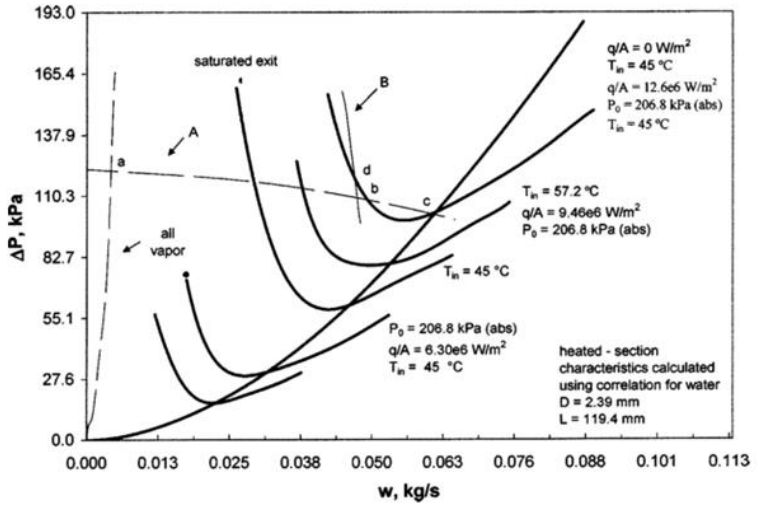


Figure 2-2 Pressure drop vs mass flux curve for in-tube flow under constant and uniform heat flux, Bergles and Kandlikar (2005)

## 2.2 EXPERIMENTAL STUDIES

Figure 2-3 shows the distribution of the most relevant 1000 papers about boiling instabilities (based on Google Scholar search) in the past six decades. The experimental study of boiling instabilities started in the 60s. A good example is Veziroglu and Lee (1969). They investigated boiling instabilities in a two parallel channel setup. They identified two modes of oscillation: density wave mode and pressure drop mode. They also developed an analytical model to predict the starting of the pressure-drop mode instabilities.

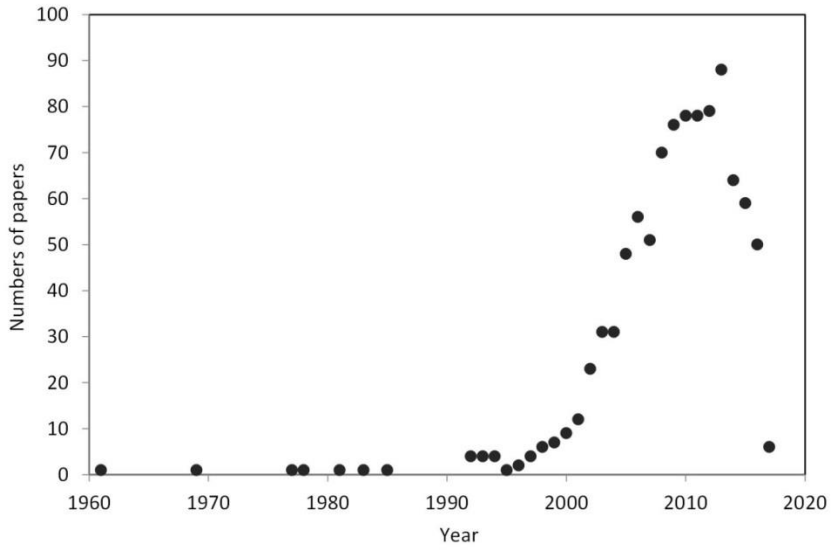


Figure 2-3 Distribution of the most relevant 1000 papers about boiling instabilities in time

During the late 90s and early 2000s, the research about boiling instabilities started to take off. Therefore, the literature review in this study is focused on the research after the year 2000, which is summarized in Table 2-1.

Brutin *et al*. (2003) experimentally investigated the unsteady boiling of n-pentane in heated minichannels. They found that the unsteady boiling region was determined by heat flux and mass velocity, and unsteady boiling created reverse flow and high amplitude fluctuation of the pressure signal. Brutin and Tadrist (2004) further studied the steady and unsteady boiling region determined by heat flux and mass velocity. They found that under each heat flux they examined, there is a critical mass velocity (or Re number) that delimits steady and unsteady boiling. Under each heat flux, unsteady boiling only happens at the low mass velocity region, which can also be interpreted as the high exit quality region. They also examined both confined inlet and compliant inlet (with a buffer)

and discovered that pressure drop oscillation has lower amplitude but higher frequency in the compliant inlet case compared with the confined inlet case.

Wu and Cheng (2003) studied water boiling in two silicon microchannels with diameters of 158.8 and 82.8 micron. They believed a new type of oscillation with long period was discovered in which single phase flow and two-phase flow appear alternatively. The oscillation period in the large channel was 31 s, and it was 141 s in the smaller tube. Wu and Cheng (2004) continued their study about boiling instabilities in parallel microchannels. They first adjusted the water inlet pressure, then gradually increased heat flux. They discovered liquid/two-phase alternating flow at heat flux from 13.5-16.6 W/cm$^2$, then continuous two-phase flow at heat flux of 18.8 W/cm$^2$, and lastly liquid/two-phase/vapor alternating flow at heat flux of 22.6 W/cm$^2$. They found that liquid/two-phase/vapor alternating flow created the largest pressure oscillation, while continuous two-phase generated the least pressure oscillation.

Qu and Mudawar (2004) studied boiling instabilities of water in parallel microchannels under high heat fluxes. They were focusing on two types of dynamic instabilities: pressure drop oscillation and parallel channel instabilities. They found that pressure drop oscillation can be greatly suppressed by a throttling valve placed before microchannels. Parallel channel instability, which is much milder than pressure oscillation, can also be alleviated by more throttling. They also discovered that under the same mass flux, higher heat flux will help to stabilize the boiling process because the system becomes stiffer with increasing pressure drop and a smaller portion of two-phase flow.

Hetsroni *et al.*, (2005) proposed detailed stages in one cycle of periodic boiling process as shown in Figure 2-4. Soon after nucleation, a bubble grows very rapidly to the size comparable to the diameter of the channel (step a); then the bubble expands bidirectionally (step b); after the downstream edge of the bubble reaches the channel outlet, the bubble begins to vent (step c); few liquid droplets are left on the wall after bubble depletion (step d); along with bubble depletion, pressure inside of the channel decreases and fresh liquid starts to move in (step e); finally, a new cycle starts (step f). Through experiments, they also found that pressure oscillation caused by boiling instabilities increases with increasing quality. Hetsroni et al., (2006) tried to describe boiling instabilities by dimensionless groups. They picked Nusselt number (Nu), Eotvos number (Eo) and Boiling number (Bo). They correlated initial film thickness and Nu/Eo with Bo and believed Bo (q/mhfg) is the bond between the momentum and energy equations.

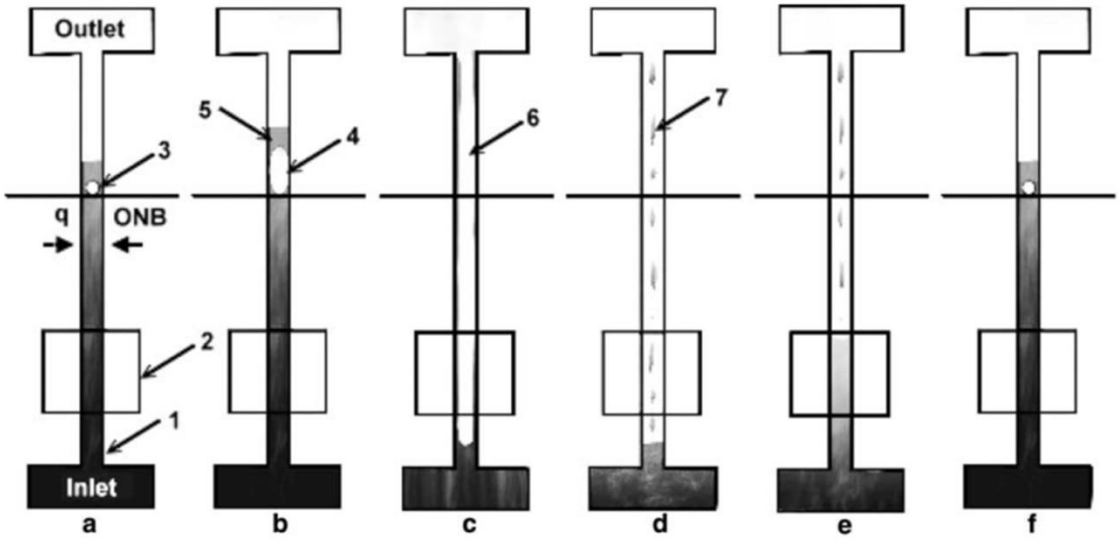


Scheme of explosive boiling: (1) microchannel; (2) area of visual observation; (3) ONB point; (4) elongated cylindrical bubble; (5) liquid in front of the bubble; (6) vapor; (7) liquid droplets and clusters.

Figure 2-4 Illustration of one cycle of the periodic boiling process (Hetsroni *et al.*, (2005))

Chen and Garimella (2006) visualized FC-77 flow in parallel silicon microchannels. They found that under high heat fluxes (>427 kW/m$^2$), flow reversal occurs near the inlet of the microchannels, causing oscillation of pressure drop. They also concluded that flow reversal, which creates changes of mass flow rate, causes the alternation of flow regime near the outlet of the microchannel. From their results, it can be seen that higher heat flux leads to greater chance of reverse flow, but this comparison is made under the same mass flux and changing outlet quality (under same mass flux, higher heat flux will create higher exit quality). Harirchian and Garimella (2008) visualized FC-77 flow in parallel silicon microchannels with different geometries. They located a throttling valve before the heat sink to suppress instabilities, but flow reversal was still observed at their highest heat flux examined.

Huh et al. (2007) studied boiling instabilities in one microchannel. They discovered that there is a phase shift between pressure drop oscillation and mass flow oscillation. A sudden increase of mass flow rate occurred at the peak of pressure drop. They also found that an increase of mass flow rate led to smaller oscillation amplitude and shorter period. Under the same mass flux, increasing heat flux (equivalent to higher exit quality) created higher oscillation amplitude and longer period.

Kuan and Kandlikar (2007) investigated the effect of boiling instabilities and flow reversal on heat transfer. Pressure drop elements were added in one set of the tests to suppress boiling instabilities. They found that the heat transfer performance was enhanced by using the pressure drop element under 362.9 kg/m$^2$/s mass flux, while the heat transfer performance deteriorated under 144.4 kg/m$^2$/s mass flux. Even the

enhancement in the high mass flux case is arguably comparable with the measurement uncertainty range.

Consolini and Thome (2008) studied the flow boiling of R245fa, R236fa and R134a under stable and unstable conditions. A valve placed at the upstream of the test section was used to control the intensity of the boiling instability. As is shown in Figure 2-5, the heat transfer coefficients under stable boiling conditions can be very different with those under unstable boiling conditions (heat flux and mass flux are kept the same). There is no generalized conclusion about the effect of boiling instabilities on heat transfer.

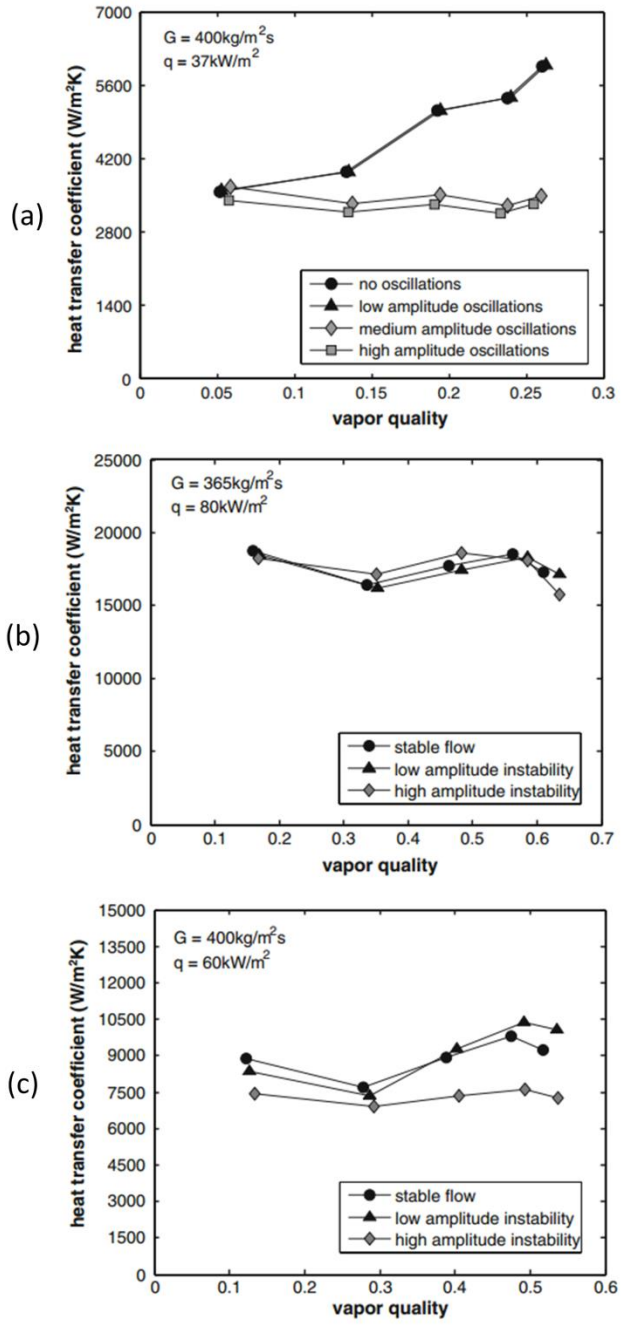


Figure 2-5 Effect of boiling instabilities on heat transfer coefficients: a) R245fa, b) R236fa, and c) R134a

Zhang et al. (2009) investigated excursive instabilities in parallel microchannels. They found that increasing operation pressure, channel diameter, and channel length and adding an inlet restrictor could alleviate instabilities.

Chen and Garimella (2011) found out that boiling instabilities enhanced the heat transfer at the upstream and downstream part of a channel which has hydraulic diameter of 159 micron. In contrast with this research, they (Chen and Garimella (2006)) discovered that in a microchannel with hydraulic diameter of 389 micron, heat transfer coefficient was relatively insensitive to boiling instabilities. They concluded that the size of the channels contributed to the difference.

To the author's best knowledge, flow reversal in air conditioning systems was first reported in the open literature by Bowers et al. (2012). They visualized the flow reversal (as shown in Figure 2-6) in a R410A residential air conditioning system which was operated under direct expansion mode.

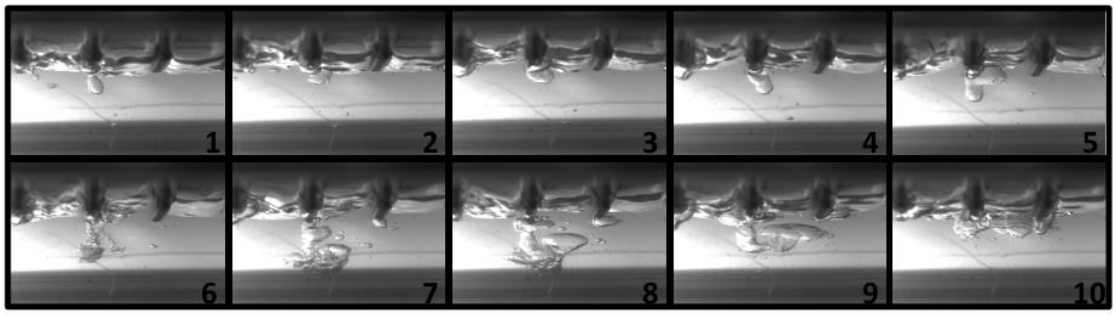


Figure 2-6 Flow reversal in a horizontal inlet header with upward microchannels

Tuo and Hrnjak (2013 a, b and 2014 a, b) studied flow reversal and its effects in a microchannel evaporator used in air conditioning systems. They invented a new system configuration to vent the reversed vapor in the evaporator. They found that the reverse vapor accounted for 2-8% of the total supplied liquid into the evaporator. By venting the reverse vapor, 5 % of capacity and 3 % of COP improvement could be achieved compared with the flash gas bypass AC system baseline. It has been also found that mass

flow rate of reversed vapor shared the same oscillation frequency with the pressure drop and the frequency increased with increasing heat flux.

Prajapati *et al*. (2015) tested three microchannel heat sinks with different geometries (uniform, diverging, and segmented). They found that segmented channels had 5.2 % higher pressure drop than uniform channels and 3.5 % higher pressure drop than diverging channels. As for heat transfer, segmented channels had the highest heat transfer coefficient among all three types of microchannels. The reason could be attributed to more nucleation sites, breakup of the thermal boundary layer, less confinement for bubbles and slugs, and minimum reverse flow. The diverging channels had higher heat transfer coefficient than uniform channels due to the reduction of flow reversal.

Khovalyg *et al*. (2015) investigated boiling instabilities within parallel unevenly heated microchannels. They found that there existed a strong cross-correlation between the most and least heated tubes, especially under low mass flux conditions. The interchannel interaction became less significant when mass flux increased.

Table 2-1 Summary of the previous experimental studies about boiling instabilities

| Author/Year | Fluid and ranges of G ($kg/m^2s$) &q ($kW/m^2$) | Channel shape, material, size ($D_h$), numbers (C#) | Fluid inlet & exit states | | Reverse flow reported |
|---|---|---|---|---|---|
| Brutin *et al*. (2003) | n-Pentane, G=125-475, q=200-700 | Rectangular, Al, Dh=889μm, #CH = 1 | Subcooled | x=20%-40% | Yes |
| Brutin and Tadrist, (2004) | n-Pentane, G=95.8-2258, q=15.7-125.6 | Rectangular, Al, Dh=889μm, #CH = 1 | Subcooled | x=0-1.0 | No |
| Wu and Cheng, (2003) | Water, G = 144 – 251, q = 9.6 – 155 | Trapezoidal, Si, Dh=158.8,82.8μm, #CH = 8,15 | Subcooled | No superheat | No |
| Wu and Cheng (2004) | Water, G = 112 – 146, q = 20 – 2400 | Trapezoidal, Dh=186μm, #CH = 8 | Subcooled | x<16% | No |

Table 2-1 Summary of the previous experimental studies about boiling instabilities (cont.)

| | | | | | |
|---|---|---|---|---|---|
| Balasubramanian and Kandlikar (2005) | Water, G = 112 – 120, q = 208 – 316 | Rectangular, Cu, Dh = 333 μm, #CH = 6 | Subcooled | No superheat | Yes |
| Qu and Mudawar (2004) | Water, G = 134.9 – 400.1, q = 208 – 316 | Rectangular, Cu, Dh = 349 μm, #CH = 6 | Subcooled | x<15% | Yes |
| Lee and Mudawar (2005) | R134a, G = 127 – 654, q=316 – 938 | Rectangular, Cu, Dh=349μm, #CH = 6 | x =0.1%-25% | x=49%-superheat | No |
| Xu et al. (2005) | Water/Methanol, G = 20 -1200, q = 130 - 392 | Rectangular, Cu, Dh = 436 μm, #CH = 26 | Subcooled | No superheat | No |
| Xu et al. (2005) | Acetone, G = 64 - 600, q = 150 - 480 | Triangular, Si, Dh = 155.4 μm, #CH = 10 | Subcooled | x=0.07–1.15 | No |
| Hetsroni *et al*., (2005) | Water, G=95-340, q=80-330 | Triangular, Si, Dh=129 μm, #CH = 13,21 | Subcooled | x<10% | Yes |
| Kandlikar *et al*., (2005) | Water, G = 120, q = 298 – 308 | Rectangular, Cu, Dh = 332μm, #CH = 6 | Subcooled | No superheat | Yes |
| Hetsroni *et al*., (2006) | Water & Ethanol, G = 28.5 – 1267, q = 50.7 – 365 | Triangular, Si, Dh=100,130,220 μm, #CH = 13,21,26 | Subcooled | x<8% | Yes |
| Chen and Garimela (2006) | FC-77, G =286-490, q =94 - 730 | Square, Si, Dh=389 μm, #CH = 24 | Subcooled | x <63% | Yes |
| Koşar *et al*., (2006) | Water, G = 115-389, q = 90 – 6140 | Rectangular, Si, Dh = 227μm, #CH = 5 | Subcooled | No superheat | Yes |
| Chang and Pan (2007) | Water, G = 22 - 110, q = 7.86 – 95.5 | Rectangular, Si, Dh = 86.3μm , #CH = 15 | Subcooled | No superheat | Yes |
| Huh et al. (2007) | Water, G = 170 – 360, q = 200 – 530 | Rectangular, PDMS, Dh = 103.5μm, #CH = 6 | Subcooled | No superheat | No |
| Kuan and Kandlikar (2007) | Water, G = 144, 363, q = 152 – 388 | Rectangular, Cu, Dh = 332μm, #CH = 7 | Subcooled | No superheat | Yes |
| Harirchian and Garimela (2008) | FC-77, G =250-1600, q =0 - 300 | Rectangular, Si, Dh=100-5850 μm, #CH = 2-60 | Subcooled | x=4%-superheat | Yes |
| Wang *et al*., (2008) | Water, G =75-1500, q = 184.2 - 485.5 | Trapezoid, Si, Dh= 186, #CH = 8 | Subcooled | No superheat | Yes |
| Kuo and Peles (2008, 2009) | Water, G = 86 – 520, q = 0 – 2340 | Rectangular, Si, Dh = 223 μm, #CH = 5 | Subcooled | No superheat | No |
| Consolini and Thome (2009) | R245fa, R236fa, and R134, G= 300-2000, q=0-200 | Rectangular, Stainless steel, Dh = 510, 790 μm, #CH = 1 | Subcooled and Saturated | Two phase | No |
| Zhang *et al*., (2009) | Water/HFE-7100, G = 5 – 345, q = 30-44 | Rectangular, Si, Dh=100,220,337, #CH =100,40,25 | Subcooled | No superheat | No |

Table 2-1 Summary of the previous experimental studies about boiling instabilities (cont.)

| | | | | | |
|---|---|---|---|---|---|
| Chen and Garimella (2011) | FC-77, G =f 254–1015, q = 100–1080 | Rectangular, Si, Dh=159, #CH =60 | Subcooled | No superheat | Yes |
| Barber *et al*., (2011) | FC-72, G= 32, q=4.26 | Rectangular, Glass, Dh=889μm, #CH = 1 | Subcooled | No superheat | Yes |
| Szczukiewicz *et al*., (2012) | R245fa, R236fa, and R1234ze(E), G= 283-2370, q=19-486 | Rectangular, Si, Dh=100μm, #CH = 67 | Subcooled | No superheat | Yes |
| Bogojevic *et al*., (2009, 2013) | Water, G = 72.2 – 433.3, q=178 – 445 | Rectangular, Si, Dh=194μm, #CH = 40 | Subcooled | No superheat | Yes |
| Tuo and Hrnjak (2014) | R134a, G = 40– 65, q=7.5 – 11.5 | Rectangular, Al, Dh=1000μm, #CH = 250 | Saturated | superheat | Yes |
| Khovalyg *et al*. (2015) | R134a, G = 86–430, q=3.8 – 18.7 | Circular, Glass, Dh=508μm, #CH = 4 | Saturated | superheat | Yes |
| Prajapati *et al*. (2015,2017) | Water, G = 100–350, q=10 – 350 | Cu, Dh=522μm, #CH = 12 | Subcooled | x<9% | Yes |
| Lee and Mudawar (2016) | R134a, G = 152.9–530.7, q=8.0 – 48.4 | Rectangular, Cu, Dh=1000μm, #CH = 75 & 100 | Saturated | superheat | No |
| Kuang *et al*. (2017) | R717, G = 66–148.2, q=3.7 – 12.2 | Rectangular, Cu, Dh=1048μm, #CH = 4 | Subcooled | No superheat | Yes |

## 2.3 NUMERICAL STUDIES

Literature reviewed in this chapter focuses on 1D modeling aiming to explain the physics of flow reversal instead of 3D models concentrating on detailed flow physics. Compared with the experimental studies, there are far fewer simulation studies available in the literature, which are summarized in Table 2-2.

Hetsroni *et al*. (2005) proposed a simple physical model to simulate the unsteady cyclic flow. The following assumptions were made: 1) bubbles nucleate when the wall temperature is higher than the saturation temperature; 2) heat flux is constant and uniform;

3) all heat input is used to evaporate liquid, and refrigerant is in saturated state; 4) after bubbles are vented, there are liquid droplets attached on the wall that gradually evaporate; 5) the thermal inertia of the tube wall is neglected. Simulation results show that cycle time and film thickness decrease with increasing heat flux, which matches the experimental results fairly well. Although simulation results were presented, the details of the model were not revealed in this paper.

Kenning *et al*. (2006) developed a 1D model to simulate single bubble growth in a microchannel. They defined bubble growth into two stages: unconfined ((a) in Figure 2-7) and confined ((b) in Figure 2-7). In the unconfined stage, the radius of the spherical bubble is governed by an empirical correlation (function of time) proposed by Plesset and Zwick (1954). In the confined growth stage, the bubble growth is governed by mass, momentum and energy conservation equations. Comparison between experimental data and optimized simulation results shows that this model predicted accurately the exponential growth of a bubble and predicted fairly well the fluctuation of the inlet pressure (increase first, then decrease).

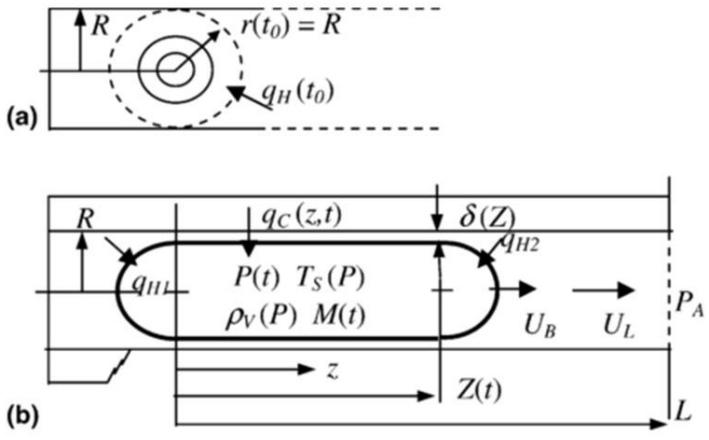


Figure 2-7 Illustration of Kenning *et al*.'s model

Gedupudi *et al*. (2010) developed a 1D model for single bubble growth inside of one microchannel. They divided the whole growth process into three stages (as shown in Figure 2-8): 1). partially confined growth, 2). fully confined growth, 3). vapor venting. Bubble growth was governed by the energy input. The growth rate of the bubble determined the velocity difference of the upstream liquid slug and the downstream liquid slug. The velocities of both liquid slugs were also governed by pressure. The momentum conservation equation was solved with the knowledge of heat input. In their simulation, there was inlet resistance and upstream compressibility. When the outlet pressure was fixed, oscillation of the inlet pressure was shown by their simulation. The highest pressure was found to be somewhere along the tube instead of the inlet.

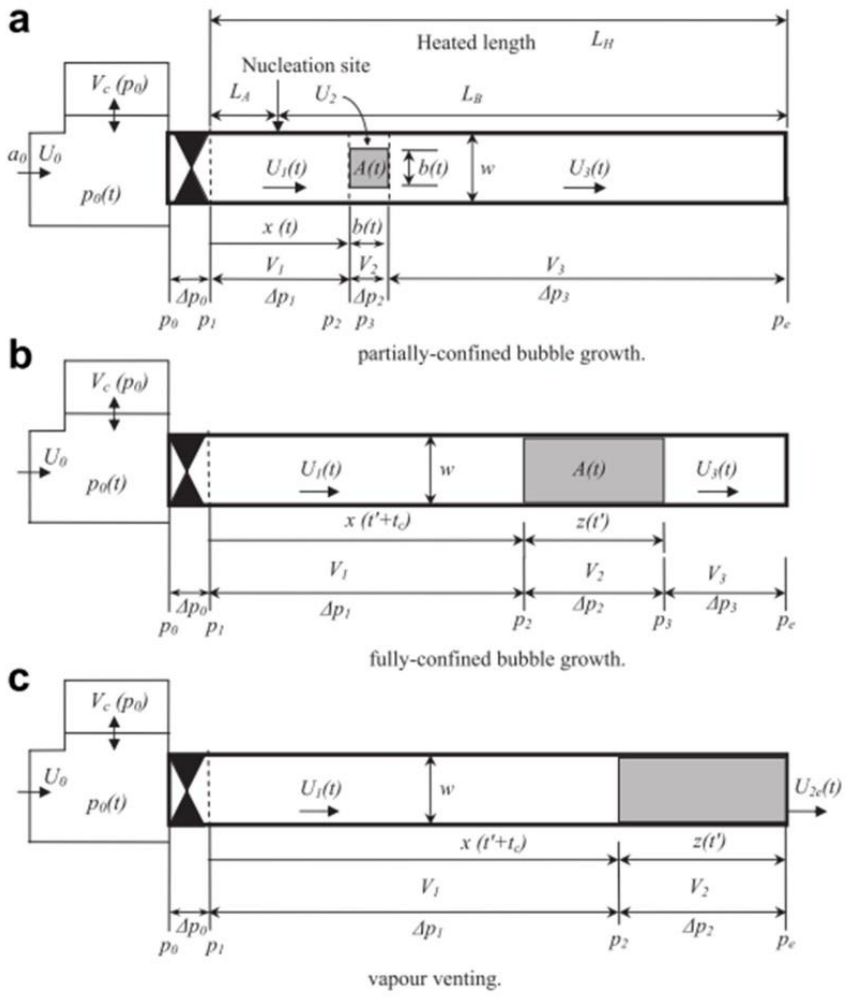


Figure 2-8 Illustration of Gedupudi *et al*.'s model

Belmares and Park (2014) simplified the flow inside of a microchannel into two elements: liquid and vapor. They modeled the pressure drop of each element and applied mass balances on the liquid and vapor interfaces. Through simulation, they found that flow reversal occurs more easily if the liquid front interface lies closer to the inlet and that an inlet flow restriction can alleviate flow reversal.

Revellin *et al*. (2008) modeled the collisions between a series of bubbles. They used the model developed in Agostini et al. (2007) to link the velocity and length of elongated

bubbles. Coupled with heat input, which determines the growth rate of a bubble, bubble collision can be simulated when the liquid slug between bubbles vanishes.

He *et al*. (2017) developed an analytical model of single bubble dynamics. Flow reversal and pressure oscillation can be simulated using this model. This model is based on a similar idea with Gedupudi *et al*. (2010). Bubble movement and pressure oscillation are determined by solving the momentum equation of the liquid slug coupled with the force balance at the liquid-vapor interface.

Table 2-2 Summary of the previous simulative studies about boiling instabilities

| Author/Year | Fluid | Number of bubbles | Reverse flow reported |
|---|---|---|---|
| Hetsroni *et al*., (2005) | Water | 1 | Yes |
| Kenning *et al*., (2006) | Water | 1 | No |
| Gedupudi *et al*., (2011) | Water | 1 | No |
| Gedupudi *et al*., (2014) | Water | 1 | No |
| Revellin *et al*., (2010) | R134a | Multiple | Yes |
| Agostini *et al*., (2007) | R134a | 1 | Yes |
| Belmares and Park (2014) | Water | 1 | No |
| He *et al*., (2017) | Water | 1 | Yes |

## 2.4 LIMITATIONS OF PREVIOUS STUDIES

Most of the research reviewed above focuses on flow instabilities in microchannel heat sinks used in electronics cooling applications. There are very few studies investigating flow instabilities in microchannel evaporators used in air conditioning applications. There are four distinctive differences between these two applications: 1) in heat sinks for electronics cooling, the incoming flow is normally subcooled and the exit quality is very low (below 0.5), while in microchannel evaporators of A/C systems, the fluid at the inlet is either two-phase or saturated liquid and the outlet is normally superheated. Within the studies summarized in Table 2-1, there are only five studies having saturated refrigerant at the heat exchanger inlet and only five studies having superheated refrigerant at the heat exchanger outlet. 2) The heat flux in electronic cooling applications (normally hundreds of $kW/m^2$ on the refrigerant side) is much higher than that in air conditioning applications (on the order of magnitude of 10 $kW/m^2$ on the refrigerant side). 3) Water is the most commonly used fluid in the reviewed studies, and its thermophysical properties (vapor density, heat of vaporization, etc.) are significantly different with those of hydrofluorocarbons which are used in air conditioning applications (R134a, R410A, R245fa etc.). Within the studies summarized in Table 2-1, only six studies use HFC as the working fluid. 4) The motivation of the research related to electronics cooling is to achieve better thermal stability, while the greatest concern for air conditioning applications is to maximize cooling capacity. To sum up, the boiling instabilities including flow reversal have not been thoroughly investigated in microchannel heat exchangers which are used in air conditioning applications (using hydrofluorocarbons as refrigerant and with refrigerant side heat flux on (or less than) the

order of magnitude of 10 kW/m$^2$). Additionally, the effect of boiling instabilities is unknown on the heat transfer performance of a microchannel heat exchanger. The first objective of this research is to fill the aforementioned gaps in the literature through experimentation.

Additionally, the comparison between Table 2-1and Table 2-2 demonstrates the lack of simulation work to explore the mechanism of flow reversal. There is no model available in the literature to simulate multiple bubble dynamics including flow reversal. The second objective of this research is to develop such a model to demonstrate the physics of flow reversal.

# Chapter 3 VISUALIZATION AND MEASUREMENT OF REVERSE FLOW IN AN ALUMINUM MICROCHANNEL EVAPORATOR

## 3.1 INTRODUCTION

In this study, flow regimes in an aluminum microchannel under air heating are visualized. Due to the usage of a special technique (introduced in Chapter 3.2.2), this visualization is believed to be very similar with the realistic flow regime in operating microchannel heat exchangers. Through careful analysis of the high speed video, different flow regimes in DX and FGBR mode are identified. The mechanism of flow reversal is also discussed.

## 3.2 EXPERIMENT SETUP

### 3.2.1 SYSTEM SETUP

The schematic drawing of the facility is shown in Figure 3-1. The working fluid used in this study is R134a and the lubricant is PAG46 (oil circulation ratio is maintained around 1%). The fixed displacement compressor (driven by a variable speed motor) and the microchannel condenser are components that are used in a major brand vehicle. The microchannel evaporator is one slab of a genuine automotive evaporator which originally

had a two slab design. Aluminum headers are replaced by transparent hollow PVC headers for the purpose of visualization. As a result, the evaporator was converted to single pass. The length of the finned tube is 145 mm. The whole heat exchanger consists of 33 tubes. Inside of each tube, there are 6 parallel microchannels with a hydraulic diameter of 2.8 mm. Currently there is no general agreement regarding the classification and definition of conventional channel, minichannel and microchannel. There are not only criteria which are purely based on hydraulic diameter (Kandlikar (2003)) but also criteria which combine hydraulic diameter with the thermophysical properties of the working fluids (Brauner and Maron (1992), Kew and Cornwell (1997), Triplett et al. (1999) and Akbar et al. (2003)). In this study, the definition of microchannel from Thome et al. (2004) is selected. According to them, the best threshold for microchannel is that the size of the channel confines bubble flow. Through visualization of the flow regimes in this study, it has been found that the bubble growth is confined by the channel wall and the elongated bubble regime is one of the dominating flow regimes. Due to this reason, the terminology of microchannel is used in this research.

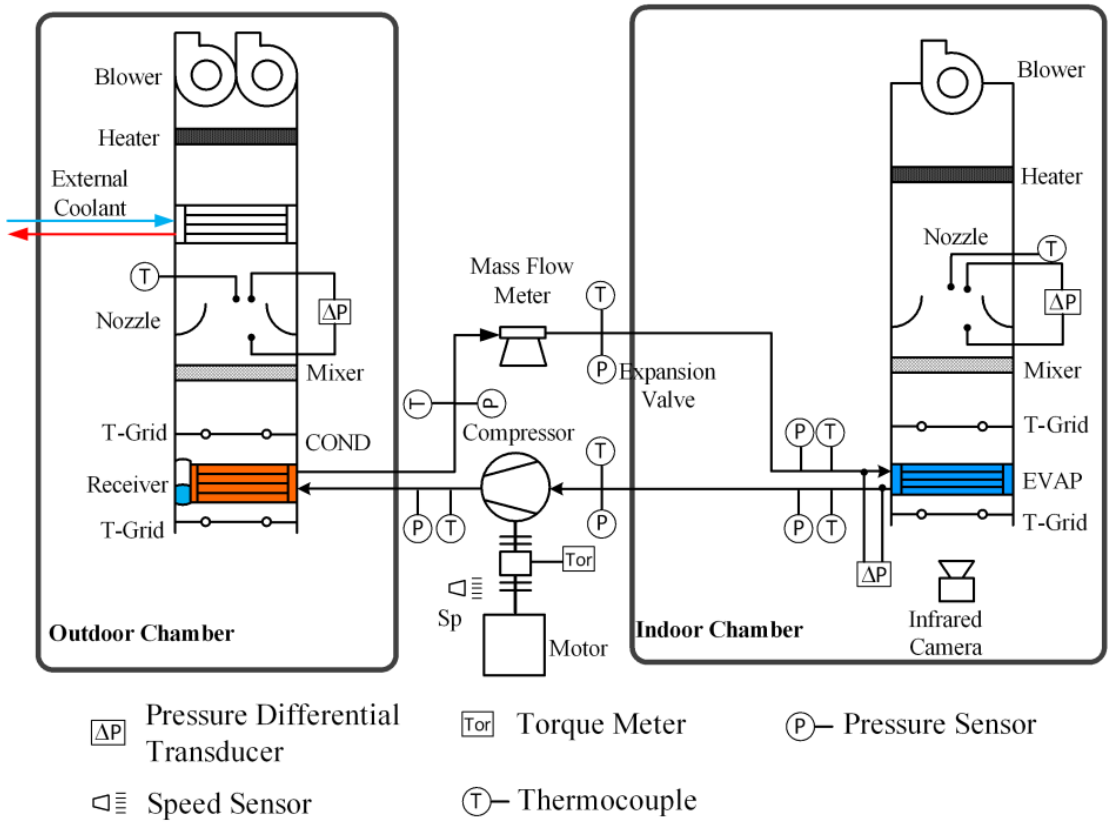


Figure 3-1 Schematic drawing of the test facility

To measure the flow rate of reversed vapor, a FGBR configuration which was used in Tuo and Hrnjak (2014a) is employed (as shown in Figure 3-2). FGBR is a modification of the flash gas bypass (FGB) configuration. In the FGB mode, a separation vessel is placed before the evaporator, ensuring that only liquid is supplied to the evaporator and vapor is bypassed to the inlet of a compressor. Although only liquid is supplied, a substantial amount (up to 8% in Tuo and Hrnjak (2014b)) of vapor is reversed back into the inlet header, which obstructs the continuous liquid feeding. Based on the FGB configuration, two venting ports are added near both ends of the inlet header in FGBR mode, directing the reversed vapor to the top of the separation vessel. In this way, only

liquid feeding is guaranteed in FGBR mode. The dynamic mass flow rate of reversed vapor is measured by a mass flow meter placed on the venting line.

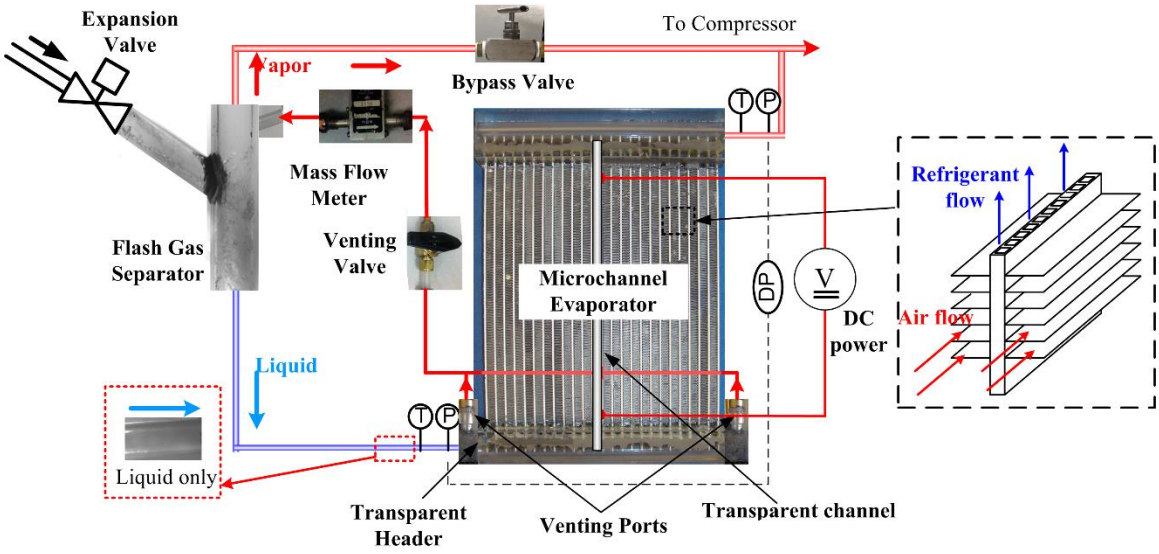


Figure 3-2 Evaporator setup in FGBR mode (Tuo and Hrnjak (2014a))

## 3.2.2 VISUALIZATION SECTION SETUP

For the visualization sections, two tubes in an evaporator are chosen and one outer wall and the first inner wall of each tube are removed by electrical discharge machining (EDM). In this way (as shown in Figure 3-3), the first microchannel port was sacrificed so that a transparent window made by PVC can be placed in. After proper sealing, through the transparent window, the flow regime in the second microchannel port can be visualized. This visualization technique can ensure very realistic flow regimes in the microchannel. The only difference with reality is that the frontal aluminum surface of the second port is replaced by PVC (with low conductivity), but this surface only accounts for 20.9% of the refrigerant side heat transfer area. In addition, heat transfer on this

surface occurs between refrigerant streams, which is insignificant due to the small temperature difference. In order to ensure sufficient spatial resolution of in-tube flow regimes, the transparent channel is divided into three sections with equal length and visualization for each section is done separately. Since flow regimes in sections 2 and 3 are mostly annular or dryout flow, the visualizations provided in this paper are in section 1 except Figure 3-12(b) which is in section 2. To the author's best knowledge, visualization of bubble dynamics including flow reversal in a single air heating aluminum channel is done for the first time in the literature. Usage of two transparent channels increases the reliability of the visualization by providing redundancy. In this study, only the visualization in tube 2 (shown in Figure 3-3) is presented due to higher visualization quality compared with tube 1. Due to two phase refrigerant maldistribution in DX mode, tube 2 is expected to have lower inlet quality than tube 1 due to its longer distance to the inlet (refer to the flow regimes in the inlet header and infrared images from Li and Hrnjak (2015b)), but the exact value is immeasurable in this facility. In FGBR mode, since only liquid is supplied to each channel, tube 1 and tube 2 are expected to have inlet quality of 0.

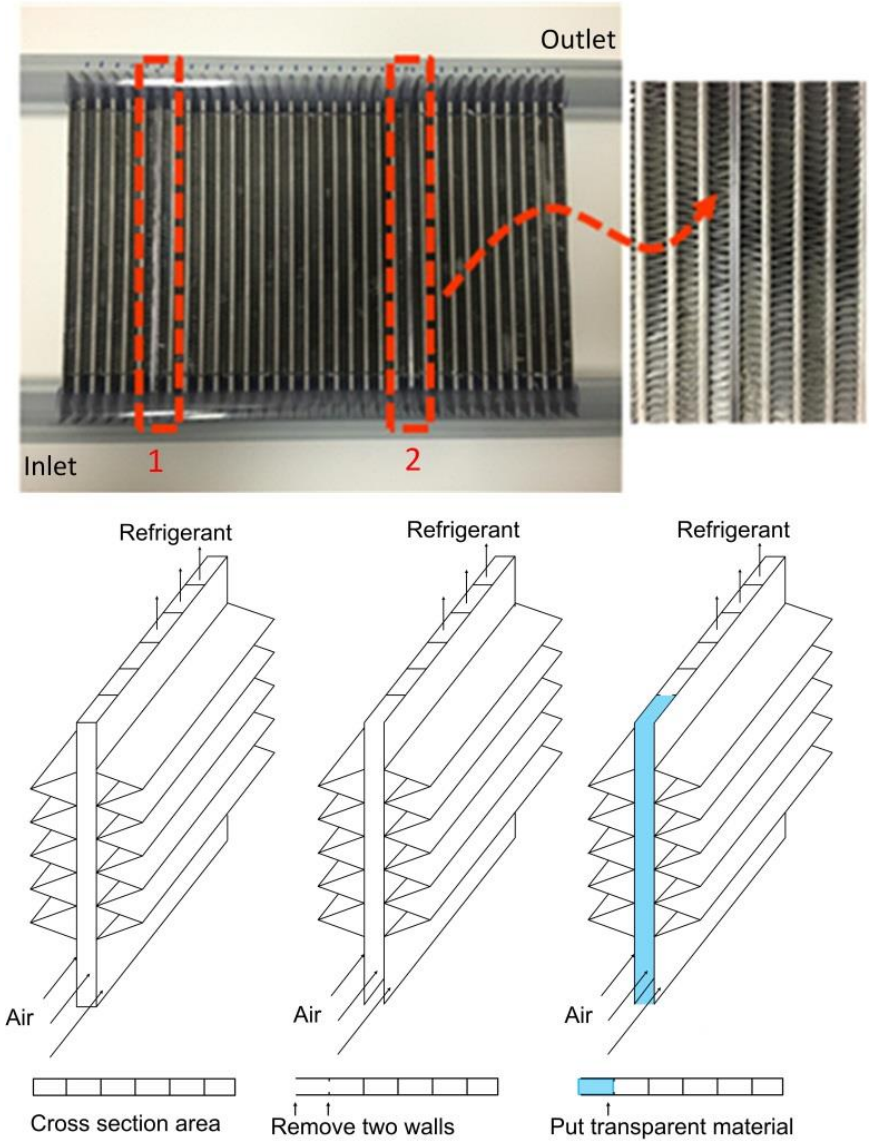


Figure 3-3 Visualization section: aluminum tube with transparent window

## 3.3 TRANSIENT FLOW REGIMES INSIDE OF ONE MICROCHANNEL

In DX operation mode, two-phase refrigerant is supplied into each microchannel, while in FGBR mode, in principle, each channel only experiences liquid feeding due to

continuous vapor venting. In FGB mode, although only liquid is supplied to the inlet header, microchannels still receive two-phase refrigerant at the inlets, due to the re-entrance of reversed vapor. The flow regime inside of one channel is expected to fall in between the flow regimes in DX and FGBR modes. For this reason, this study only demonstrates the flow regimes in DX and FGBR modes.

### 3.3.1 FLOW REGIMES IN DX MODE

In DX mode, the evaporator is operated at 305 kPa saturation pressure with an inlet quality of 0.33. The average refrigerant side heat flux is fixed at 6.4 kW/m$^2$ and the average refrigerant mass flux is around 6.7 kg/m$^2$/s. The system is operated at 7 ºC compressor inlet superheat. By processing the high speed video, three flow regimes as shown in Figure 3-4 are identified, and they occur alternatively. Red lines are used to highlight the vapor-liquid boundaries. Chen et al. (2006) visualized the flow regime in a channel with a similar diameter (2.88 mm). Although their mass flux is much higher (84-1720 kg/m$^2$/s), the flow regimes they provided (quality ranges from 0.2%-85.8%) cover all three typical flow regimes in this study. In this research, even though the mass flux and quality are nearly constant at the heat exchanger inlet, the flow regime in each individual channel varies in time. It is partly due to the distribution issue in parallel channel structure (each channel may not receive constant mass flux and inlet quality all the time) as is indicated in Niño et al. (2003), but more importantly due to the unstable boiling process. The boiling instabilities inside of microchannels induce the acceleration and deceleration of the working fluid, which alters the flow regimes simultaneously. Due

to aforementioned reasons, the conventional flow regime mapping cannot correctly characterize the flow configuration inside of a channel during unstable boiling.

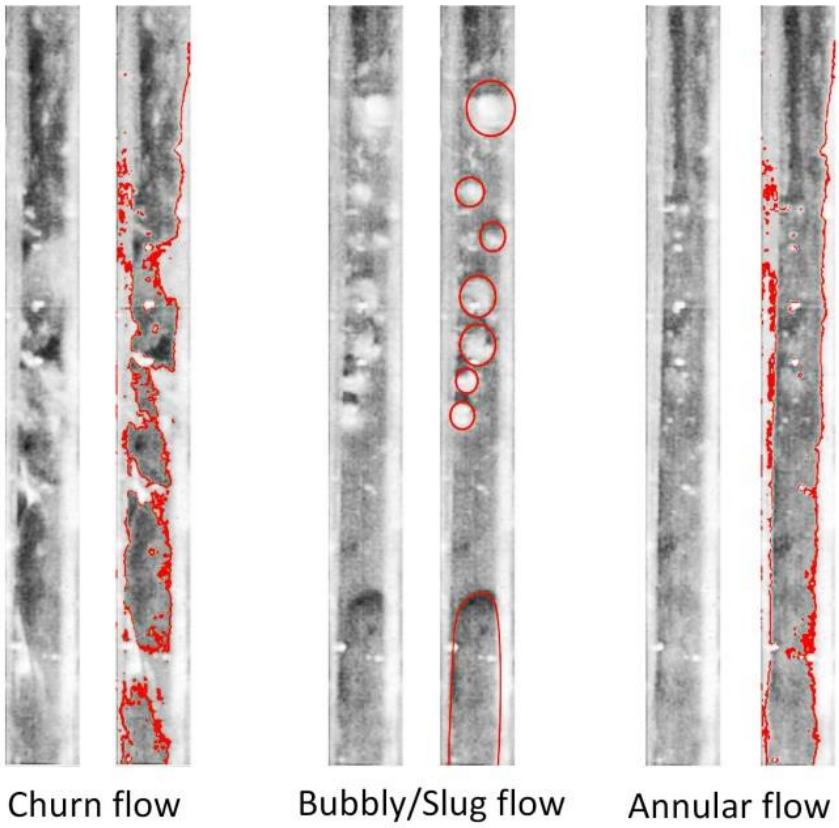


Figure 3-4 Typical flow regimes in DX mode

Figure 3-5 shows the flow regime development within 14 seconds of the high speed video. Churn flow appears when the velocity of the feeding two-phase fluid is high. High velocity is most likely caused by the small downstream resistance within the tube. Under consistent air heating, bubbles inside of the channel expand rapidly in longitudinal directions, decelerating the forward flow and accelerating the downstream flow. As the velocity of the feeding fluid decreases to a certain extent, the churn flow transitions to the bubbly/slug regime. Flow reversal only occurs during the bubbly/slug regime. During 14

seconds of high speed video, 168 milliseconds of flow reversal are observed, which is included in the circled region of Figure 3-5. As shown in Figure 3-6, a dotted line is used to track the upstream edge of one bubble and it shows a backward flow direction. The period and quantity (visually observed) of flow reversal is much shorter and smaller compared with FGBR mode. Reverse flow is normally soon replaced by forward bubbly/slug flow. After continuous evaporation, the vapor quality inside of the channel becomes so high that the entire channel is occupied by a vapor core with a thin film of liquid covering the walls (annular flow in Figure 3-4). Since the flow regimes inside of a microchannel in DX mode are extremely complex phenomena, which are determined by the local flow regime near the channel inlet and the pressure distribution along the entire channel, the duration of each flow regime is not constant. The alternation of these three flow regimes is normally on the order of churn flow-bubbly/slug flow-annular flow.

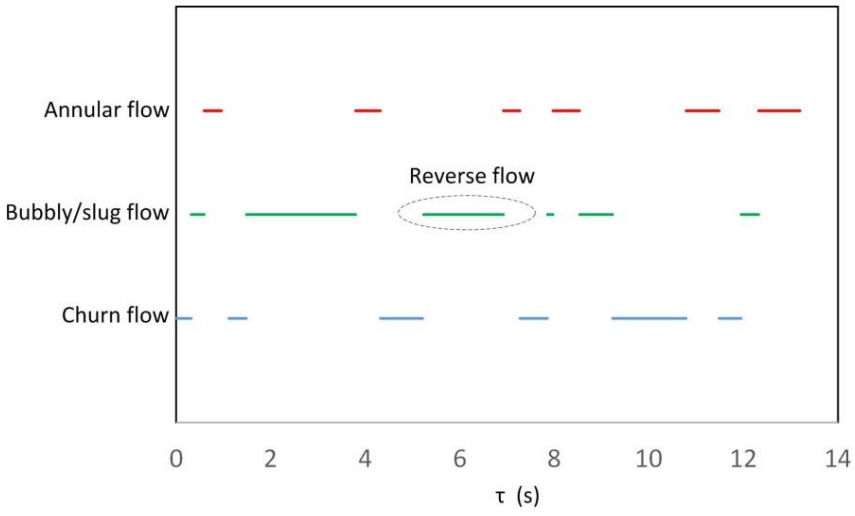


Figure 3-5 Flow regime development in DX mode

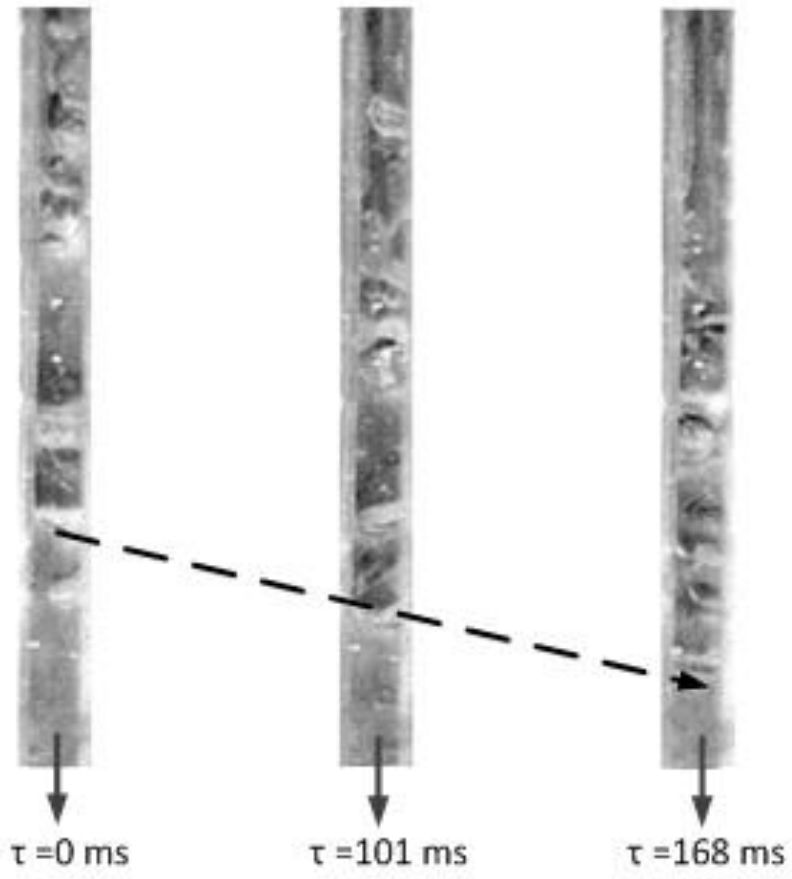


Figure 3-6 Flow reversal occurs in bubbly/slug regime

### 3.3.2 FLOW REGIMES IN FGBR MODE

In FGBR mode, feeding fluid is always in the form of liquid and reverse flow is always in the form of bubbly/slug flow; the flow regime is categorized using forward and reverse flow as shown in Figure 3-7.

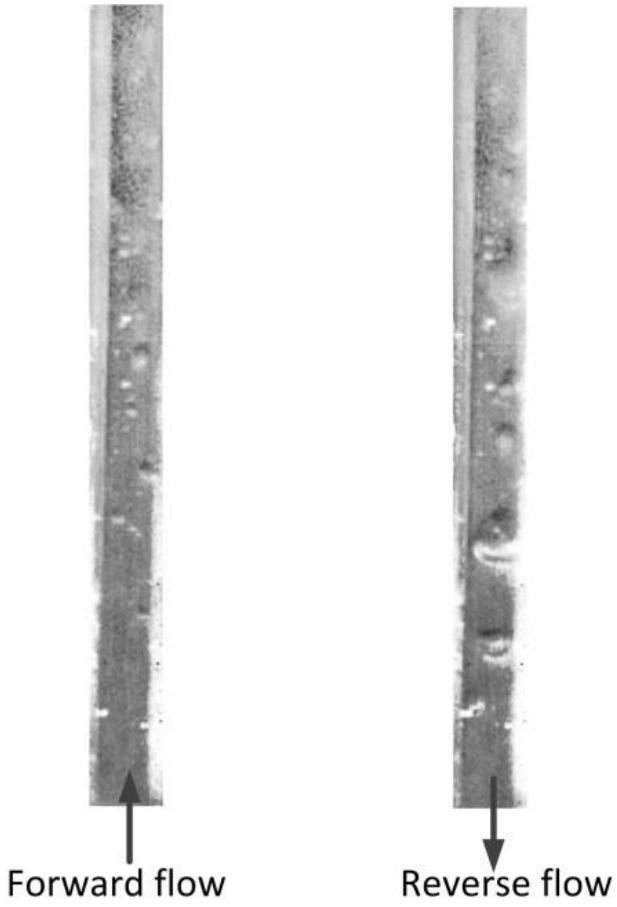


Figure 3-7 Typical flow regimes in FGBR mode

In FGBR mode, the evaporation pressure is kept at 411 kPa. The inlet quality of each channel is believed to be 0. The average refrigerant side heat flux is fixed at 7.8 kW/m$^2$ and the average refrigerant mass flux is around 8.6 kg/s/m$^2$. The system is operated at 13 ℃ compressor inlet superheat. The occurrence and period of both forward and reverse flows within a 12 second high speed video is summarized in Figure 3-8. It has been found that forward and reverse flow happen alternatively. Through Fast Fourier Transformation, the dominant frequency of the flow regime alternation is identified to be 0.94Hz.

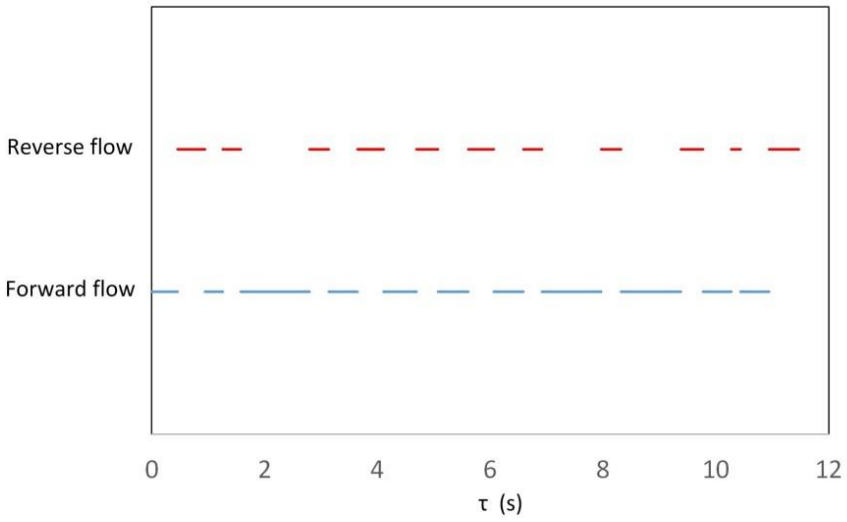


Figure 3-8 Flow regime development in FGBR mode

One periodic cycle consists of a forward and a reverse flow. Tuo and Hrnjak (2014a) used the same facility to visualize the flow regime inside of an electric heating glass tube and they identify nine representative transient flow regimes under FGBR mode (as shown in Figure 3-9(a)). Although the heat flux (10.9 kW/m$^2$) and mass flux (28.5 kg/s/m$^2$) in Tuo and Hrnjak's (2014a) study are higher than those in this study, a great similarity can be found when comparing the visualization results within one periodic cycle of both studies.

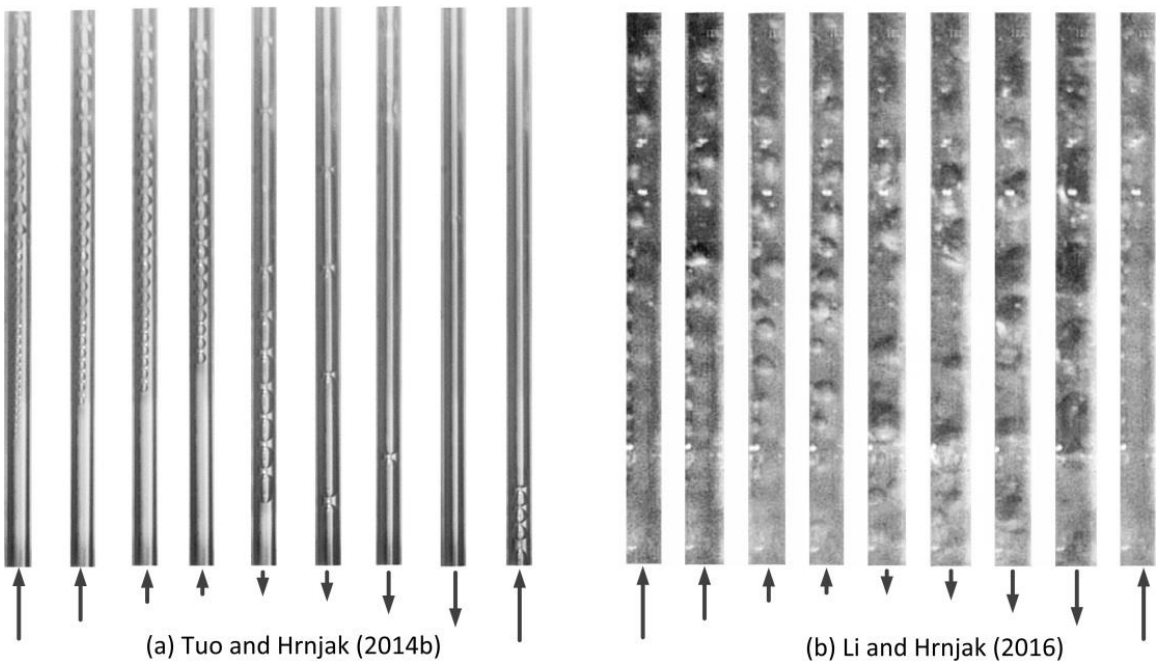


Figure 3-9 Flow regimes within one periodic cycle in FGBR mode (glass and aluminum channel)

At the beginning of a cycle, fresh liquid flows into the channel. Since the channel is relatively empty at this point with a large portion of elongated vapor slug (or dryout) at the downstream, the incoming liquid accelerates due to small flow resistance at the downstream. As liquid continue to evaporate, the vapor slug grows rapidly in the longitudinal direction (growth in radius direction is constrained by the channel wall). As a result, the downstream part of the flow is accelerated, which creates higher downstream frictional resistance. Meanwhile, the incoming flow decelerates. Figure 3-10 shows the flow regime soon after the liquid refrigerant enters both channels. The velocities of the selected vapor slugs in Figure 3-10 are recorded from the moment that these bubbles detach from the channel wall untill the moment of reversal. The velocity profiles of the selected bubbles in both channels show the same trend: accelerating (short period)-decelerating-reversal (as shown in Figure 3-11).

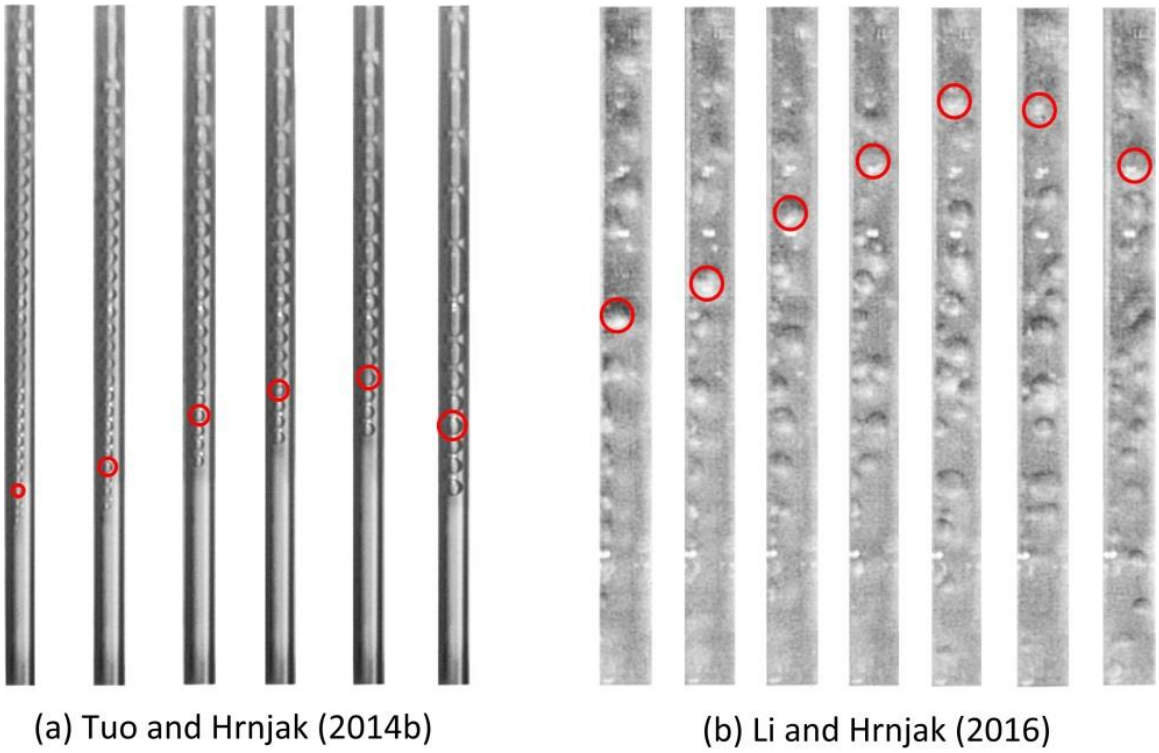


Figure 3-10 Flow regime development at an early stage of a periodic cycle (glass and aluminum channels)

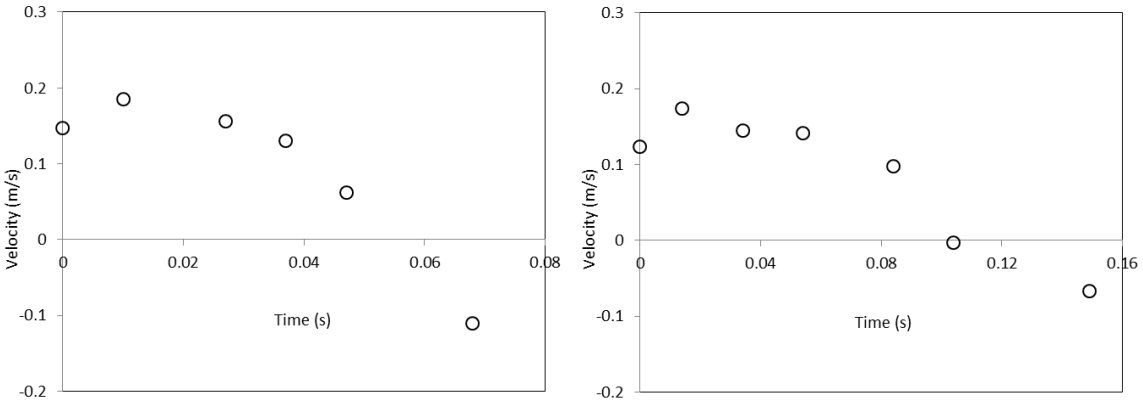


Figure 3-11 Velocity profiles of two selected bubbles in Figure 3-10 (both glass and aluminum channel)

As the incoming flow continues to decelerate caused by the longitudinal expansion of the vapor slugs, the flow in the downstream accelerates. Figure 3-12 shows the flow

regimes, which is soon after flow reversal was spotted. The velocities of the downstream edge of the selected vapor slugs (marked by red) in both channels demonstrate a trend of acceleration, as is shown in Figure 3-13.

Along with the deceleration of the incoming flow, the highest pressure within the entire channel propagates from the inlet to downstream. This phenomenon is numerically illustrated in Li and Hrnjak (2017a). The vapor slugs in the glass and aluminum channels selected in Figure 3-12 are believed to have the highest pressure. Although the local pressure is not directly measured, the flow directions upstream and downstream of that vapor slug indicate the existence of the pressure peak.

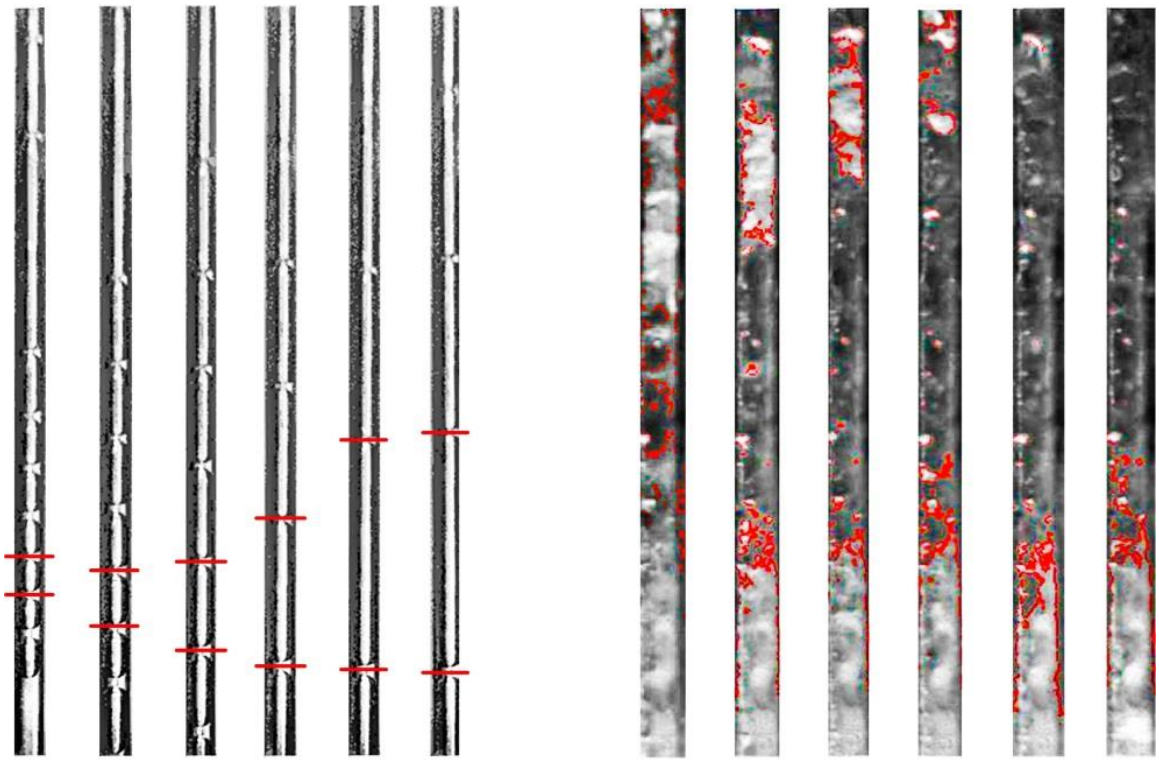


Figure 3-12 Flow regime development at a late stage of a periodic cycle (glass and aluminum channels)

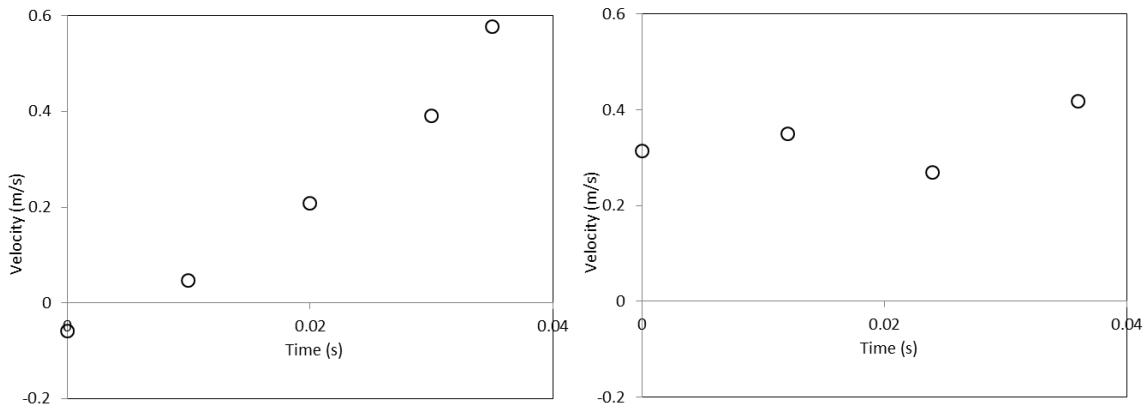


Figure 3-13 Velocity profiles of two selected bubbles (downstream) in glass and aluminum channel respectively

The channels become emptier after continuous evaporation and venting of liquid and vapor from both the inlet and outlet. Up to a certain point, the pressure build-up in the inlet header will push fresh liquid refrigerant into the channel to start a new cycle.

Comparing with the FGBR mode, it is two-phase refrigerant feeding a channel in DX mode instead of liquid refrigerant. There is higher frictional resistance located at the upstream part of a channel in DX mode which results in less flow reversal (introduced in Chapter 3.3.1).

## 3.4 SUMMARY AND CONCLUSIONS

In this chapter, flow regimes in an air heated aluminum channel (a part of an operating microchannel evaporator) are visualized for the first time in the literature, to the best of the author's knowledge.

Visualization is focused on the first one third of the channel. In DX mode, three typical flow regimes are identified as: churn flow, bubbly/slug flow and annular flow.

They occur alternatively with variable period. Flow reversal is witnessed occasionally and only in bubbly/slug flow regime. In FGBR mode, only liquid and bubbly/slug flow are observed. Forward and reverse flow occurs periodically.

In FGBR mode, after liquid just enters the channel, the newly generated bubbles or slugs may experience a short period of acceleration. As liquid continue to evaporate, the rapid expansion of the vapor slug in the longitudinal direction accelerates the downstream flow and decelerates the upstream flow. When the downstream resistance is high enough, flow reversal occurs. In DX mode, flow reversal is much less compared with FGBR mode, which is due to higher upstream resistance caused by two-phase refrigerant feeding.

# Chapter 4 MODELING OF BUBBLE DYNAMICS IN SINGLE DIABATIC MICROCHANNEL

## 4.1 INTRODUCTION

The focus of this chapter is to develop a mechanistic model which is capable of simulating multiple bubble dynamics inside of single microchannel. This model will be validated against the visualization results of the flow regime inside of a microchannel. The validated model can be used as a tool to demonstrate the mechanism of flow reversal during in-tube flow boiling.

## 4.2 EXPERIMENTAL SETUP

The schematic drawing of the facility is shown in Figure 3-1. The microchannel evaporator has a single pass and single slab which is specially designed for the experimental purpose. The length of the finned tube is 190 mm. The whole heat exchanger consists of 25 tubes. Inside of each tube, there are 10 parallel microchannels with the hydraulic diameter of 1.4 mm. In order to measure the flow rate of reversed vapor, the FGBR configuration is employed (as shown in Figure 3-2).

The visualization results used in this work is from Tuo and Hrnjak (2014a). In that study, one transparent glass tube is placed in front of one aluminum microchannel tube. The glass tube has an inner diameter of 1 mm which is similar to the hydraulic diameter of the aluminum tube (1.4 mm). Inlet and outlet of the glass tube are inserted into the

inlet and outlet headers respectively, so that the glass tube is subject to the same pressure field and flow regime as the nearby aluminum tubes. As shown in Figure 4-1, three Nichrome resistance wires are glued to the outer surface of the glass tube by thermal paste. An adjustable DC voltage is applied on the resistance wire to provide heating. Firstly, the DC voltage is roughly adjusted untill there is only single phase vapor in S5 region (shown in Figure 3) (maybe with a few randomly entrained droplets). Finally, the DC voltage is finely tuned to the point that the glass tube has the same temperature in S5 region with the nearby aluminum tubes. The surface temperatures of the glass tube and aluminum tube are measured by an infrared camera. Since emissivities of glass and aluminum surfaces (with lots of cavities created by fins) are fortunately very close, the same surface temperature indicated similar refrigerant-side superheat. After the aforementioned adjustment, a reasonable heating power is determined under which the flow regime in the glass tube is believed to be very similar with that in nearby aluminum tubes. A small portion of the frontal area of the glass tube is left transparent (no thermal paste is applied) to enable visualization. A high speed CCD camera is used to record the transient flow regime in all five regimes of the glass tube. The recording speed is 1000 frame/s and the resolution of the each frame is 512 × 512 pixels. In order to ensure enough resolution, the flow regime in each region (S1 to S5) is filmed individually. Only the visualization in S1 is used in this study because that is where flow reversal happens. Regions S2-S5 are mainly occupied by long vapor slugs or annular flow.

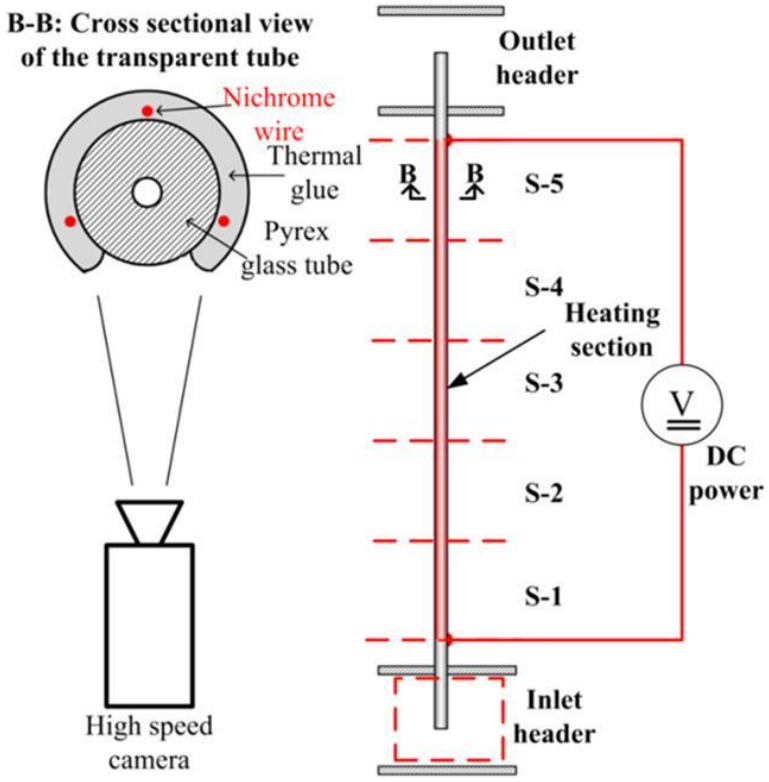


Figure 4-1 An electric heating transparent glass tube is used for flow visualization

Based on visualization, Tuo and Hrnjak (2014a) summarized nine typical flow patterns within one periodic cycle and presented them in chronological order in Figure 4-2. Since the flow regimes in S2-S5 regions are elongated bubble, annular or dryout, only the nine typical flow regimes in S1 region are shown in Figure 4-3.

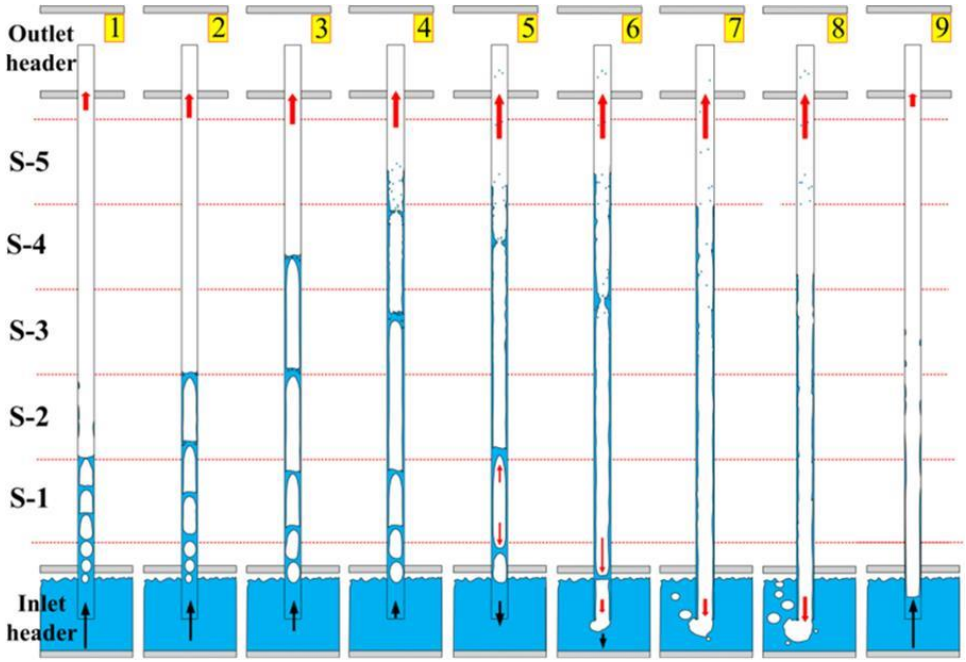


Figure 4-2 Transient flow patterns and flow dynamics in one channel within one periodic cycle (Tuo and Hrnjak, 2014a)

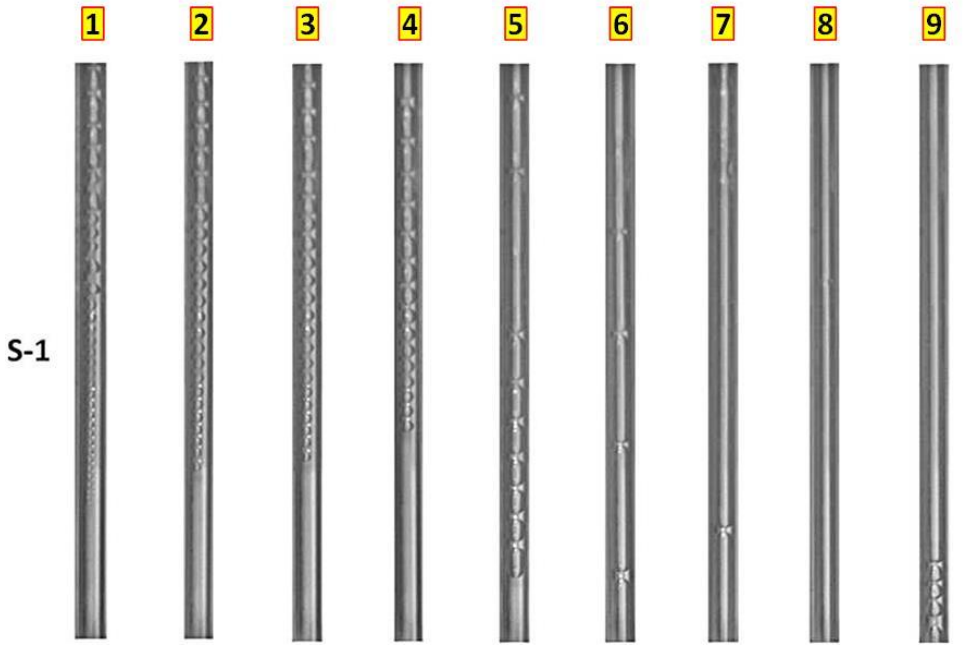


Figure 4-3 Typical flow regimes in S1 region corresponding to Figure 4-2

Improvement of the visualization technique by inserting transparent surface in a genuine microchannel evaporator presented essentially the same physics in Li and Hrnjak (2017b).

## 4.3 MODEL DESCRIPTION AND VALIDATION

### 4.3.1 MODEL DESCRIPTION

In this model, each bubble generated on the nucleation site acts like a ‘‘shutter’’, which divides liquid refrigerant into successive liquid slugs. The same idea is presented in Thome *et al*.’s (2004) heat transfer model in a microchannel. This model applies mass, momentum and energy conservation on each vapor and liquid segment, and eventually connects them together to satisfy the boundary condition and form the complete system. The growth of each bubble can be divided into two stages: partial confinement stage and full confinement stage. Partial confinement stage is defined as the period from the nucleation to the detachment of the bubble. Full confinement stage starts from bubble detachment and ends at the depletion of the bubble.

The following major assumptions are made in developing the model.

1) Only one nucleation site (located at 10D from the inlet) exists in one channel (even though there are multiple nucleation sites, small bubbles will soon merge into one bigger slug).

2) The flow regimes in this model only include bubbly, slug and annular flow.

3) When the diameter of a bubble reaches 95% of the tube diameter, it detaches from the wall and can only grow longitudinally afterwards.

4) A detached bubble has to travel at least a diameter away from the nucleation site before the next bubble can be generated, and no new bubble will be generated if the nucleation site is subject to reverse flow (based on visualization results).

5) The heat flux is constant and uniform in time along tube walls.

6) All heat is used to evaporate liquid refrigerant and there is no superheat state.

7) The local thermophysical and transport properties are determined from the local pressure.

8) The liquid film remains attached to the wall and has constant thickness (0.025D). (Evaporation only happens at both ends of a vapor slug and not at the film)

9) Heat conduction along channel wall is neglected.

10) Thermal mass of channel wall is neglected.

11) The inlet and outlet pressure is constant and decoupled with the bubble dynamics inside of the channel.

Assumptions 1,3 and 4 are based on experimental observation. A more mechanistic approach to model bubble nucleation and detachment is currently under development, which includes the effect of surface condition of the channel wall and surface tension of the refrigerant. Ideally this mechanistic modeling of bubble nucleation and detachment will eliminate assumptions 1,3 and 4.

#### 4.3.1.1 PARTIAL CONFINEMENT STAGE

Once a bubble is generated on the nucleation site, the growth rate of the bubble should be ideally described by formulas that were developed to model bubble growth near a heated surface, for instance Mikic and Rohsenow (1969), but typically these correlations includes many immeasurable parameters in our facility, such as the size of the active nucleation sites. In the end, a correlation for bubble growth in an extensive liquid pool was adopted, which was proposed by Plesset and Zwick (1954).

$$r(t) = Ja\sqrt{\frac{12\alpha_t t}{\pi}} \quad \left( Ja = \frac{\rho_l c_{pl}}{\rho_v \Delta h_{lv}} \Delta T_{sat} \right) \tag{4-1}$$

The bubble generation frequency is obtained from the visualization of the glass tube, which is around 1000 Hz. As long as a bubble is attached on the tube wall, it is in the partial confinement stage which means it can grow freely in all directions except towards the tube wall.

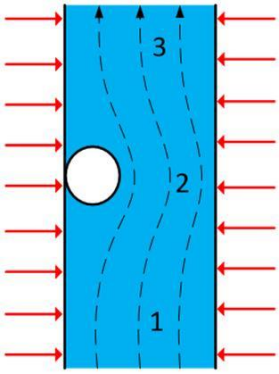


Figure 4-4 Flow regime in partial confinement stage

Due to the transient nature of boiling instabilities, the flow in regions 1, 2 and 3 (as shown in Figure 4-4) can be either laminar or turbulent. Since the Churchill equation (1977) covers laminar, transitional and turbulent flow, it is used to calculate the Darcy

friction factor of liquid flow in regions 1, 2 and 3 (also used in all later single phase frictional pressure drop calculations). An additional feature of the Churchill equation is that it can apply for developed laminar, developed turbulent and developing turbulent flow, but its feasibility to model developing laminar flow pressure drop needs further investigation.

$$f_{Darcy} = 8[(\frac{8}{\mathrm{Re}})^{12} + \frac{1}{([-2.457\ln[(\frac{7}{\mathrm{Re}})^{0.9} + 0.27\frac{\varepsilon}{D}]]^{16} + (\frac{37530}{\mathrm{Re}})^{16})^{1.5}}]^{\frac{1}{12}} \quad (4\text{-}2)$$

Due to the existence of the bubble in region 2, there exists contraction pressure drop from region 1 to region 2 and expansion pressure drop from region 2 to region 3. The contraction and expansion pressure loss coefficients are calculated according to Idel'chik (1994).

$$K_{se} = K_{correction}(1 - \frac{A_{small}}{A_{large}})^2 \quad (4\text{-}3)$$

$$K_{sc} = K_{correction}(1 - \frac{A_{small}}{A_{large}})^{0.75} \quad (4\text{-}4)$$

#### 4.3.1.2 FULL CONFINEMENT STAGE

Once a bubble detaches from the wall, it becomes a slug and can only grow only longitudinally. As refrigerant keeps evaporating, the length of a liquid slug sandwiched between two vapor slugs decreases, and when the length is less than 5% (assumption based on visualization) of the hydraulic diameter, two vapor slugs coalesce (shown in Figure 4-5). As the leading edge of the first vapor slug travels to the outlet of the tube, the slug becomes annular flow (shown in Figure 4-5).

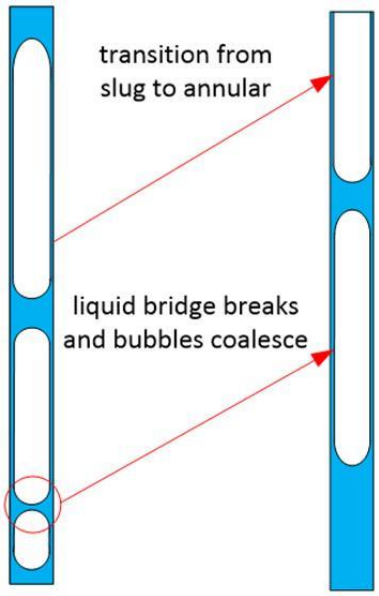


Figure 4-5 Illustration of flow regime transition

The model treats each vapor and liquid slug as a finite volume as shown in Figure 4-6 and applies mass, momentum and energy conservation to each of them. For each liquid slug, Newton's second law for a variable mass system is applied to describe the momentum conservation.

$$P_{i-1,d}A - P_{i,u}A + F_{fric,l,i} + m_{l,i}g + \frac{1}{2}V_{rel,i,u}\dot{m}_{evap,i,u} + \frac{1}{2}V_{rel,i-1,d}\dot{m}_{evap,i-1,d} + \sigma_{i,u}L_{wetting,u} + \sigma_{i-1,d}L_{wetting,d} = m_{l,i}\frac{dV_i}{dt} \tag{4-5}$$

In the above equation, the rate of momentum exchange (caused by evaporation) and force caused by surface tension on both ends of the liquid slug are assumed to have the same magnitude but opposite sign. In the end, the momentum equation can be simplified as follow:

$$P_{i-1,d}A - P_{i,u}A + F_{fric,l,i} + m_{l,i}g = m_{l,i}\frac{dV_i}{dt} \tag{4-6}$$

The mass and energy conservation equations for each liquid slug are formulated in equations (4-7) and (4-8). $L_{l,i}$ is the length of the corresponding liquid slug. $L_{v,i-1}$ and $L_{v,i}$ are the lengths of the upstream and downstream vapor slugs. Since all heat input is used to evaporate liquid refrigerant, the mass conservation equation and energy conservation equation can be coupled together.

$$\frac{dm_{l,i}}{dt} = \dot{m}_{evap,i,u} + \dot{m}_{evap,i-1,d} \tag{4-7}$$

$$\frac{dm_{l,i}}{dt}h_{lv} = (\dot{m}_{evap,i,u} + \dot{m}_{evap,i-1,d})h_{lv} = \dot{q}\pi D(L_{l,i} + \frac{L_{v,i-1}}{2} + \frac{L_{v,i}}{2}) \tag{4-8}$$

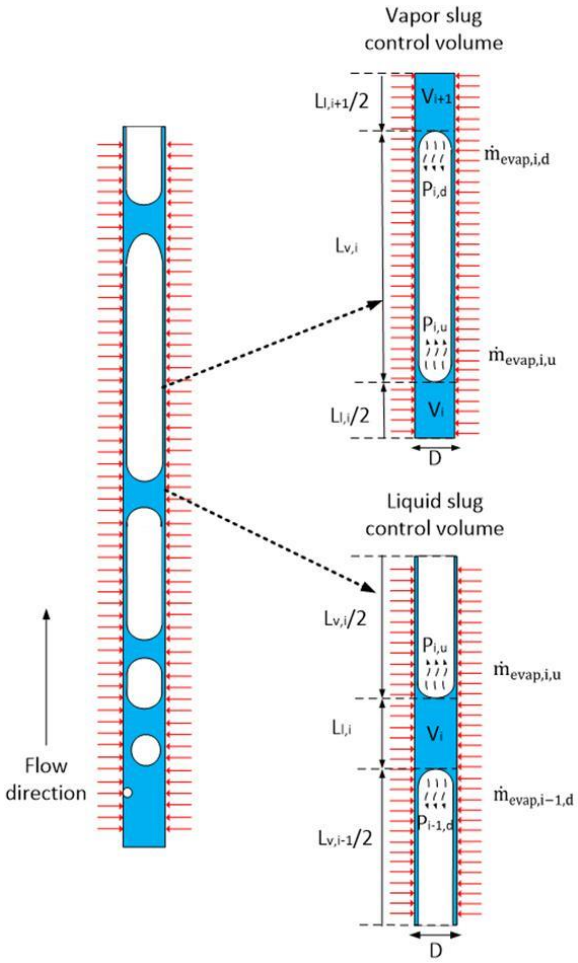


Figure 4-6 Control volumes for liquid and vapor slugs

Following the same logic, the momentum equation for each vapor slug is formulated as equation (4-9). It is assumed that half of the vapor slug has the velocity of the upstream liquid slug and the other half has the velocity of the downstream liquid slug.

$$P_{i,u}A - P_{i,d}A + F_{fric,v,i} = m_{v,i}\frac{d(V_i/2 + V_{i+1}/2)}{dt} \tag{4-9}$$

The mass and energy conservation equations for the vapor slug are shown as follows. $L_{v,i}$ is the length of the corresponding vapor slug and $L_{l,i}$ and $L_{l,i+1}$ are the lengths of the upstream and downstream liquid slugs.

$$\frac{dm_{v,i}}{dt} = \dot{m}_{evap,i,u} + \dot{m}_{evap,i,d} \tag{4-10}$$

$$\frac{dm_{l,i}}{dt} h_{lv} = (\dot{m}_{evap,i,u} + \dot{m}_{evap,i,d}) h_{lv} = \dot{q} \pi D (L_{v,i} + \frac{L_{l,i}}{2} + \frac{L_{l,i+1}}{2}) \tag{4-11}$$

Since vapor is incompressible, the increase of mass is proportional to the increase of the volume.

$$\frac{dm_{v,i}}{dt} = \rho_v A \frac{dL_{v,i}}{dt} \tag{4-12}$$

The increase of the bubble length is caused by the velocity difference on both ends and the decrease in length of the liquid slug located upstream and downstream.

$$\frac{dL_{v,i}}{dt} = V_{i+1} - V_i + \dot{q} \pi D (\frac{L_{l,i}}{2} + \frac{L_{v,i}}{2}) / \rho_l A h_{lv} + \dot{q} \pi D (\frac{L_{l,i+1}}{2} + \frac{L_{v,i}}{2}) / \rho_l A h_{lv} \tag{4-13}$$

Combining equation 4-10 to 4-13, a relationship between velocity and heat flux can be built.

$$V_{i+1} - V_i = \frac{\dot{q} \pi D (L_{v,i} + \frac{L_{l,i}}{2} + \frac{L_{l,i+1}}{2})(1 - \frac{\rho_v}{\rho_l})}{\rho_v A h_{lv}} = \frac{4 \dot{q} (L_{v,i} + \frac{L_{l,i}}{2} + \frac{L_{l,i+1}}{2})(1 - \frac{\rho_v}{\rho_l})}{\rho_v D h_{lv}} \tag{4-14}$$

Once boundary conditions are specified (fixed inlet and outlet pressures are currently used in the model), equations (4-6), (4-8), (4-9), (4-11), (4-12), (4-13), (4-14) can be solved iteratively to determine the velocity and location of each liquid and vapor slug.

### 4.3.2 MODEL VALIDATION

Visualization results from Tuo and Hrnjak (2014a) are used to validate the simulation results. The operating conditions of the experiments (using R134a as the refrigerant) are

summarized in Table 4-1, and the same conditions are used as inputs in the model. Pressure drop in the model is modified to be 0.7 kPa to better match with the flow visualization results.

Table 4-1 Experimental conditions

| Items | Unit | Value |
|---|---|---|
| Evaporation pressure | kPa | 343 |
| Heat flux | $kW/m^2$ | 10.6 |
| Pressure drop | kPa | 0.3 |

Figure 4-7 shows the comparison of bubble movement in experiment and simulation. The locations of three selected liquid slugs are highlighted using green, red and blue lines. The difference between them is the length of a vapor slug. The left figure consists of nine snapshots taken from a high speed video of the diabatic in-tube flow. The right figure is generated using the numerical values of the vertical locations of liquid and vapor slugs at the same times as in the experiment. The model captures the entire process well with reasonable quantitative agreement, and most importantly, the transient flow directions: forward-reverse-forward.

Figure 4-8 shows the comparison of bubble velocity in experiment and simulation for the same condition as above. The velocities in experiment are calculated using the traveling distance of a certain liquid slug divided by the corresponding time interval. The right figure is generated using the numerical values of the velocities of liquid and vapor slugs at the same times as in the experiment. The model is able to predict that the selected three liquid slugs begin to reverse around 20 ms, and the velocity of the top liquid slug

(green line) increases back to positive value around 50 ms followed by the next two liquid slugs. The bubble velocities of all three slugs seem to be the same before 15ms in the experiment. This is most likely because the majority of the heat input is used to superheat the new coming liquid refrigerant, but this factor is not considered in the model.

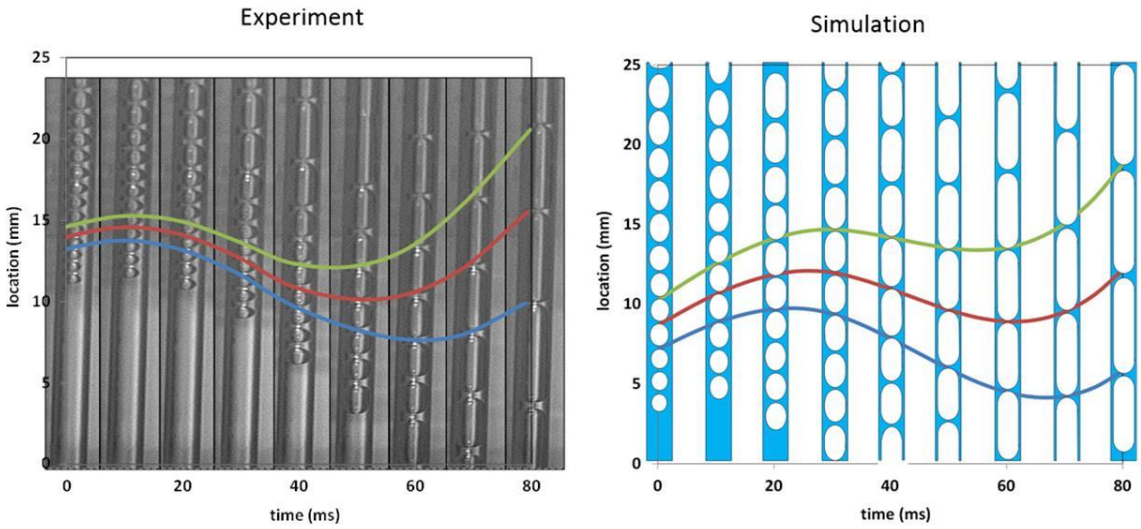


Figure 4-7 Transient flow regime validation

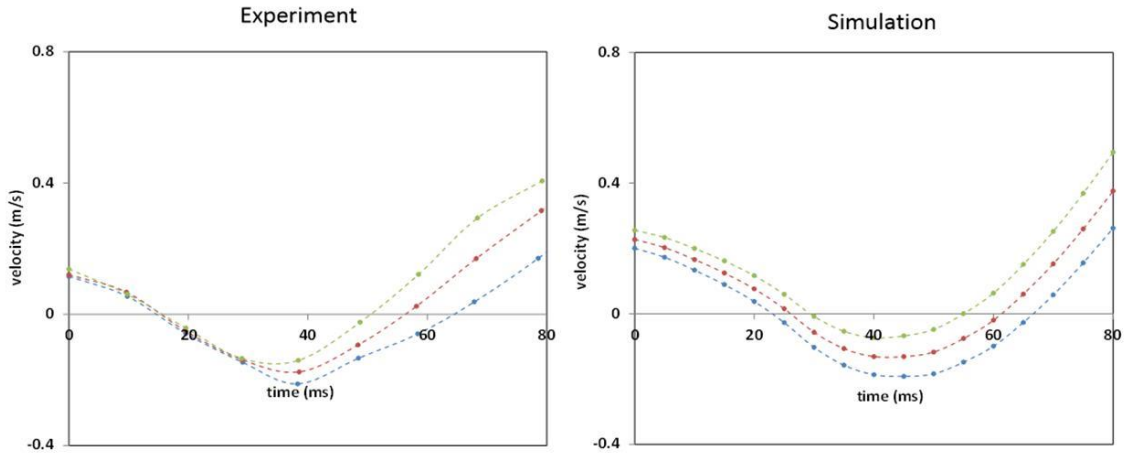


Figure 4-8 Transient velocity validation

## 4.4 DISCUSSION

Figure 4-9 demonstrates the transient mass flux at the inlet of the microchannel under the same simulating conditions as introduced in Chapter 4.3. The change of the mass flux corresponds well with the transient flow pattern introduced in Tuo and Hrnjak (2014a) as shown in Figure 4-2.

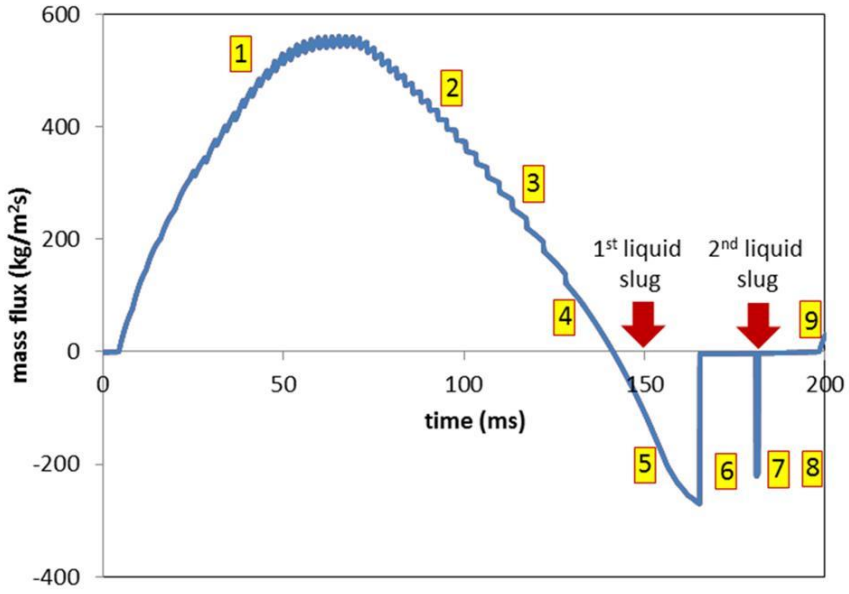


Figure 4-9 Mass flux at the tube inlet during one periodic cycle as modeled

The pressure distributions along the channel at nine selected states, which determines the transient flow regime, are presented in Figure 4-10. At state 1, fresh liquid flows into the tube. Since the tube is relatively empty at this point with large portion of elongated vapor slug (or dryout) at the downstream, the incoming liquid accelerates due to small flow resistance at the downstream. As shown in Figure 4-10 (state 1), the pressure gradient is higher at the upstream (liquid rich slug flow) than the downstream (vapor rich slug flow, annular flow or dryout) due to higher viscosity of the liquid refrigerant than the

vapor refrigerant. From state 2 to 4, caused by continuous liquid evaporation, the downstream part of the flow is accelerated, which creates higher downstream frictional resistance. As a result, the incoming flow decelerates. The aforementioned phenomenon can also be reflected in Figure 4-10; the pressure drop gradient becomes more flattened at the upstream, while steeper at the downstream. At state 5, the highest pressure was generated at 2% of the channel length instead of at the inlet, indicating the beginning of flow reversal. As is indicated in Figure 4-9, the inlet mass flux becomes negative at state 5. From state 6 to 8, up to 6.5% of the tube length after the inlet experiences positive pressure gradients. The highest pressure during the whole cycle is generated at state 7 (75% of the cycle time), which elevates the pressure drop (difference between the highest and the lowest pressures along the channel. The lowest pressure is always located at the outlet) by 3%. Due to the positive pressure gradient at the upstream, liquid slugs and vapor slugs are expelled out of the channel not only from the outlet but also from the inlet. As is indicated in Figure 4-9 by red arrows, the sudden increase of negative mass flux is caused by the venting of liquid slugs at the inlet. In between liquid slugs, it is the venting of vapor slugs, which creates almost zero negative mass flux. At state 9, the tube becomes empty after the continuous evaporation and venting of liquid and vapor slugs, and fresh liquid refrigerant flows into the channel to start a new cycle.

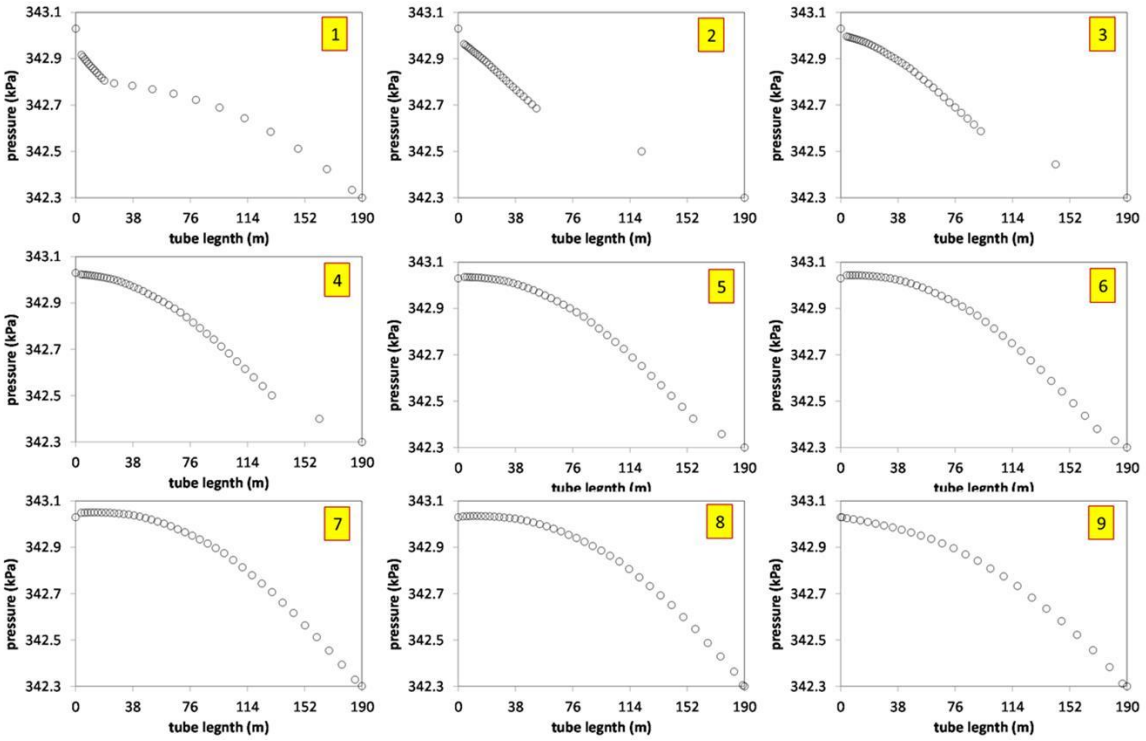


Figure 4-10 Pressure distribution along the channel within one periodic cycle

## 4.5 IMPROVEMENT OF THE CURRENT MODEL

One major limitation of the model is the fixed heat flux throughout the channel wall. In that case, the information of local heat transfer coefficient is missing. In this chapter, air side conditions including temperature and velocity are imposed for each channel, and the heat flux is calculated based on air side and refrigerant side heat transfer coefficients. A detailed correlation selection for this model is summarized in Chapter 5, Chapter 6 and Chapter 7.

Table 4-2It is assumed that there is always liquid film covering the wall in the vapor slug and annular flow region, and the film thickness is constant. All evaporation is assumed to happen on the vapor-liquid interfaces that are perpendicular to the flow

direction. The value of film thickness in the model is determined based on the best matching with the experimental capacity data. This improved model will be used for all the simulations in Chapter 5, Chapter 6 and Chapter 7.

Table 4-2 Correlations of heat transfer and pressure drop in the model

| | | Liquid slug | Vapor slug | Annular flow |
|---|---|---|---|---|
| Ref side | Heat transfer | Incropera & DeWitt (2002) and Gnielinski (1976) | Kattan *et al.* (1998) | Kattan *et al.* (1998) |
| | Pressure drop | Churchill (1977) | Abiev (2011) | Field & Hrnjak (2011) |
| Air side | Heat transfer | Kim & Bullard (2002) | | |

## 4.6 SUMMARY AND CONCLUSIONS

A mechanistic model of bubble dynamics in single microchannel is developed and presented. The comparison between high speed visualization and simulation results shows that the model is capable of capturing the transient flow regime and slug velocity inside of a single microchannel and predicting flow reversal.

Combing with the transient flow patterns developed by Tuo and Hrnjak (2014a), the model quantitatively demonstrates the mechanism and evolution of flow reversal: at the beginning of one periodic cycle, fresh liquid refrigerant accelerates in the channel due to smaller downstream resistance; as continuous evaporation accelerates the downstream velocity, which increases the downstream frictional resistance, the incoming flow decelerates; as downstream resistance continues to build up, the highest pressure in the tube gradually propagates from the inlet to downstream (highest pressure is located at up to 6.5% of channel length and pressure drop is elevated by up to 3% in our case), the

resulting positive pressure gradient causes flow reversal; After continuous evaporation and depletion of working fluid from both inlet and outlet, the downstream resistance decreases and fresh liquid flows into the empty tube again to start a new cycle.

# Chapter 5 EFFECT OF CHANNEL GEOMETRY ON FLOW REVERSAL IN MICROCHANNEL EVAPORATORS

## 5.1 INTRODUCTION

The focus of this chapter is to experimentally and numerically investigate the effect of channel diameter and length on flow reversal. Microchannel evaporators with different diameters and lengths are tested under the same heat flux and superheat. The flow rate and frequency of reversed vapor are recorded. Meanwhile, the mechanistic model that is introduced in Chapter 4 is further validated using experimental results. The simulation results are used to explain the effect of different geometries on flow reversal.

## 5.2 EXPERIMENT DESCRIPTION

The schematic drawing of the facility is shown in Figure 3-1. The fixed displacement compressor (driven by a variable speed motor) and the microchannel condenser are components that are used in a major brand vehicle. Three different microchannel evaporators are examined in the system with detailed geometry summarized in Table 5-1. Two heat exchangers have identical channel length but different channel diameters, and the cross sectional views of two microchannels are shown in Figure 5-1. Another two heat exchangers are made of the same microchannels, so they share the same diameter but have different lengths. In order to measure the flow rate of reversed vapor, the FGBR system is employed again (as shown in Figure 5-2). In this study, the headers of all heat exchangers are intentionally oversized to eliminate as much header pressure drop-induced

refrigerant maldistribution as possible (Tuo and Hrnjak (2013c)). Refrigerant distribution is maintained nearly uniform for all heat exchangers.

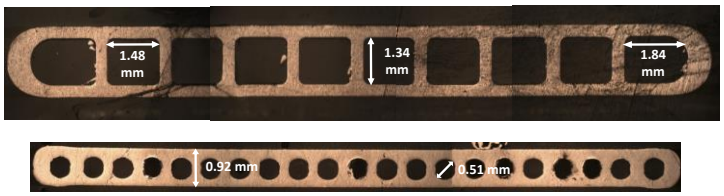


Figure 5-1 Cross-section of two types of microchannel evaporators examined

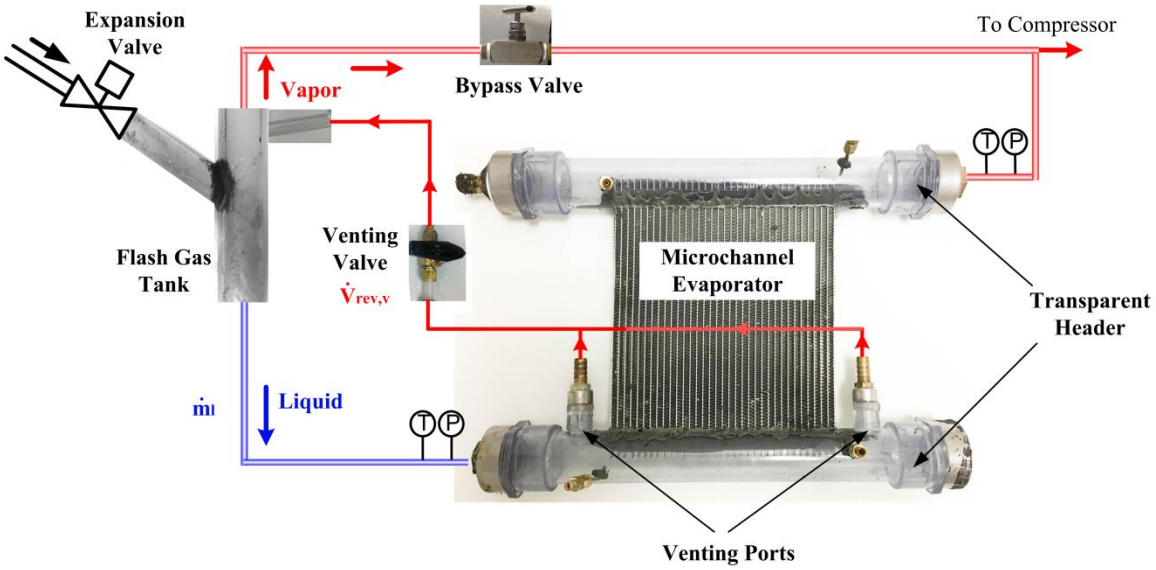


Figure 5-2 Evaporator setup in FGBR mode

Table 5-1 Key geometries of three different heat exchangers (HX)

| | Hydraulic diameter (mm) | Number of tubes | Channels /tube | Length (mm) | Refrigerant-side area /channel ($mm^2$) |
|---|---|---|---|---|---|
| HX 1 | 0.5 | 35 | 21 | 190.0 | 304.4 |
| HX 2 | 1.4 | 25 | 10 | 190.0 | 1099.9 |
| HX 3 | 0.5 | 35 | 21 | 510.0 | 817.1 |

## 5.3 RESULTS AND DISCUSSIONS

Hydraulic diameter and length are the two defining parameters of a microchannel. In this chapter, two set of experiments, which use heat exchangers with identical length but different diameters and heat exchangers with identical diameter but different lengths are carried out to demonstrate the effect of channel diameter and length on flow reversal. Meanwhile, simulations corresponding to each test are performed and the results are used to explain the experimental phenomena.

### 5.3.1 EFFECT OF CHANNEL DIAMETER

HX1 and HX2 are chosen in this study, since they have the same channel length (190 mm) but different channel diameters (0.5 mm and 1.4 mm). Similar operation conditions are imposed for both heat exchangers (around 7.5 kW/m$^2$ heat flux and 6.7 ºC superheat). As shown in Figure 5-3 and Figure 5-4, the reversed vapor flow rate and pressure drop oscillate periodically in both heat exchangers, but the oscillation is more distinct in HX2 with higher amplitude. Through Fast Fourier Transformation (FFT) of the temporal data, the dominant frequency in HX1 is identified to be 1.31 Hz, as shown in Figure 5-3. In HX2, the dominant frequency of oscillation reduces to 0.81 Hz, but the amplitude significantly increases. Although heat flux is kept the same for both heat exchangers, the total liquid flow rate supplied to each heat exchanger can be different, because they have difference refrigerant-side heat transfer areas. For instance, the supplied liquid flow rate to HX1 is 8.2 g/s, while the mass flow rate of HX2 is 10.9 g/s. The volumetric flow rate of reversed vapor normalized by the mass flow rate of the supplied liquid refrigerant ($\dot{V}_{rev,v}/\dot{m}_l$) (referred as normalized volumetric flow rate of reversed vapor in later text) is

employed to quantify the intensity of flow reversal. The reasons why this parameter is selected are following: 1) One of the major effects of reverse flow in microchannel evaporators is that the reversed vapor can deteriorate the refrigerant distribution in the inlet header. The size of the vapor pocket in the inlet header, which obstructs continuous liquid feeding, is determined by the volume of the reversed vapor rather than the mass, so volumetric flow rate instead of mass flow rate is chosen as the numerator. As for the denominator, simply because mass flow rate is directly connected with evaporator capacity which engineers care the most in reality, it is selected instead of the volumetric flow rate. 2) Both flow rates can be experimentally measured (shown in Figure 5-2) and this parameter can serve as a validation for the model. The normalized volumetric flow rate of reversed vapor in HX1 (6.3 L/kg) is higher than that in HX2 (3.2 L/kg). In the current test facility, only reversed vapor flow rate can be measured. Given the fact that the density of liquid is much higher than vapor, the flow rate of reversed liquid refrigerant is expected to be higher than that of the vapor.

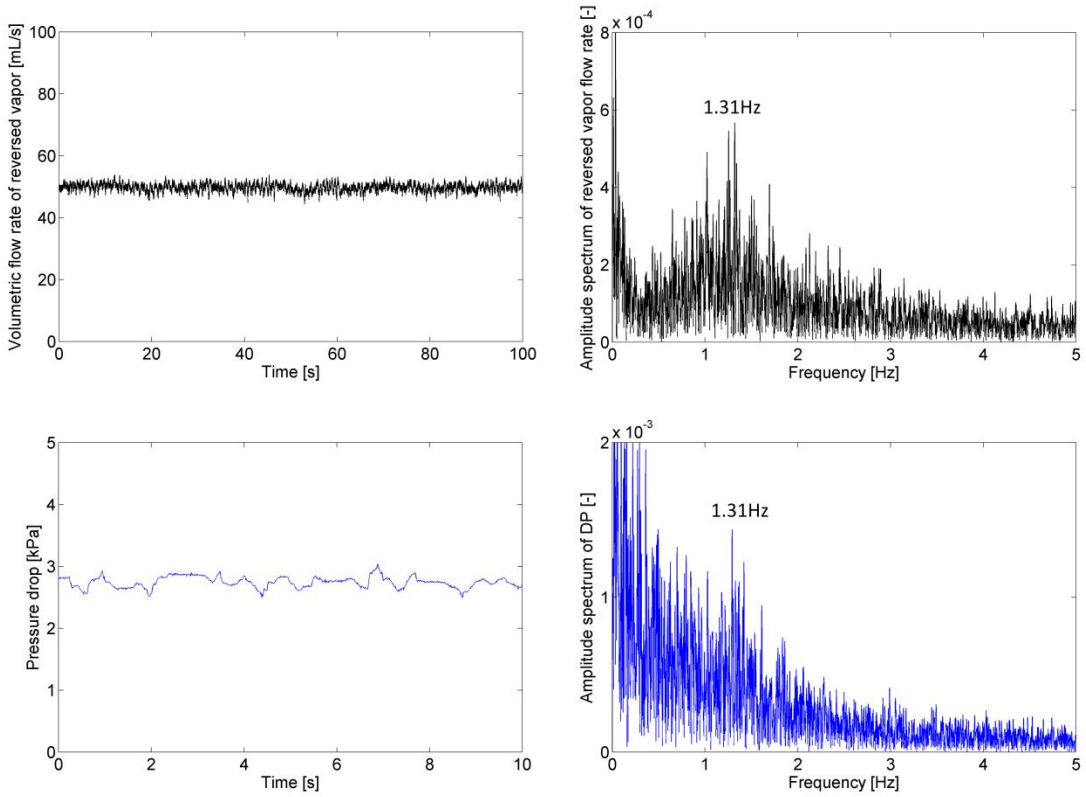


Figure 5-3 Temporal variation and frequency analysis of the reversed vapor flow rate and pressure drop in HX1

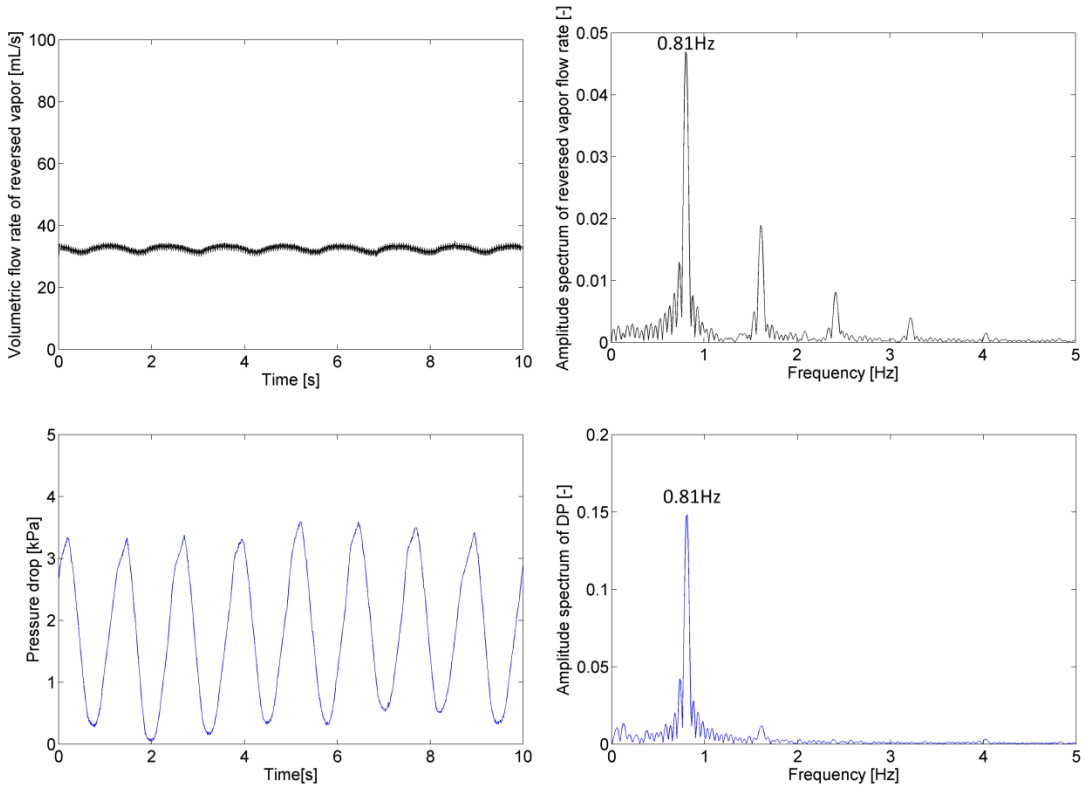


Figure 5-4 Temporal variation and frequency analysis of the reversed vapor flow rate and pressure drop in HX2

Bubble dynamics in these two channels are simulated using the model that is introduced in Chapter 4. The same air side conditions (temperature and velocity) and channel geometries as in the experiments are imposed in the model. Pressure drops in the models are adjusted so that the simulated mass fluxes match with the corresponding experimental results. Figure 5-5 shows the flow regime and pressure development within one periodic cycle for R134a in a channel with 0.5 mm diameter and 190 mm length. On the left side of Figure 5-5, blue lines and red lines are used to track the locations of the upstream and downstream edge of each vapor slug in time. A schematic of the in-tube flow regime is employed (also shown on the left side of Figure 5-5) to illustrate the

physical interpretation of the red and blue lines. Two dashed lines mark the beginning and end of a periodic cycle. The in-tube pressure development within one cycle is shown on the right side of Figure 5-5, and it corresponds to the flow regimes between the dashed lines on the left. The highest and lowest pressures during the entire cycle are selected as the upper and lower limits of the color bar to maximize the resolution. It can be seen that as the rapid bubble growth continues to accelerate the downstream flow and decelerate the upstream flow, the highest pressure inside of a channel migrates from the inlet towards downstream. In this case, the highest pressure occurs at 74% of the entire period and at 34% of the tube length from the inlet.

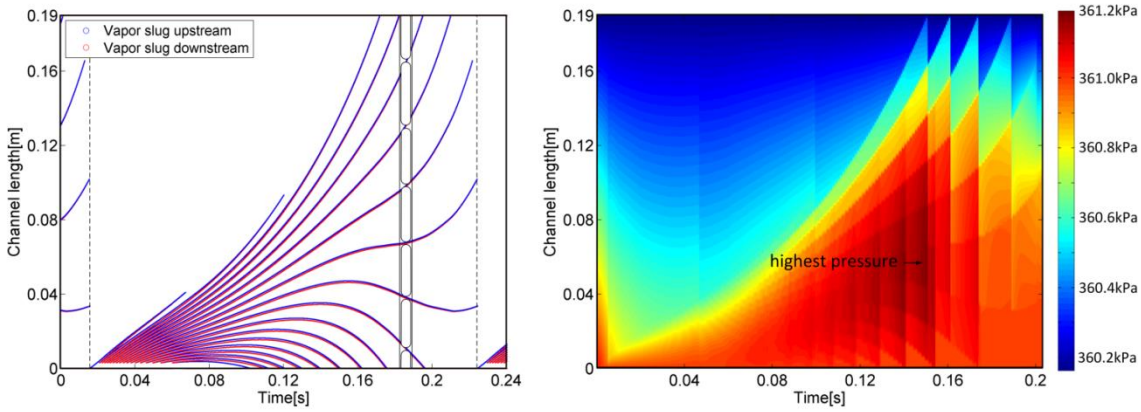


Figure 5-5 Flow regime and pressure development within one periodic cycle for R134a in a channel with 0.5 mm diameter and 190 mm length

Figure 5-6 shows the same content as in Figure 5-5, but in a tube with 1.4 mm diameter and 190 mm length. It can be seen from the comparison of flow regimes in Figure 5-5 and Figure 5-6 that flow reversal is less likely to happen in the channel with a larger diameter. The pressure development also indicates the same information: the highest pressure only propagates to 3% of the tube length from the inlet, and it occurs at 88% of the entire period. Due to the milder pressure oscillation and slower velocity, the

frequency of flow reversal in this case is lower than that of the channel with smaller diameter.

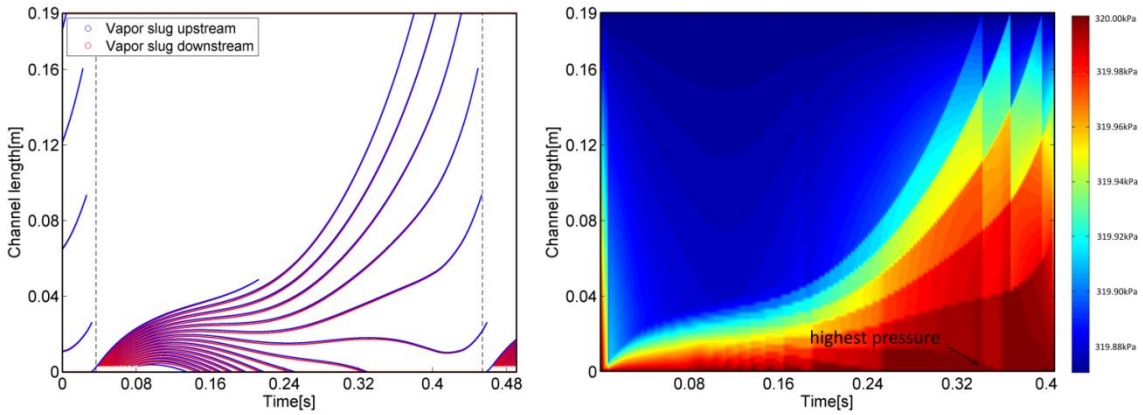


Figure 5-6 Flow regime and pressure development within one periodic cycle for R134a in a channel with 1.4 mm diameter and 190 mm length

Figure 5-7 summarizes the comparison between experimental and simulation results of flow reversal ratio and frequency. The model is able to capture the normalized volumetric flow rates of reversed vapor fairly accurately. As for the frequency, the model is only capable of predicting the qualitative trend: larger diameter leads to lower frequency. One possible reason for the discrepancy is following: the measured frequency including more influential factors (such as the inlet header and hundreds of other microchannels) than the simulated. In the experiment, the reversed vapor flow from all channels merges in the inlet header, then being vented and measured. The inlet header with large compressible volume might serve as a buffer to reduce the frequency, making the measured results much lower than the simulated single channel frequency.

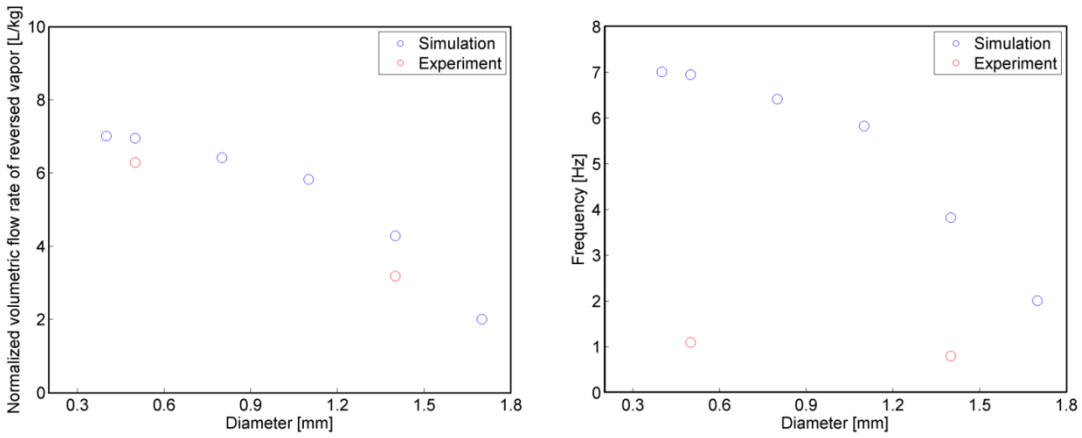


Figure 5-7 Both simulation and experiment show that normalized volumetric flow rate of reversed vapor and frequency decrease with larger channel diameter (under 7.5 kW/m$^2$ heat flux and 6.7 ℃ superheat)

In order to explain the difference of flow reversal between channels with different diameters, equation 4-14 has to be revisited. The velocity difference between any two neighboring liquid slugs is inversely proportional to the channel diameter. Under the same heat flux, smaller channel diameter leads to more rapid growth of a bubble, so the velocity difference between upstream and downstream flow becomes larger. Since the frictional resistance created by liquid or vapor slugs is proportional to the velocity squared, it is concentrated more on the downstream in the channel with a smaller diameter. Due to a higher downstream frictional resistance, the upstream flow in smaller channels tends to decelerate quicker and the pressure peak migrates further toward the downstream.

### 5.3.2 Effect of Channel Length

In this study, HX1 and HX3 are chosen since they have the same channel diameter (0.5 mm) but different channel length (190 mm and 510 mm). Similar operation

conditions are imposed for both heat exchangers (around 7.5 kW/m$^2$ heat flux and 6.7°C superheat). In Figure 5-8, pressures at the inlet and outlet of the evaporator are chosen instead of the pressure drop due to better measurement quality of the absolute pressures in this case. By comparing Figure 5-3 and Figure 5-8, it can be seen that the oscillation amplitude of reversed vapor flow is higher in HX3 than in HX1, but the frequency is lower. Larger oscillation is due to the fact that the longer tube contains more refrigerant mass, and a larger quantity of vapor is vented within one periodic cycle. At the same time, more inertia associated with more refrigerant mass slows down the periodic process, which contributes to lower frequency. The normalized volumetric flow rate of reversed vapor in HX3 (3.9 L/kg) is lower than that in HX1 (6.3 L/kg).

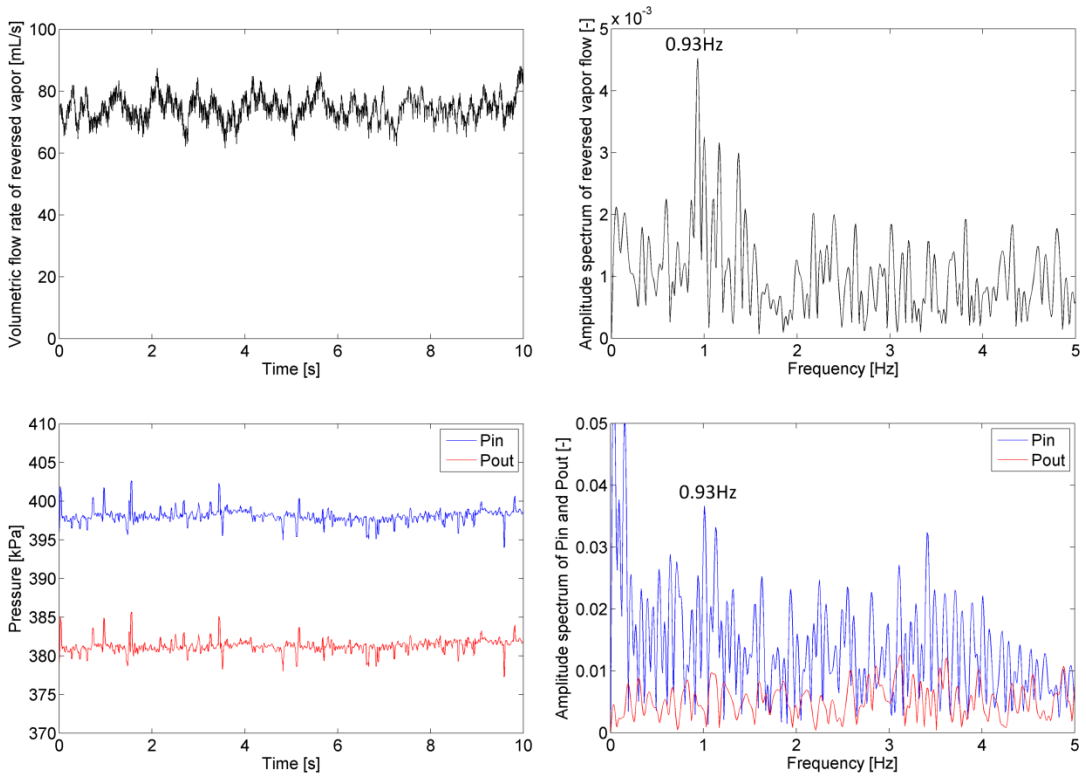


Figure 5-8 Temporal variation and frequency analysis of the reversed vapor flow rate and pressures in HX3

Bubble dynamic simulation is carried out in the same way as is described in chapter 5.3.1. Figure 5-9 shows the flow regime and pressure development within one periodic cycle for R134a in a channel with 0.5 mm diameter and 510 mm length. The highest pressure propagates to 26% of the tube length from the inlet, and it occurs at 82% of the entire period. The model is able to predict the effect of channel length on flow reversal fairly accurately, as shown in Figure 5-10. The reason for the reduction of flow reversal in the longer channel is the following: even though average heat flux is similar for both channels, the mass flow rate in the longer channel is much higher than that in the shorter channel, because longer length ensures more heat input into the channel and the cross

sectional area stays the same. In this case, the mass flow rate of supplied liquid refrigerant in HX3 is 19.1 g/s compared with 8.2 g/s in HX1. At the beginning of a cycle when a channel is relatively empty, the refrigerant side heat transfer coefficient is low due to large dryout area, which generates less acceleration of the downstream flow. During this period, because of higher incoming velocity, there is relatively more refrigerant flowing into the longer channel than the shorter one, building up higher upstream resistance. It can be seen from the comparison of the pressure contours in Figure 5-5 and Figure 5-9: there is more light-blue region in the longer channel, indicating higher upstream resistance which in turn contributes to less flow reversal. As for the frequency, the prediction is qualitatively correct as shown in Figure 5-10 demonstrating that longer channel results in lower frequency.

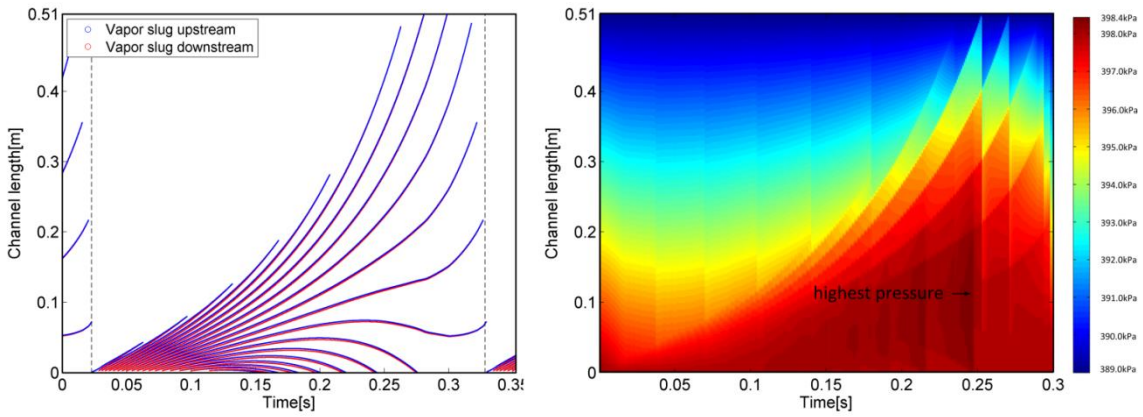


Figure 5-9 Flow regime and pressure development within one periodic cycle for R134a in a channel with 0.5 mm diameter and 510mm length

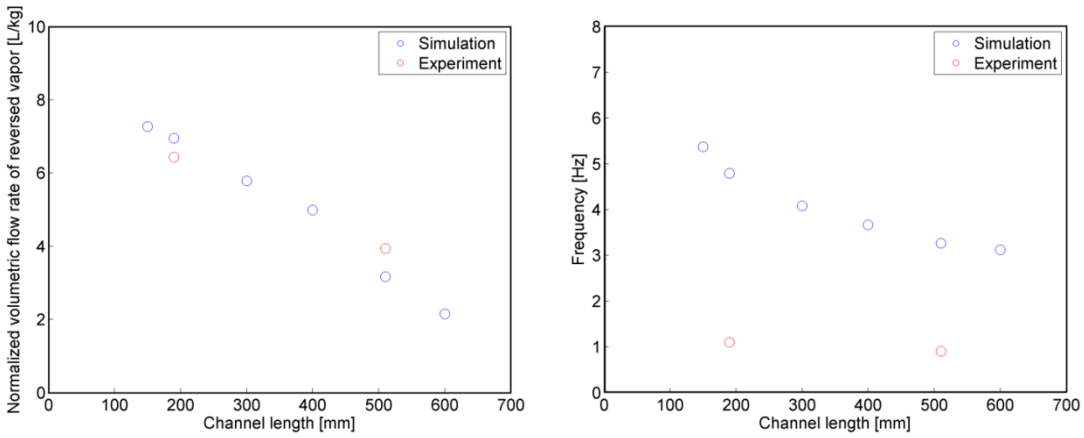


Figure 5-10 Both simulation and experiment show that normalized volumetric flow rate of reversed vapor and frequency decrease with longer channel length (under 7.5 kW/m$^2$ heat flux and 6.7 ℃ superheat)

## 5.4 SUMMARY AND CONCLUSIONS

In this chapter, the effects of channel diameter and length on flow reversal are presented. A newly developed mechanistic model which can simulate bubble dynamics in single microchannel is used to simulate and explain the experimental results.

It has been found experimentally that under the same heat flux, superheat and channel length, the microchannel evaporator with smaller diameter induces more reversed vapor flow (per unit mass flow rate of supplied refrigerant) at a higher frequency. Simulation under the same condition demonstrates that smaller diameter creates more rapid growth of vapor slugs and allocates more flow resistance to the downstream. As a result, the incoming flow is quickly decelerated and the positive pressure gradient ends up covering larger upstream areas, all of which leads to more flow reversal at a higher frequency. Experiments also show that the microchannel evaporator with longer tubes (when the

diameter is the same) produces less reversed vapor flow (per unit mass flow rate of supplied refrigerant) at a lower frequency. Consistent with the experimental results, simulation also predicts less flow reversal at a slower frequency in the longer channel. This is due to relatively more buildup of upstream resistance due to a higher refrigerant velocity in the longer channel, especially at the beginning of a periodic cycle when large dryout area exists.

# Chapter 6 EFFECT OF REFRIGERANT THERMOPHYSICAL PROPERTIES ON FLOW REVERSAL IN MICROCHANNEL EVAPORATORS

## 6.1 INTRODUCTION

Using the model presented in Chapter 4, bubble dynamics simulations are carried out for nine widely used refrigerants in the same microchannel and under the same operation conditions. Simulation results demonstrate that the amount and frequency of reverse flow largely depend on the specific volume difference and heat of vaporization of the working fluid. Four refrigerants with different thermophysical properties are selected and experimentally examined under conditions that are very close to the simulated. In reality, each refrigerant should have its own optimized channel geometry thus different heat flux, but the purpose of this study is to single out the effect of refrigerant thermophysical properties on flow reversal, so the heat flux and channel geometry are kept the same for all refrigerants. Experimental results are used to validate the numerical model.

## 6.2 SIMULATION RESULTS

All simulations are carried out in the same channel geometries (0.5 mm hydraulic diameter and 190 mm length) and under the same heat flux (7.5 $kW/m^2$) based on the refrigerant side area. The quality at the entrance of the microchannel is fixed to be 0 for

all refrigerants. Refrigerant distribution among parallel microchannels is assumed to be uniform, so single channel simulation is representative of the whole heat exchanger.

Revisiting equation 4-14, it describes the expansion rate of a vapor slug. In the literature, many authors (Brutin (2003), Tadrist (2007) and Li and Hrnjak (2017a)) believe that boiling instabilities in microchannels are determined by the competition between the vapor recoil effect (caused by rapid vapor expansion) and the inertia effect (imposed by pumps). The expansion rate of the vapor slugs serves as the driving force for flow reversal. The faster the expansion rate is, the more likely the incoming fluid will be decelerated or even reversed. This expansion rate is proportional to the difference between the specific volume of the saturated vapor and saturated liquid of the working fluid (referred to as specific volume difference in later text), and inversely proportional to the heat of vaporization. Eight widely used refrigerants with a wide range of specific volume differences and heats of vaporization (shown in Table 6-1) are investigated in the numerical study. Properties are calculated using Engineering Equation Solver. Evaporation temperature is fixed at 5 °C for all selected refrigerants.

Table 6-1 Selected thermophysical properties of the examined refrigerants

| | R1233zd(E) | R245fa | R134a | R1234yf | R410A | R32 | R717 | R290 | R744 |
|---|---|---|---|---|---|---|---|---|---|
| $T_{evap}$[°C] | 5 | 5 | 5 | 5 | 5 | 5 | 5 | 5 | 5 |
| $v_{fg}$ [L/kg] | 288.84 | 249.98 | 57.52 | 47.24 | 27.03 | 37.64 | 241.42 | 81.58 | 7.58 |
| $h_{fg}$ [kJ/kg] | 202.3 | 201.7 | 194.7 | 160.0 | 215.3 | 307.3 | 1244.0 | 367.5 | 215.0 |

The frequency of flow reversal is used to indicate its intensity. Simulated frequencies of all selected refrigerants are summarized in Figure 6-1. It shows that as the specific volume difference increases, the frequency of flow reversal also increases. Referring to

equation 4-14, under the same heat input, vapor slugs of the refrigerant with higher specific volume difference expands faster (assuming other parameters remain the same). As a result, more fluid will be reversed at a higher speed, creating a higher frequency. Additionally, lower heat of vaporization also causes a rise of the frequency of flow reversal. Equation 4-14 demonstrates that under the same heat input, vapor slugs of a refrigerant with lower heat of vaporization grow more quickly (assuming other parameters remain the same). Consequently, more reverse flow is generated faster, which contributes to a higher frequency.

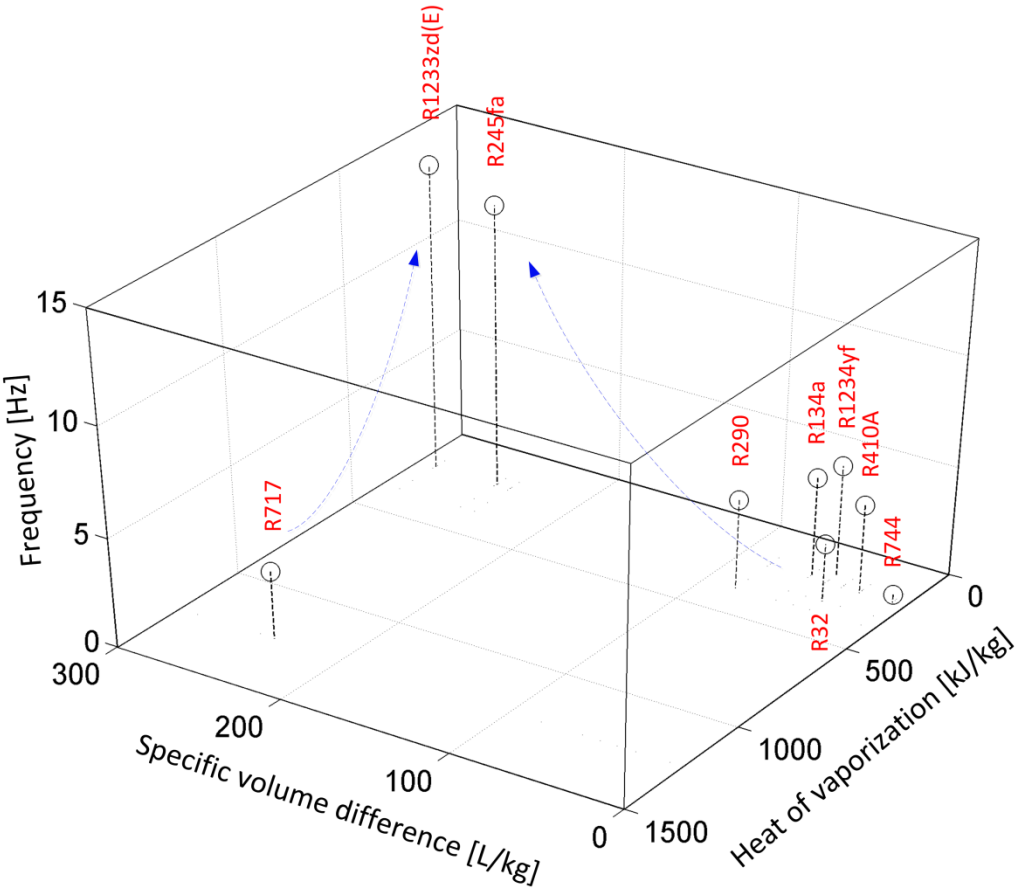


Figure 6-1 Frequency of flow reversal increases with increasing specific volume difference and decreasing heat of vaporization

In addition to the frequency, another parameter defined as the volumetric flow rate of reversed vapor normalized by the mass flow rate of the supplied liquid refrigerant ($\dot{V}_{rev,v}/\dot{m}_l$, referred as the normalized volumetric flow rate of reversed vapor in later text) is employed to quantify the intensity of flow reversal. This parameter represents the competition between the vapor expansion effect (determines the volumetric flow rate of reversed vapor) and the inertia effect (determines the mass flow rate of supplied liquid refrigerant). The reason why this parameter is selected is stated in Chapter 5.3.1. Normalized volumetric flow rates of reversed vapor of all selected refrigerants are summarized in Figure 6-2. It has been shown that as the specific volume difference increases, the normalized volumetric flow rate of reversed vapor also increases. This is caused by a more drastic expansion of vapor slugs. More interestingly, the normalized volumetric flow rate of reversed vapor seems to be not very sensitive to heat of vaporization (under fixed heat flux condition). As the heat of vaporization decreases, a vapor slug expands faster creating more reverse flow; meanwhile, the mass flow rate of supplied refrigerant also increases under a fixed heat flux. The heat of vaporization seems to have effects with similar magnitude on both flow rates, which creates the insensitivity.

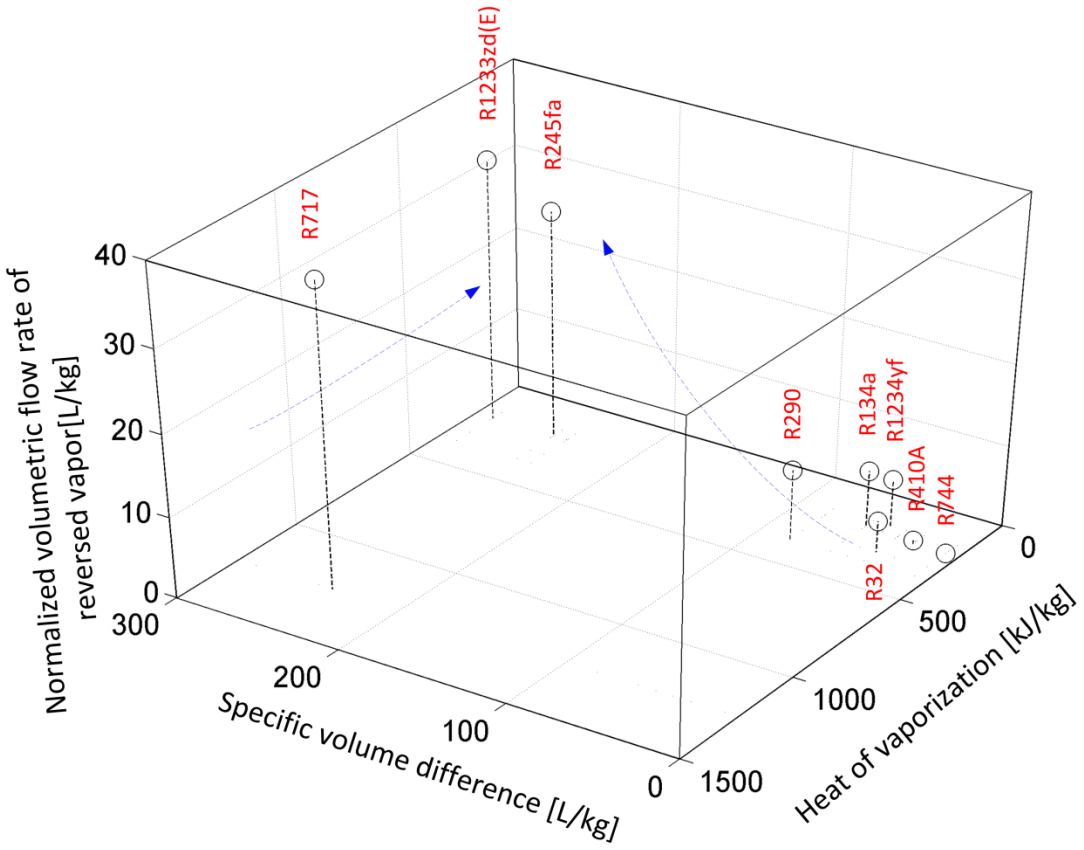


Figure 6-2 Normalized volumetric flow rate of reversed vapor increases with increasing specific volume difference and is not sensitive to heat of vaporization

## 6.3 RESULTS AND DISCUSSION

In order to demonstrate the effect of specific volume difference on flow reversal, R245 and R134a are selected, since they have very similar heat of vaporization but very different specific volume difference. Although the combination of R744 and R134a might also work, the sealing of the evaporator (the junctions between aluminum channels and transparent headers) cannot withstand the operation pressure of R744, thus this refrigerant combination is discarded. In order to demonstrate the effect of heat of vaporization on flow reversal, R134a and R1234yf are employed. By adjusting the

evaporation temperature, R1234yf can have the similar specific volume difference with R134a but smaller heat of vaporization. In addition, R134a and R32 are also tested. Again by adjusting the evaporation temperature, R32 can have a similar specific volume difference with R134a but higher heat of vaporization. The same test facilities and evaporator (only HX2) as described in Chapter 5.2 are utilized in this study.

### 6.3.1 EFFECT OF SPECIFIC VOLUME DIFFERENCE

R134a and R245fa are selected to demonstrate the effect of specific volume difference on flow reversal. The evaporation temperature of R245fa is adjusted to 22℃ so that its heat of vaporization is very similar with R134a's (shown in Table 6-2). Additionally, 22℃ evaporation temperature which corresponds to 132.1kPa evaporation pressure ensures the system to avoid subatmospheric operation. The heat flux and superheat are fixed around 7.5kW/m$^2$ and 6.5℃ for both refrigerants.

Table 6-2 The selected refrigerants have close heats of vaporization but different specific volume differences

| | R134a | R245fa |
|---|---|---|
| $T_{evap}$[℃] | 5 | 22 |
| $v_v$ [mL/g] | 58.3 | 130.5 |
| $v_l$ [mL/g] | 0.78 | 0.74 |
| $h_{fg}$ [kJ/kg] | 194.7 | 192.1 |

As shown in Figure 6-3 and Figure 6-4, under the same operation condition (heat flux and superheat), R245fa produces almost four times as much volumetric flow rate of reversed vapor as R134a. The normalized volumetric flow rate of reversed vapor of R245fa is 260% higher, which indicates more intense boiling instabilities associated with

R245fa. The signals of reversed vapor flow and pressure drop around the evaporator in the frequency domain are demonstrated on the right side of Figure 6-3 and Figure 6-4. They are obtained through Fast Fourier Transformation (FFT) of the temporal data. According to the model prediction in Chapter 6.2, R245fa should have higher dominant frequency than R134a, but the experimental results demonstrate that the dominant frequency of R245a is at 0.53Hz which is lower than R134a's (1.31Hz). The reason for this discrepancy might be related to the phenomena shown in Figure 6-5. Since R245fa generates much more reverse vapor flow by volume compared with R134a, all of the reversed vapor may not be directed out of the inlet header by the venting lines alone. Figure 6-5 demonstrates the liquid level fluctuation in the inlet headers caused by the excessive amount of reversed R245fa vapor. On the left side of Figure 6-5, the liquid level is at its highest location during an entire cycle, and the liquid refrigerant totally submerges the header inlet. On the right side of Figure 6-5, due to a large amount of reversed R245fa vapor, the liquid level has been pushed down and a certain amount of vapor exits from the header inlet to the separation tank. Inside of the separator, the reversed vapor shoots up periodically. The vapor venting process of R245fa in the experiment involves the movement of the liquid not only in the inlet header but also in the separation tank, which might be the reason for a low dominant frequency. Additionally, the real reversed vapor flow rate should be higher than the measurement, since part of it vents through the separation tank. In contrast with R245fa, the liquid level always stays high and steady in the inlet header for R134a.

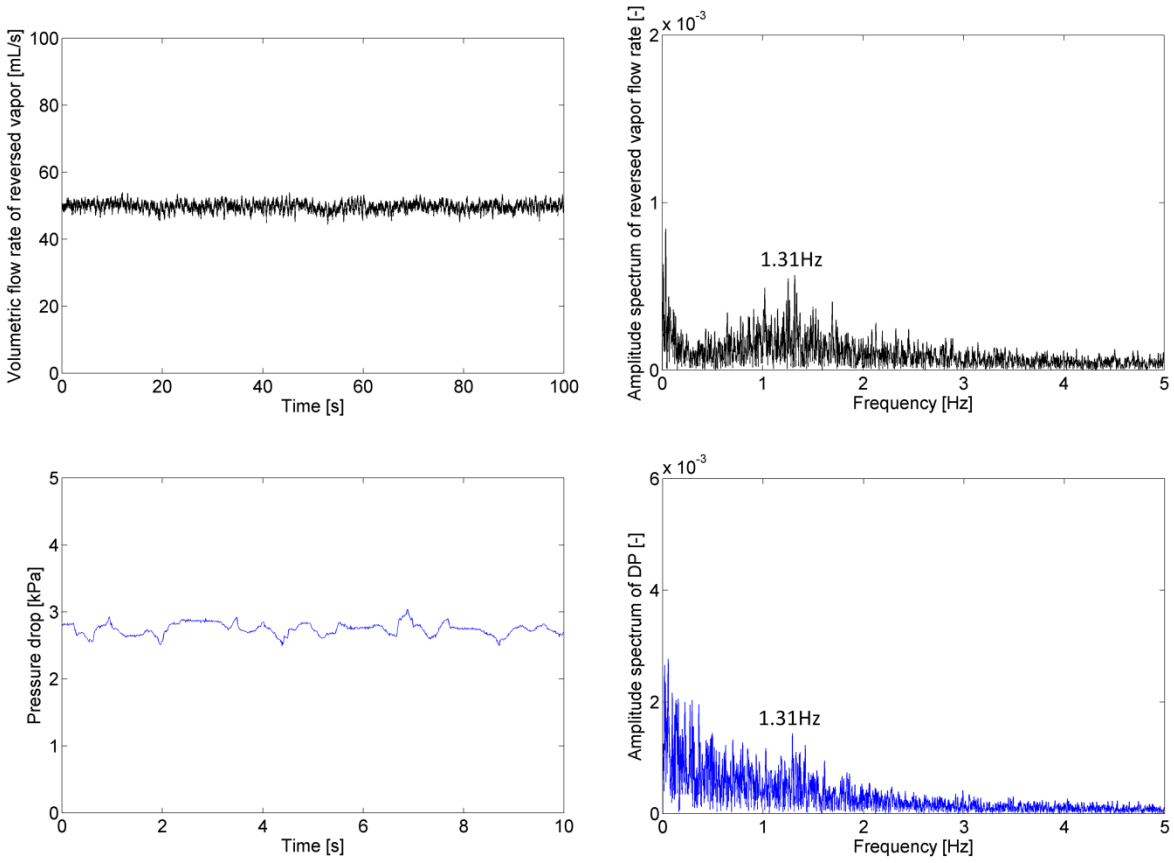


Figure 6-3 Temporal variation and frequency analysis of the reversed vapor flow rate and evaporator pressure drop in the R134a system

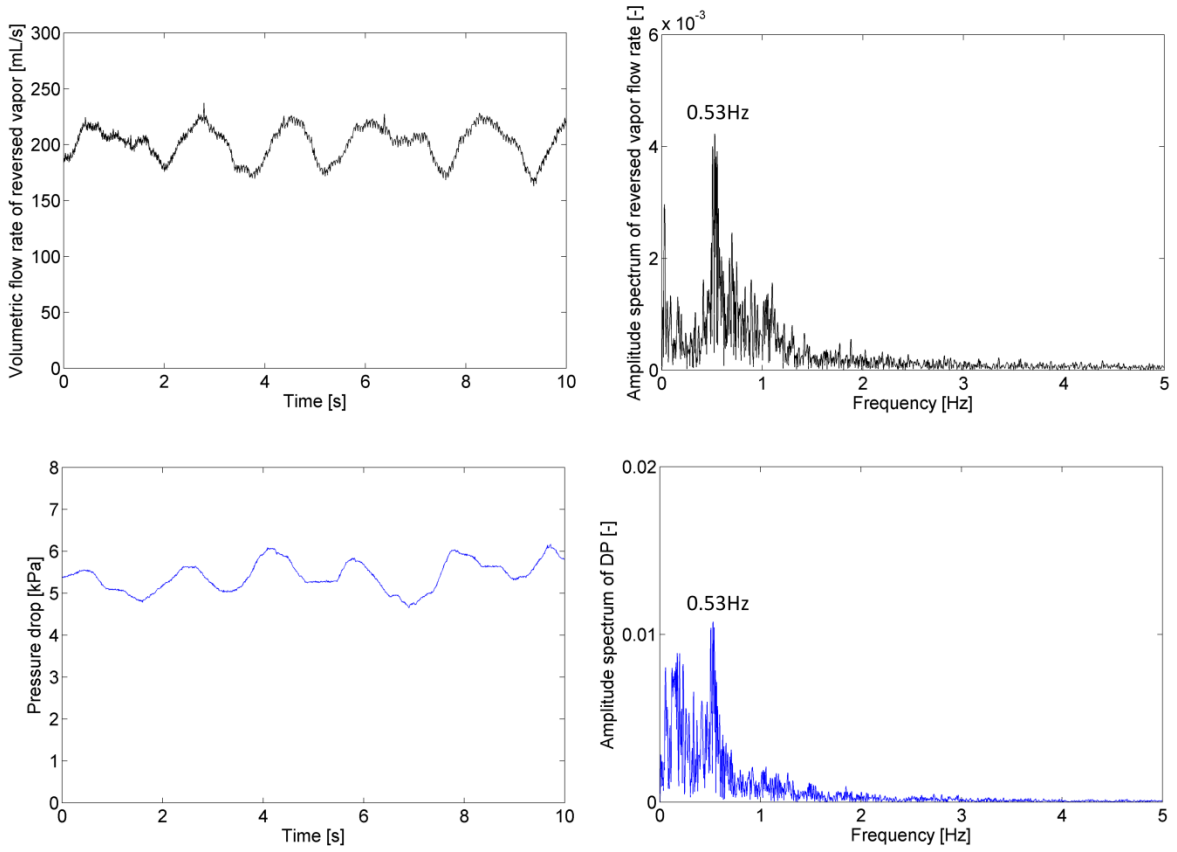


Figure 6-4 Temporal variation and frequency analysis of the reversed vapor flow rate and evaporator pressure drop in the R245fa system

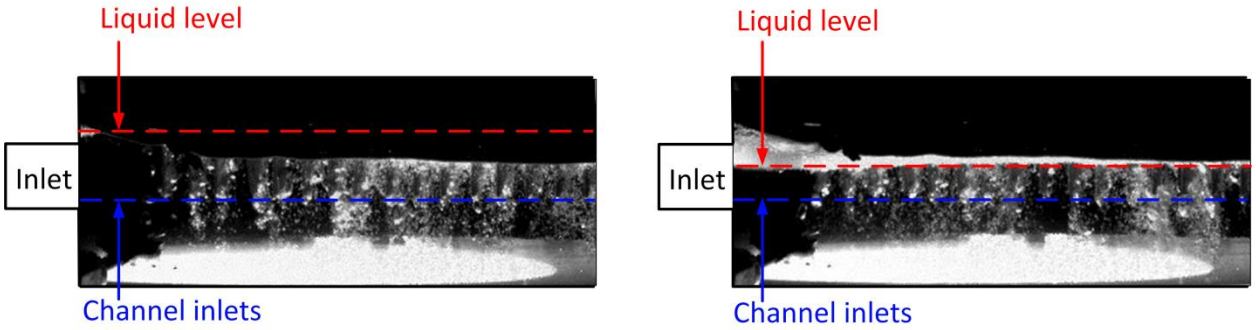


Figure 6-5 Fluctuations of the liquid level in the inlet header during flow reversal for R245fa (the highest location of the liquid level is shown on the left, and the lowest is shown on the right)

For R134a and R245fa, bubble dynamics simulation is carried out under conditions that are the same as in the corresponding experiment. In order for the model to have the same mass flux as in the experiment, pressure drops in the simulation are adjusted. Figure 6-6 shows the flow regime and pressure development within one cycle for R134a in a channel with 0.5 mm diameter and 190 mm length. On the left side of Figure 6-6, blue lines and red lines are used to track the locations of the upstream and downstream edges of each vapor slug in time. A schematic of the in-tube flow regime is employed (also shown on the left side of Figure 6-6) to illustrate the physical interpretation of the red and blue lines. Two vertical dashed lines mark the beginning and end of a cycle. The curved dashed line is the iso-zero-velocity line. The fluid in the region ((in both time (x-axis) and space (y-axis))) which is above this line has positive velocity, thus flows forward; the fluid in the region which is underneath this line has negative velocity and most of it (vapor and liquid) will be vented out from the channel inlet. The area of the region largely determines the normalized volumetric flow rate of the reversed vapor, because it indicates how much fluid will be vented out.

The in-tube pressure development within one cycle is shown on the right side of Figure 6-6, and it corresponds to the flow regimes between the vertical dashed lines on the left. The highest and lowest pressures during the entire cycle are selected as the upper and lower limits of the color bar to maximize the resolution. It can be seen that as the rapid bubble growth continues to accelerate the downstream flow, and decelerate the upstream flow, the highest pressure inside of the channel migrates from the inlet towards the downstream section of the channel. In this case, the highest pressure occurs at 74% of the entire period and at 34% of the tube length from the inlet. The pressure elevation

ratio (R) defined in equation 6-1 is used to quantify how strong the positive pressure gradient is. Stronger positive pressure gradient will vent the reverse flow more quickly, which leads to higher frequency. In the case of R134a, the pressure elevation ratio is 23%.

$$R = \frac{P_{\max} - P_{in}}{P_{in} - P_{out}} \tag{6-1}$$

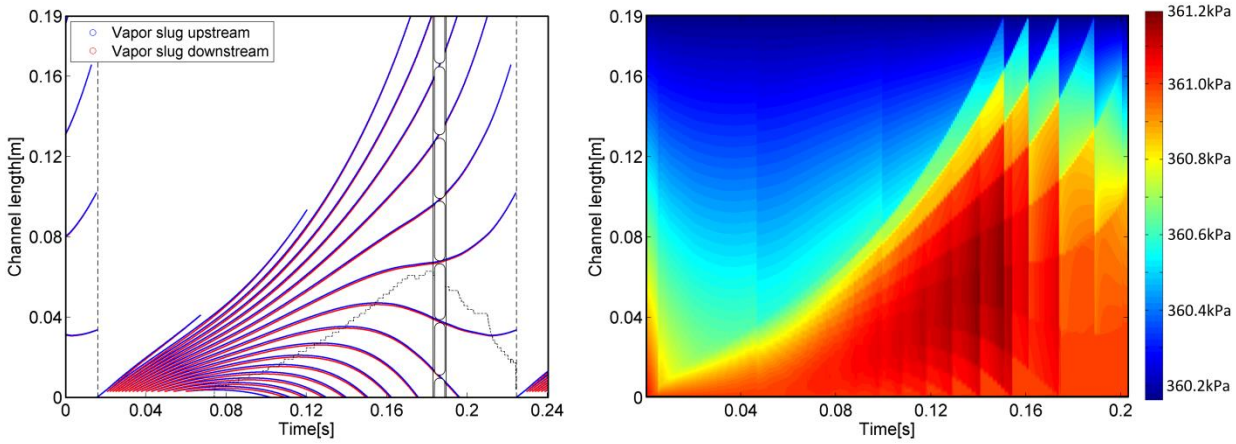


Figure 6-6 Flow regime and pressure development within one periodic cycle for R134a

Figure 6-7 shows the same content as in Figure 6-6, but it is for R245fa in the same channel. According to the analysis in Chapter 6.2, R245fa which has much higher specific volume difference than R134a should have faster bubble expansion, causing higher acceleration of the downstream fluid and deceleration of the upstream fluid. In that sense, R245fa should have more intense flow reversal. It can be seen from the comparison of flow regimes in Figure 6-6 and Figure 6-7 that flow reversal is much more likely to happen for R245fa. Figure 6-7 (right) shows that the highest pressure propagates to 34% of the tube length from the inlet, and it occurs at 72% of the entire period. Although the relative temporal and spatial locations of the highest pressure are similar for R134a and R245fa, R245fa overall has larger positive pressure region which is reflected

by a larger region with negative velocities (compare the regions underneath the iso-zero-velocity lines in Figure 6-6 (left) and Figure 6-7 (left)). As a result, the normalized volumetric flow rate of reversed vapor of R245fa (19.6 L/kg) is higher than that of R134a (7.2 L/kg). The pressure elevation ratio is 98% for R245fa, which causes a much higher frequency (9.0Hz) compared with R134a's (4.8Hz).

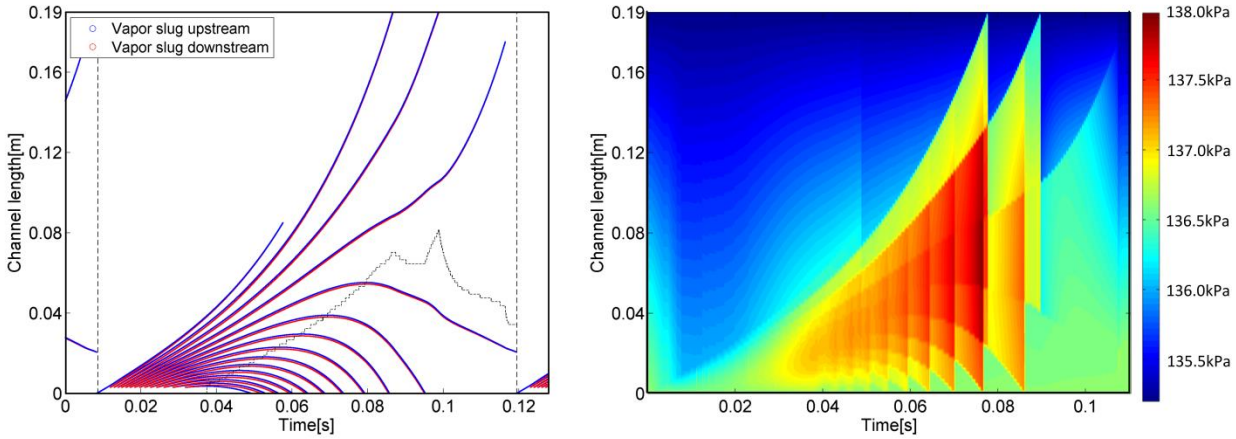


Figure 6-7 Flow regime and pressure development within one periodic cycle for R245fa

Table 6-3 summarizes the comparison between experimental and simulated results of normalized volumetric flow rate of reversed vapor and frequency. The model is able to capture the normalized volumetric flow rate fairly accurately. More importantly, this model is capable of predicting that R245fa produces higher normalized volumetric flow rate of reversed vapor than R134a. As for the frequency, the simulation results do not agree with the experimental results, the reason of which is stated earlier in this chapter. Even for R134a, the predicted frequency is much higher than the measured. One possible reason for the discrepancy is the following: the measured frequencies are a result of the compressible volume in the inlet header interacting with the reverse flow from hundreds of microchannels; while the simulated frequency only accounts for the instabilities

caused by rapid bubble expansion in a single microchannel. The compressible volume in the inlet header reduces the frequency, making the measured results much lower than the simulated single channel frequency.

Table 6-3 Comparison between experimental and simulative results: R134a and R245fa

| | Normalized volumetric flow rate of reversed vapor [L/kg] | | Frequency (Hz) | |
|---|---|---|---|---|
| | Experiment | Simulation | Experiment | Simulation |
| R134a | 6.29 | 6.95 | 1.31 | 4.8 |
| R245fa | 22.70 | 19.63 | 0.53 | 9.0 |

### 6.3.2 EFFECT OF HEAT OF VAPORIZATION

R134a, R1234yf and R32 are selected to demonstrate the effect of heat of vaporization on flow reversal. The evaporation temperature of R1234yf is adjusted to 0 ℃ so that its specific volume difference is similar with R134a's (shown in Table 6-4), while its heat of vaporization is 16% lower. The evaporation temperature of R32 is adjusted to -5 ℃ so that its specific volume difference is close with R134a's (shown in Table 6-4), but its heat of vaporization is 66% higher. The heat flux and superheat are fixed around 7.5 $kW/m^2$ and 6.7 ℃ for all tests.

Table 6-4 The selected refrigerants have close specific volume difference but different heat of vaporization

| | R134a | R1234yf | R32 |
|---|---|---|---|
| $T_{evap}$[°C] | 5 | 0 | -5 |
| $v_v$ [mL/g] | 58.3 | 56.5 | 53.3 |
| $v_l$ [mL/g] | 0.78 | 0.85 | 0.93 |
| $h_{fg}$ [kJ/kg] | 194.7 | 163.3 | 322.9 |

Comparison between Figure 6-3 and Figure 6-8 shows that on average, the volumetric flow rate of reversed vapor of R1234yf (66.1 mL/s) is 28% higher than that of R134a (51.6 mL/s). Due to smaller heat of vaporization, under similar heat fluxes, the supplied liquid flow rate of R1234yf (9.9 g/s) to the heat exchanger is 21% higher than that of the R134a (8.2 g/s); in the end, the normalized volumetric flow rate of reversed vapor of R1234yf is only 6.5% higher than that of R134a's. Given that the measurement uncertainties of the normalized volumetric flow rates for R134a and R1234yf are ±3.6% and ±2% respectively, the difference is not significant. As for the dominant frequency for R1234yf, both reversed vapor flow rate and pressure drop have a dominant frequency below 0.1Hz and a dominant frequency at 1.53Hz. According to Tuo and Hrnjak (2013a), the lower frequency is not rare in air conditioning systems and might be caused by the superheat control using an electronic expansion valve. The real dominant frequency associated with flow reversal is 1.53 Hz, which is higher than that of the R134a (1.31 Hz).

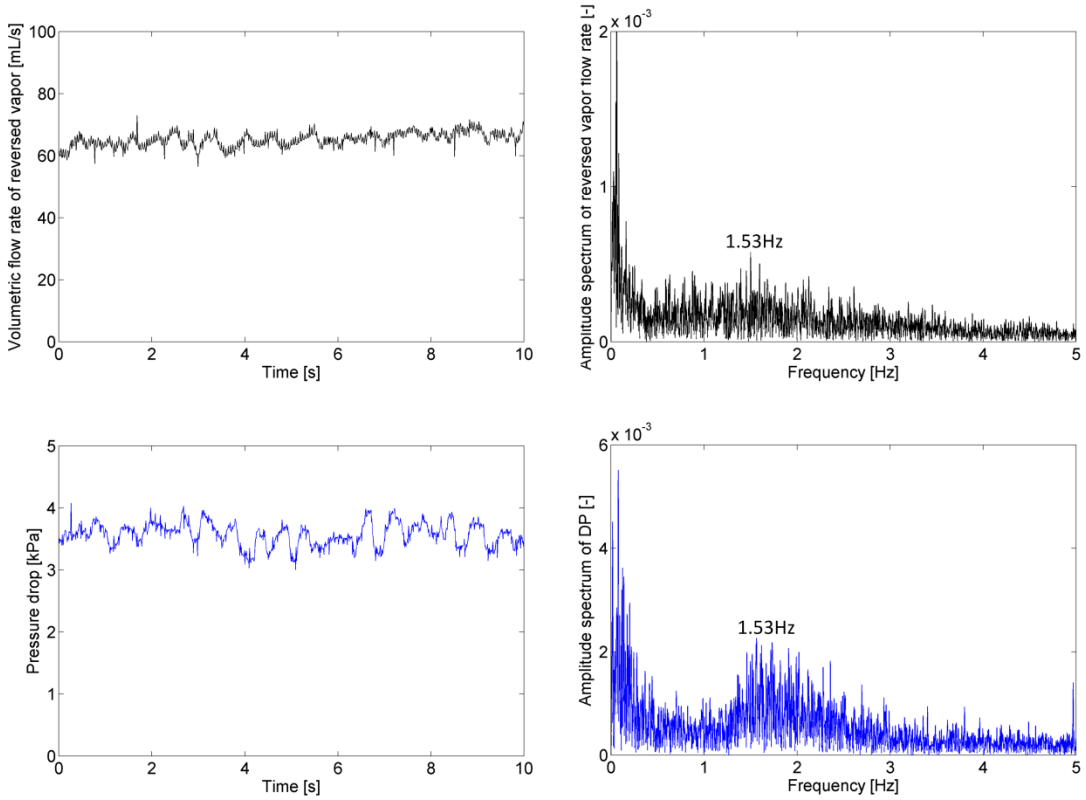


Figure 6-8 Temporal variation and frequency analysis of the reversed vapor flow rate and evaporator pressure drop in the R1234yf system

Comparison between Figure 6-3 and Figure 6-9 shows the difference between R134a and R32 in terms of flow reversal. On average, the reversed vapor flow rate of R32 (38.5 mL/s) is 25% lower than that in R134a (51.6 mL/s) system. Due to smaller heat of vaporization, under similar heat fluxes, the supplied liquid flow rate of R32 to the heat exchanger drops 33% compared with the R134a system; As a result, the normalized volumetric flow rate of reversed vapor of R32 is 12% higher than R134a's. Considering the measurement uncertainties of the vapor reversal ratios for R134a and R32 are ±3.6% and ±9.7% respectively, the difference between these two ratios is rather small. As for the

frequencies, the dominant frequency of the R32 system is lower than that of the R134a system, which is an indication of less boiling instabilities.

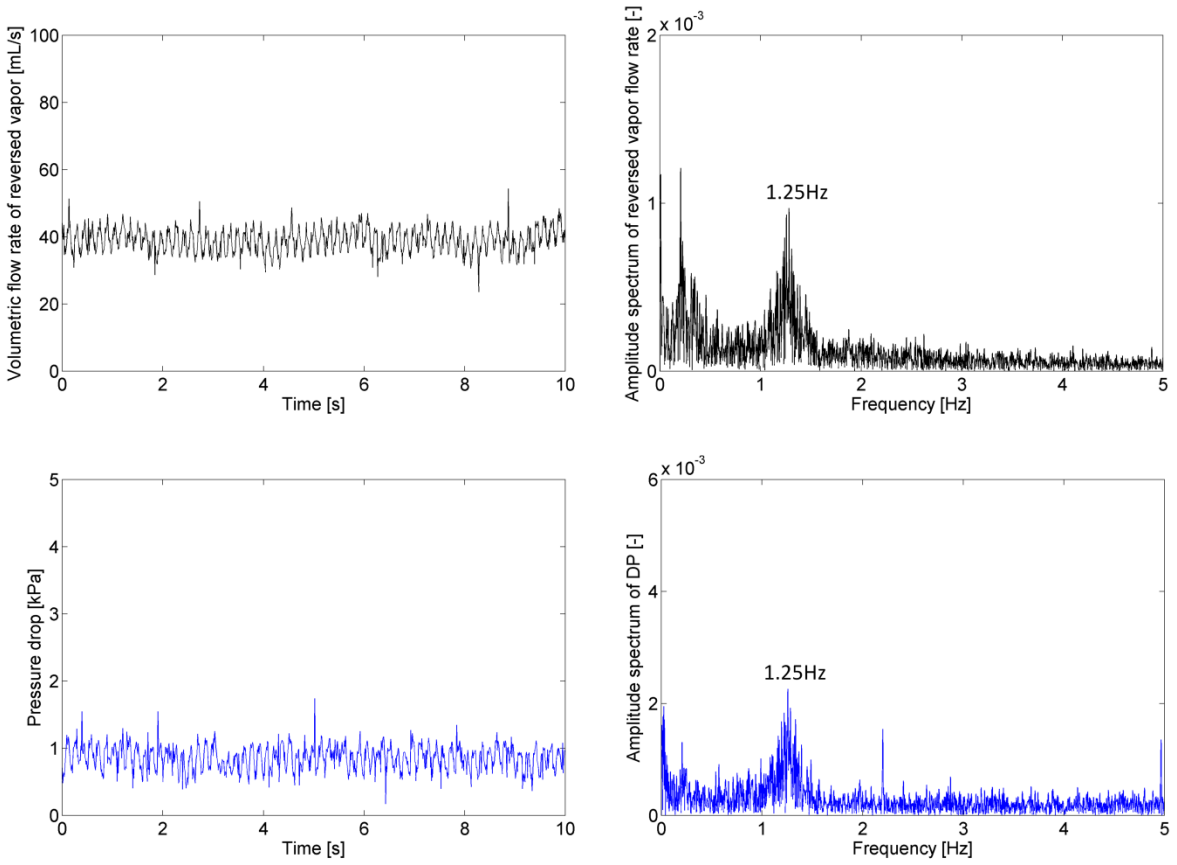


Figure 6-9 Temporal variation and frequency analysis of the reversed vapor flow rate and evaporator pressure drop in the R32 system

Bubble dynamic simulations are carried out in the same way as is described in Chapter 6.3.1 for R1234yf and R32, respectively. The flow regime and pressure development for R1234yf are show in Figure 6-10. For R1234yf, the highest pressure propagates to 34% of the tube length from the inlet, and it occurs at 68% of the entire period, both of which are very close with R134a's. More importantly, the negative velocity regions for both refrigerants remain almost identical (compare the regions

underneath the iso-zero-velocity lines in Figure 6-6 (left) and Figure 6-10 (left)). Thus the simulated normalized volumetric flow rate of reversed vapor are very close (7.3 L/kg for R1234yf and 7.2 L/kg for R134a). In the simulation, although the volumetric flow rate of reversed vapor of R1234yf is 21% higher than that of R134a, the supplied liquid flow rate is also 19% higher due to lower heat of vaporization. It turns out that the magnitudes of the heat of vaporization effect on reverse vapor flow rate and supplied liquid flow rate are quite similar. As for the frequency, the pressure elevation ratio is 34% for R1234yf, which is higher than that of R134a. Thus the simulated frequency of R1234yf (5.6 Hz) is higher than that of the R134a (4.8 Hz).

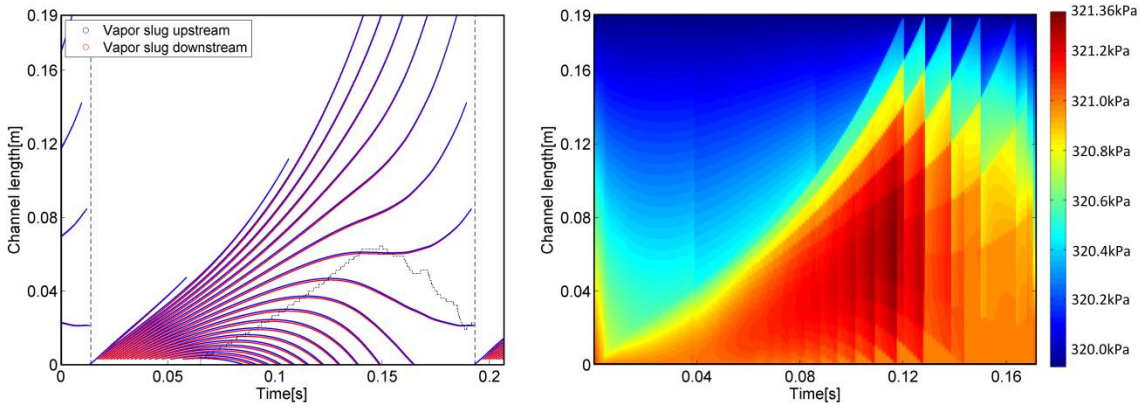


Figure 6-10 Flow regime and pressure development within one cycle for R1234yf

The flow regime and pressure development for R32 is demonstrated in Figure 6-11. For R32, the highest pressure propagates to 37% of the tube length from the inlet, and it occurs at 74% of the entire period, both of which are similar with R134a's. Again, the negative velocity region remains almost identical with R134a (compare the regions underneath the curved dash lines in Figure 6-6 (left) and Figure 6-11 (left)). As a result, the simulated normalized volumetric flow rate of reversed vapor of R32 (6.6 L/kg) is close with R134a's (7.2 L/kg). In the simulation, although the volumetric flow rate of

reversed vapor of R32 is 41% lower than that of R134a, the supplied liquid flow rate is also 36% lower due to larger heat of vaporization. This result further confirms that the heat of vaporization has similar effect on reverse vapor flow rate and supplied liquid flow rate. As for the frequency, the pressure elevation ratio is only 15% for R32, which results in a lower simulated frequency (3.1 Hz) when compared with R134a (4.8 Hz).

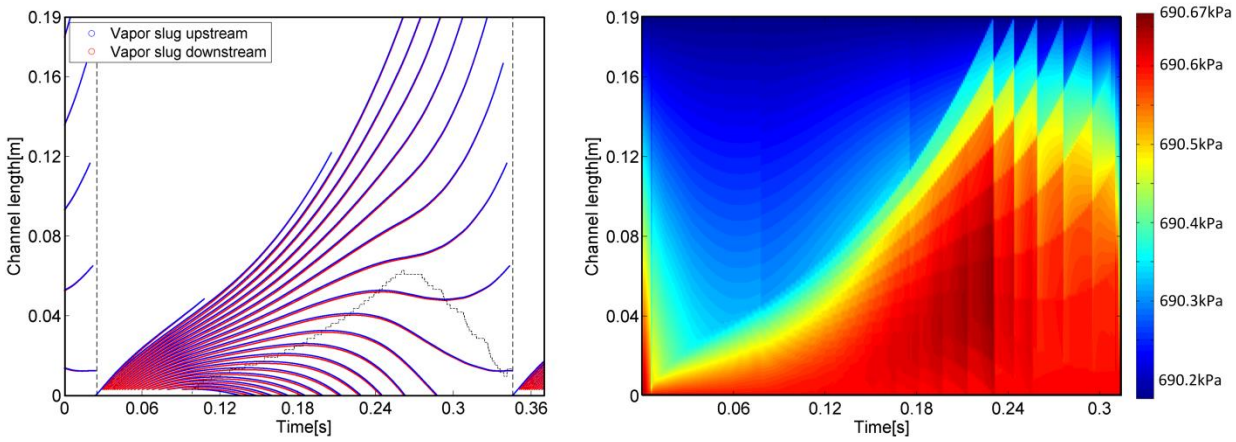


Figure 6-11 Flow regime and pressure development within one periodic cycle for R32

As is shown in Table 6-5, both the experimental and simulated normalized volumetric flow rate of reversed vapor are not sensitive to heat of vaporization, given that the heat of vaporization doubles from R1234yf to R32. As for the frequencies, the simulative results are qualitatively correct predicting that the frequency decreases as heat of vaporization increases. The quantitative discrepancies between experimental and simulative results are discussed in the counterpart in Chapter 6.3.1.

Table 6-5 Comparison between experimental and simulated results: R134a and R1234yf

| | Normalized volumetric flow rate of reversed vapor [L/kg] | | Frequency (Hz) | |
|---|---|---|---|---|
| | Experiment | Simulation | Experiment | Simulation |
| R1234yf | 6.71 | 7.35 | 1.53 | 5.58 |
| R134a | 6.29 | 6.95 | 1.31 | 4.79 |
| R32 | 7.03 | 6.61 | 1.25 | 3.11 |

## 6.4 SUMMARY AND CONCLUSIONS

The effects of refrigerant specific volume difference and heat of vaporization on flow reversal are examined experimentally and numerically.

Experiments with R134a and R245fa show that under the same heat flux, superheat and channel geometry, the refrigerant with higher specific volume difference induces more flow reversal. The corresponding simulation shows agreement with the experiment and demonstrates that higher specific volume difference creates faster growth of vapor slugs and allocates more flow resistance to the downstream section. As a result, more incoming flow is reversed. Simulation also indicates that higher specific volume difference creates higher frequency of flow reversal, but it has not been confirmed by the experiments yet. Experiments using R134a, R1234yf and R32 show that increasing heat of vaporization reduces the volumetric flow rate of the reversed vapor, but when normalizing this volumetric flow rate by the mass flow rate of supplied refrigerant, it becomes insensitive to heat of vaporization. Frequency of flow reversal increases as the heat of vaporization of the refrigerant decreases. Simulation predictions are consistent with the experimental results. It is shown that the effects of heat of vaporization on the

volumetric flow rate of reversed vapor and mass flow rate of the supplied liquid have similar magnitude, but smaller heat of vaporization creates faster vapor slug expansion which increases the frequency.

# Chapter 7 EFFECT OF PERIODIC REVERSE FLOW ON THE HEAT TRANSFER PERFORMANCE OF MICROCHANNEL EVAPORATORS

## 7.1 INTRODUCTION

Few of the selected articles reviewed in Chapter 2 studied the effect of boiling instabilities and flow reversal on the heat transfer performance of a heat exchanger, which largely remains unknown in the literature. In this chapter, two heat exchangers with identical heat transfer areas are used. Additional upstream flow resistance is added to one of them, so that these two heat exchangers generate different amounts of reverse flow. The heat exchanger with artificial upstream flow resistance is subject to less boiling instability, but has lower capacity than the other heat exchanger. At the same time, the mechanistic model introduced in Chapter 4 demonstrates numerically that boiling instabilities and flow reversal can help to improve the refrigerant side heat transfer coefficient.

## 7.2 EXPERIMENT SETUP

In this study, two selected heat exchangers are tested under FGB and FGBR modes. Both heat exchangers as shown in

Figure 7-1 are originally parts of a bigger microchannel condenser (a bigger condenser has been cut into two smaller pieces to make these two evaporators), so these

two heat exchangers have identical refrigerant side and louver fin geometries. Major geometrical features of the two heat exchangers are shown in Table 7-1. The long heat exchanger is 320 mm longer than the short heat exchanger, and that part of the long heat exchanger is covered by wax. The wax was melted and completely submerged the fins before it solidified, so that the convective heat transfer caused by the air flow is believed to be eliminated in the waxed region. The almost adiabatic wax region in the long heat exchanger will only serve as a hydraulic restriction. Two blue dashed lines indicate the "effective inlets" for both heat exchangers. Only the areas above the "effective inlets" are used for heat transfer and both heat exchangers have the same effective heat transfer areas. The two heat exchangers are operated at similar conditions under FGBR and FGB modes. Capacities are measured for both heat exchangers. The reversed vapor flow rates are only measured in FGBR mode. The vapor reversal ratio defined as reversed vapor flow rate divided by supplied liquid flow rate to the heat exchanger ( $\dot{m}_{rev,v} / \dot{m}_l$ , as shown in

Figure 7-1) is used to quantify the intensity of the reverse flow induced by boiling instabilities.

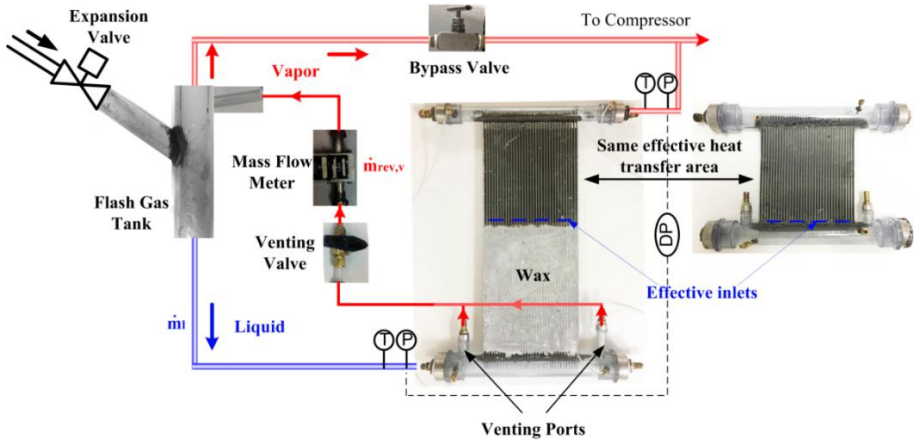

Figure 7-1 Evaporator setup in FGBR mode (evaporator presented in operation position has inlet restriction, and the one on the side has no inlet restriction)

Table 7-1 Major geometrical features of two selected heat exchangers

| Items | Unit | Heat exchanger without inlet restriction | Heat exchanger with inlet restriction |
|---|---|---|---|
| Channel diameter | mm | 0.51 | 0.51 |
| No. of channels/tube | - | 21 | 21 |
| No. of tubes/heat exchanger | - | 35 | 35 |
| Width | mm | 247 | 247 |
| Depth | mm | 16 | 16 |
| Height | mm | 190 | 510 |

## 7.3 EXPERIMENTAL RESULTS

### 7.3.1 RESULTS UNDER FGBR MODE

First, the systems are set up in the FGBR mode and operated under conditions shown in Table 7-2. Compressor speed and air side conditions (both evaporator and condenser sides) are kept constant for the systems with the two different heat exchangers.

Table 7-2 Operation conditions for both heat exchangers

| Items | Unit | Heat exchanger without inlet restriction | Heat exchanger with inlet restriction |
|---|---|---|---|
| Evaporator air inlet temperature | ℃ | 35 | 35 |
| Evaporator air flow rate | $m^3/s$ | 0.21 | 0.21 |
| Condenser air inlet temperature | ℃ | 35 | 35 |
| Condenser air flow rate | $m^3/s$ | 0.40 | 0.40 |
| Target system subcooling | ℃ | 7 | 7 |
| Target evaporator superheat | ℃ | 4/8/12 | 4/8/12 |
| Compressor speed | rpm | 900 | 900 |

As is introduced in Chapter 4, the higher the flow resistance located in the downstream part of a channel, the more reverse flow there will be. Higher superheat at the evaporator outlet creates a larger annular and dry-out region. In these regions, fluid has higher velocities and allocates more flow resistance to the downstream, thus more reverse flow are generated. Since the amount of reverse flow is a function of superheat, three superheats (4, 8 and 12 ℃) are selected in the test.

Figure 7-2 shows the infrared (IR) images and the corresponding flow regimes in the inlet headers of both heat exchangers under identical condition (listed in Table 7-2 with 12℃ superheat). Comparison of the IR images indicates that refrigerant distributions in both heat exchangers are quite uniform. Using the distribution rating parameter (Φ) proposed by Bowers et al. (2010), the Φ value for the heat exchangers without and with inlet restriction is 0.97 and 0.96, respectively, with Φ =1 being perfectly uniform. Although distributions in both heat exchangers are very uniform, flow regimes in the inlet headers are very different. It can be seen from Figure 7-2 that there are large quantities of flow reversal in the heat exchanger without inlet restriction, which is indicated by the bubbles underneath the liquid level; while in the heat exchanger with inlet restriction, flow reversal seems to be greatly suppressed with only a small amount of bubbles in the inlet header. As shown in Figure 7-3, measurement of reversed vapor flow for both heat exchangers under various superheats confirms the observation from Figure 7-2: the heat exchanger without inlet restriction generates more flow reversal than the one with inlet restriction. The vapor reversal ratio (reverse vapor flow rate divided by the supplied liquid flow rate) is plotted instead of the absolute mass flow rate of the reversed vapor in Figure 7-3.

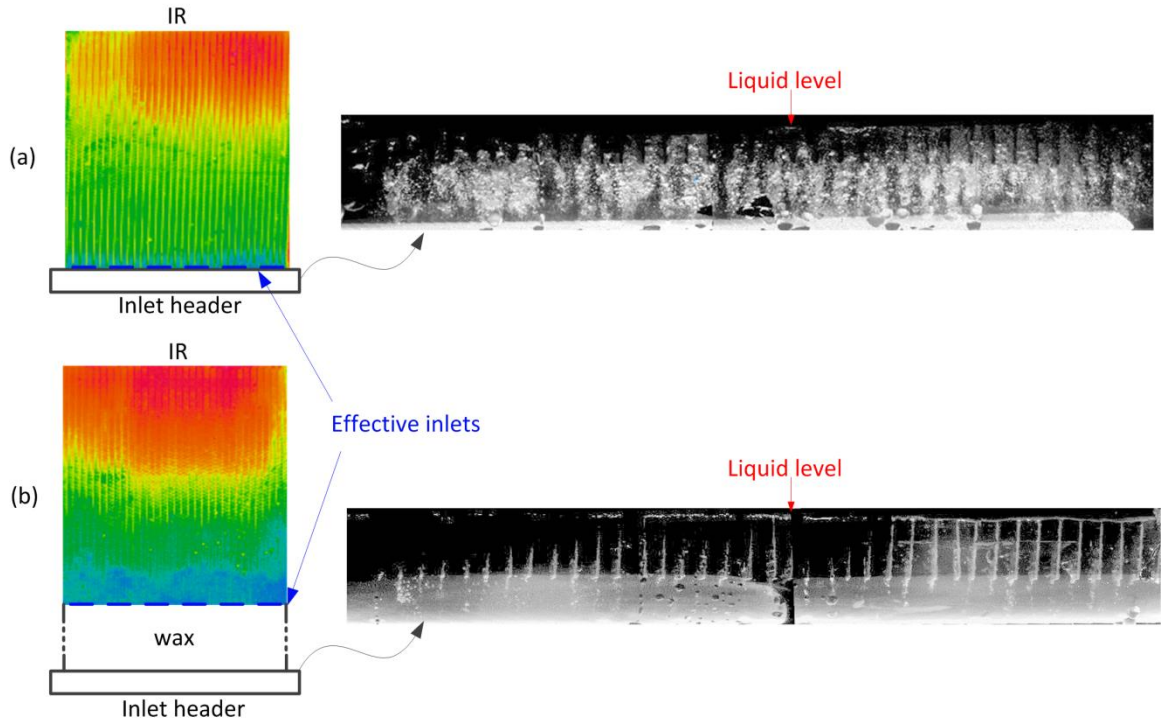


Figure 7-2 Infrared images of both heat exchangers and the corresponding flow regimes in the inlet headers under FGBR mode (a) heat exchanger without inlet restriction (b) heat exchanger with inlet restriction

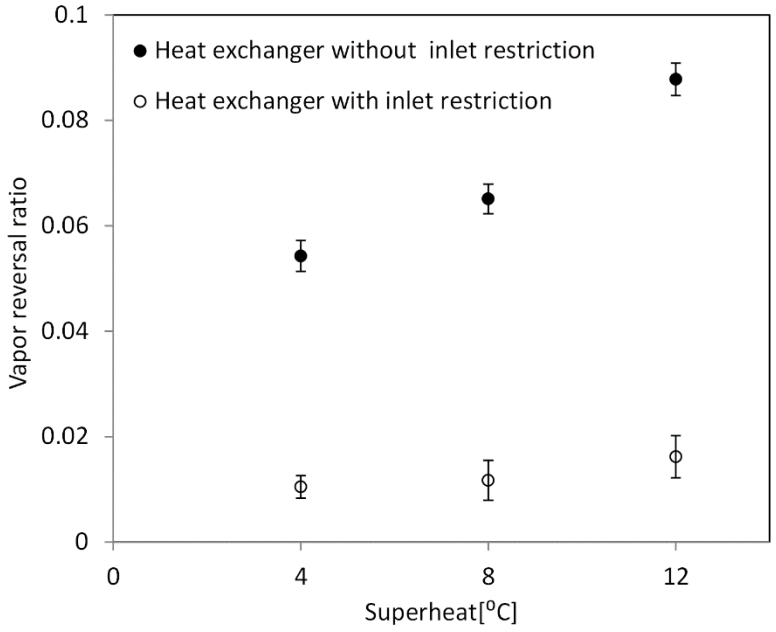


Figure 7-3 Heat exchanger without inlet restriction generates more reversed vapor flow

The capacities of both heat exchangers under three different superheats are summarized in Figure 7-4. As superheat increases, the capacities of both heat exchangers decrease, which is a result of less utilized heat transfer area. Since the operation conditions and effective heat transfer areas for both heat exchangers are the same, the difference of heat transfer performance is attributed to different magnitudes of boiling instability in both heat exchangers. Under each given superheat, the capacity of the heat exchanger without inlet restriction is higher than that of the other heat exchanger, which leads to the conclusion that boiling instability and flow reversal might enhance heat transfer. When the lowest superheat (4 ℃) is imposed, the difference between both capacities is only 4.1%, which is arguably within the measurement uncertainty range. As superheat increases, the amount of flow reversal increases faster in the heat exchanger without inlet restriction (5.4% to 8.8%) than in the one with inlet restriction (1.1% to 1.6%). As is shown in Figure 7-4, with increasing superheat, the capacity degradation rate of the heat exchanger without inlet restriction is smaller than that of the other heat exchanger. Given that the heat exchanger geometries, heat transfer areas and refrigerant distributions are identical for both heat exchangers, it is expected that the increasing boiling instabilities and flow reversal in the heat exchanger without inlet restriction compensate for the capacity decrease caused by rising superheats. In contrast, the amount of flow reversal in the heat exchanger with inlet restriction is quite insignificant to start with (1.1%) and rises slowly (up to 1.6%) with increasing superheat heat; as a result, the capacity decreases more significantly with increasing superheat when compared with the other heat exchanger.

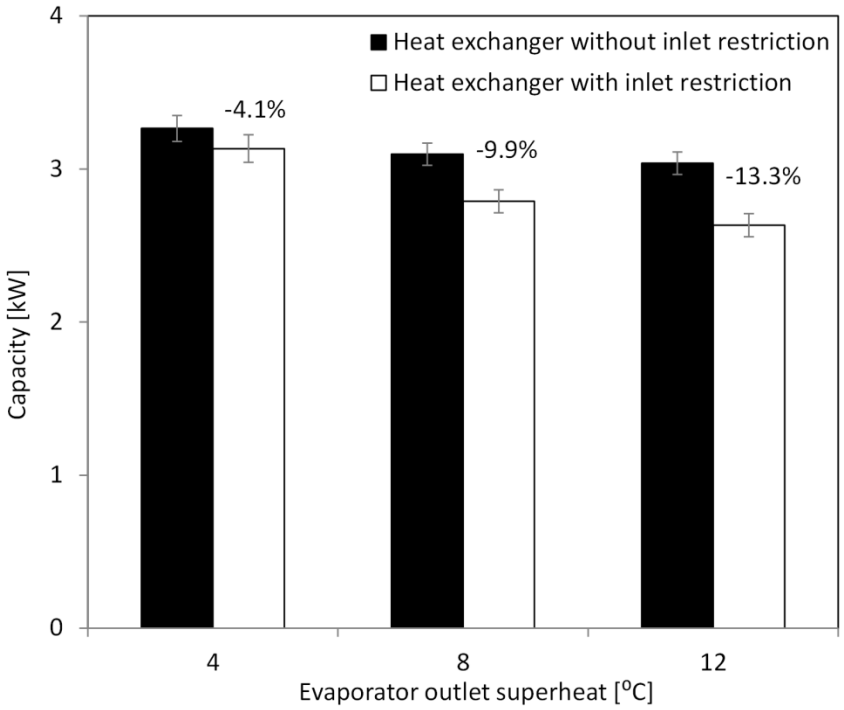


Figure 7-4 Capacity comparison under FGBR mode of both heat exchangers indicates that periodic flow reversal enhances cooling capacity

Similar trends can be observed in the comparison of the UA of both heat exchangers. The UA value of each heat exchanger can be calculated as capacity divided by the logarithmic mean temperature difference (LMTD), and the results are summarized in Figure 7-5. The UA of the heat exchanger with inlet restriction is always smaller than that of the other exchanger. As superheat increases, the UA degradation of the heat exchanger with inlet restriction is much faster than that of the heat exchanger without inlet restriction. In the case of 12 ℃ superheat, since the overall heat transfer coefficient is significantly enhanced (24.7%) by boiling instability and flow reversal, the evaporation temperature of the heat exchanger without inlet restriction is 3 ℃ higher than that of the other heat exchanger (shown in Figure 7-6).

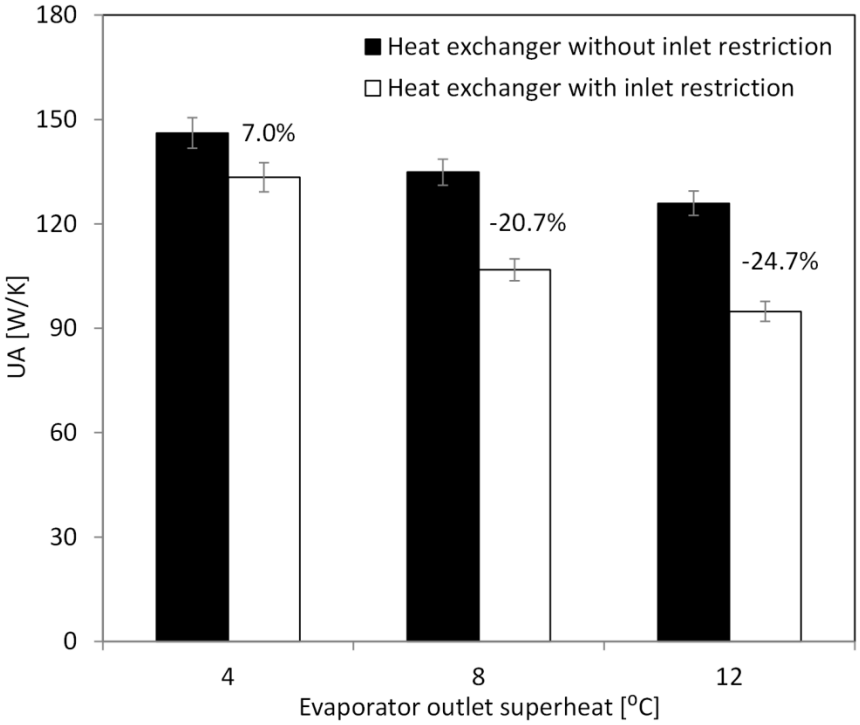


Figure 7-5 UA comparison under FGBR mode of both heat exchangers indicates that periodic flow reversal enhances refrigerant side heat transfer coefficient

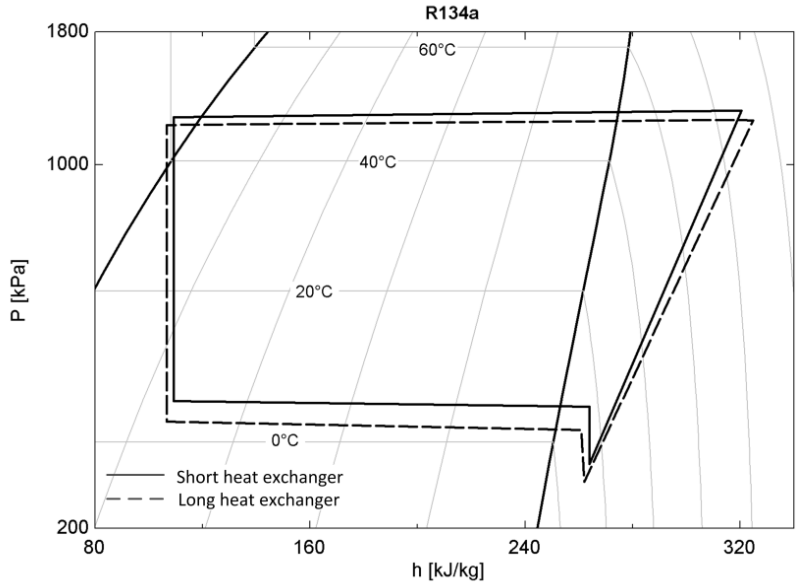


Figure 7-6 Heat exchanger without inlet restriction has higher evaporation temperature than the other heat exchanger due to higher overall heat transfer coefficient

One potential problem in this comparison is following: in the heat exchanger with inlet restriction, before the reversed vapor exits from the channel inlet, refrigerant has to flow through the waxed region. It is possible that some amount of the reversed vapor flows forward again before it even reaches the inlet. In that case, the refrigerant qualities at the "effective inlets" as marked by the blue dashed lines in

Figure 7-1 are not the same for both heat exchangers. The heat exchanger without inlet restriction ideally only receives liquid refrigerant, while the heat exchanger with inlet restriction receives a certain amount of vapor which has not exited from the real channel inlets. According to Tuo and Hrnjak (2013b), the re-entrained vapor may form "dryout" slugs and reduce local heat transfer coefficient, which might contribute to the result that the UA of the heat exchanger without inlet restriction is much higher than that of the other heat exchanger. The comparison of both heat exchangers in FGBR mode is

based on the assumption that for the heat exchanger with inlet restriction, the quality at the “effective inlets” does not substantially deviate from zero. In order to strengthen the argument that boiling instability and flow reversal help to increase heat transfer coefficient, both heat exchangers are operated under FGB mode, the results of which are shown in Chapter 7.3.2. In FGB mode, all reversed vapor in both heat exchanger has to go through the “effective inlets” again, which makes the comparison more fair.

### 7.3.2 RESULTS UNDER FGB MODE

Figure 7-7 shows the IR images and the corresponding flow regimes in the inlet header of both heat exchangers in FGB mode under identical condition (listed in Table 7-2 with 4 ℃ superheat). Comparison of the IR images indicates that refrigerant distributions in both heat exchangers are nearly uniform. The value of distribution rating parameter (Φ) for the heat exchangers without and with inlet restriction is 0.98 and 0.96, respectively. The flow regimes in the inlets headers are very different: in the heat exchanger without inlet restriction, due to a substantial amount of reversed vapor trapped in the inlet header, the liquid level fluctuates up and down, but the time-average distribution of refrigerant is kept uniform; in the heat exchanger with inlet restriction, a very small amount of flow reversal is observed in the inlet header (small bubbles under the liquid level as shown in Figure 7-7), and the liquid level is quite steady with tiny fluctuations.

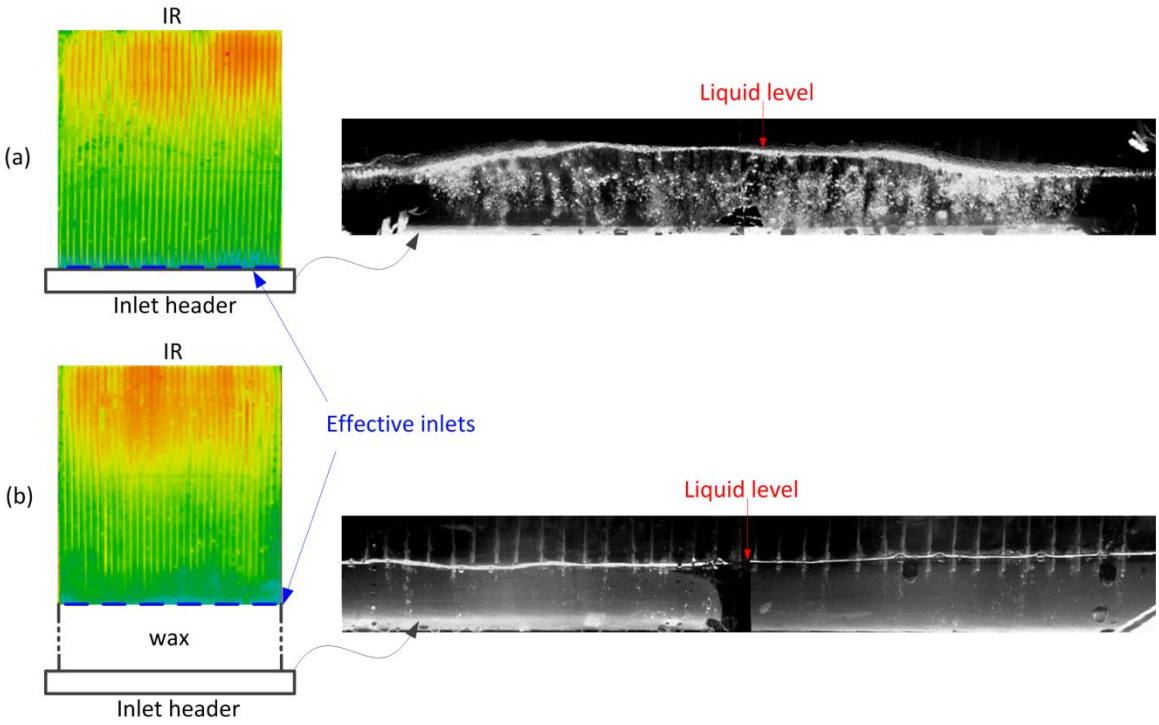


Figure 7-7 Infrared images of both heat exchangers and the corresponding flow regimes in the inlet headers under FGB mode (a) heat exchanger without inlet restriction (b) heat exchanger with inlet restriction

In FGB mode, the comparison between the two heat exchangers is more fair, since the two "effective channel inlets" share the same condition that all reversed vapor has to go through the "effective channel inlets" again. The capacities and UA of both heat exchangers are summarized in Figure 7-8 and Figure 7-9. Two similar trends are observed: 1) the capacity and UA of the heat exchanger with inlet restriction are consistently smaller than those of the heat exchanger without inlet restriction, 2) as superheat rises, the capacity and UA differences between the two heat exchanger increase (although the amount of flow reversal is immeasurable in the FGB case, a similar phenomenon as shown in Figure 7-3 can be anticipated). Both trends are evidence to

support that boiling instability and flow reversal help to enhance heat transfer performance.

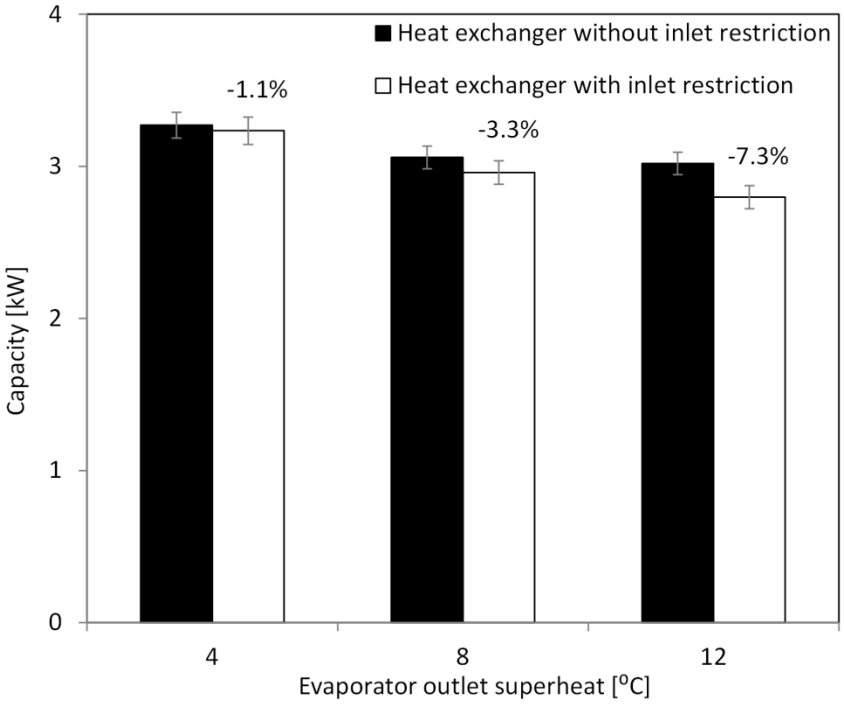


Figure 7-8 Capacity comparison under FGB mode of both heat exchangers indicates that periodic flow reversal enhances cooling capacity

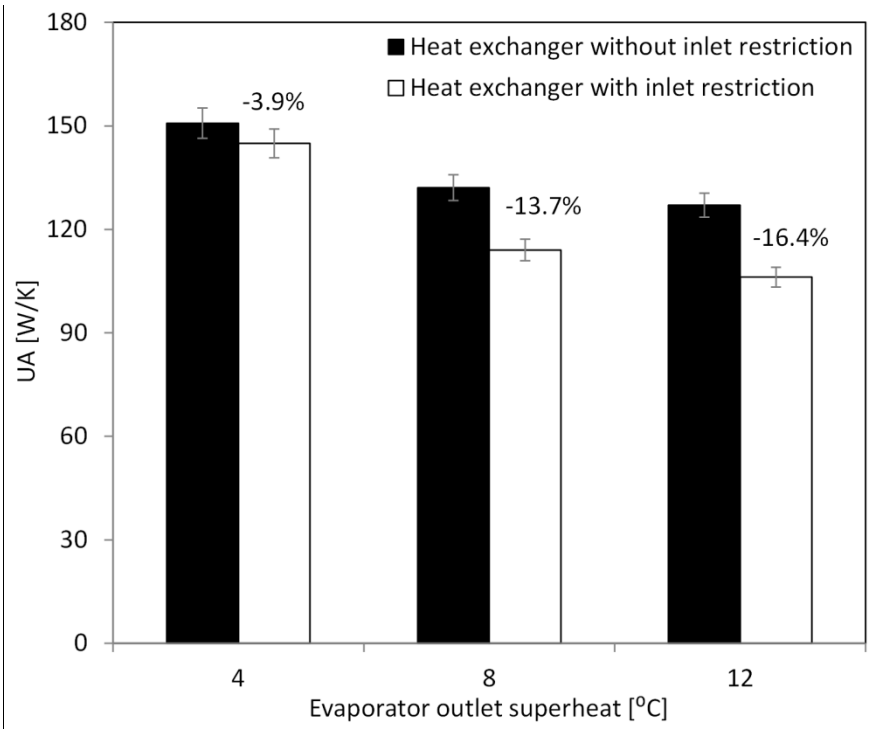


Figure 7-9 UA comparison under FGB mode of both heat exchangers indicates that periodic flow reversal enhances refrigerant side heat transfer coefficient

## 7.4 SIMULATION RESULTS

Numerical simulations are carried out for both heat exchangers under the same condition as listed in Table 7-2 (except superheat). Since the distributions in both heat exchangers are quite uniform as reflected in Figure 7-2 by the IR images, the flow condition in each microchannel is assumed to be identical. In that case, the single channel simulation is expected to represent the behavior of the whole heat exchanger. Since the experimental mass fluxes in both heat exchangers under FGBR mode are around 107 kg/m$^2$/s at 4 ℃ superheat, a slightly higher value (113 kg/m$^2$/s) is employed for both heat exchangers to ensure 0 ℃ superheat (assumption 6 in Chapter 4.3.1). The pressure drop across each channel is adjusted so that the mass flux in that channel meets the target. The

idea is to fix mass flux and air side conditions for both heat exchangers, and see which one has higher refrigerant side heat transfer coefficient, thus higher capacity.

Figure 7-10 shows the flow regime development within one periodic cycle in the two heat exchangers. For the heat exchanger with inlet restriction, only the effective heat transfer region is covered (from 0.32 m to 0.51 m). Blue lines and red lines are used to track the locations of the upstream and downstream edge of each vapor slug in time. A schematic of the in-tube flow regime is employed (also shown on the left side of Figure 7-10) to illustrate the physical interpretation of the red and blue lines. It can be clearly seen from the flow regimes that flow reversal is much more likely to happen in the heat exchanger without inlet restriction. As is indicated by the length of the x axis in Figure 7-10, due to more drastic bubble expansions, the duration of each flow cycle in the heat exchanger without inlet restriction is only half of that in the heat exchanger with inlet restriction. Simulation results show that there are 5.7% and 0.0% of vapor flow reversal in the heat exchanger without and with inlet restriction respectively, which are reasonably close to the experimental results (5.4% and 1.0% as shown in Figure 7-3) at the lowest superheat (4 ℃). The velocity developments in both heat exchangers are demonstrated in Figure 7-11. The velocities at three geometrical locations (10%, 50% and 90% of the channel length) are selected. In both channels, velocity increases from the upstream to the downstream due to continuous evaporation. In the heat exchanger without inlet restriction, because of higher intensity of flow reversal, velocities at all selected locations oscillate, while in the heat exchanger with inlet restriction, velocity at each location is relatively stable. Since the mass flux in both heat exchangers is kept the same, the in-time average of each velocity is nearly the same in both heat exchangers.

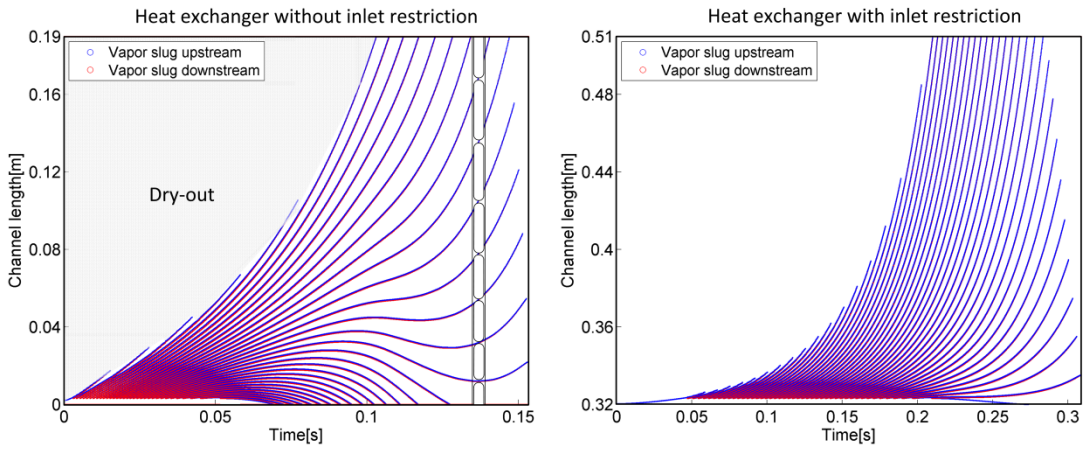


Figure 7-10 Flow regimes development within one periodic cycle in two heat exchangers

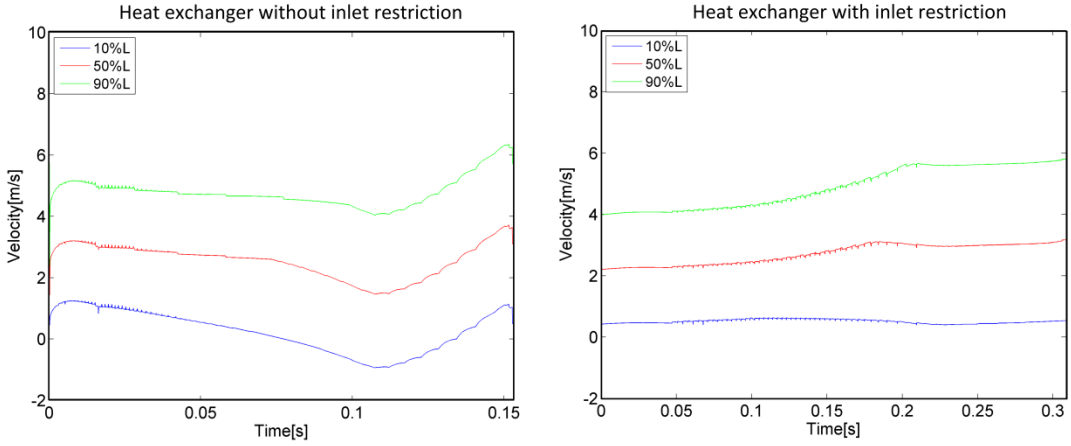


Figure 7-11 Velocity development within one periodic cycle in two heat exchangers

The refrigerant side heat transfer coefficient development at three selected locations in both heat exchangers is illustrated in Figure 7-12. At the beginning of each cycle, liquid flows into the empty channel. One location is considered in dry-out state if the first liquid slug hasn't passed that location yet. The dry-out region inside of a channel shrinks as liquid proceeds to the downstream, which is demonstrated by the shaded area in Figure 7-10 (left side). Within the dry-out region, refrigerant side heat transfer coefficient is calculated in the following way: 5% of the entire dry-out area is covered with liquid film where the heat transfer coefficient is the same as in the vapor slug, while the rest of the

area is covered with vapor where the heat transfer coefficient is calculated using single phase correlations (Incropera and DeWitt (2002) and Gnielinski (1976)). The heat transfer coefficient in the dry-out region is calculated using equation 7-1.

$$HTC_{dry-out} = 95\% HTC_{vapor} + 5\% HTC_{vapor-slug} \quad (7\text{-}1)$$

The assumption that liquid film always attaches on the wall has to be discarded in the dry-out region; otherwise unreasonably high heat transfer performance will be obtained. The dry-out ratio (95%) is determined based on the best matching with the experimental capacity data. This assumption creates discontinuities in velocities and heat transfer coefficients: at the end of each cycle, the channel core is filled with vapor and the wall is covered with thin liquid film, the velocities and heat transfer coefficients are normally the highest during the entire cycle; while at the beginning of each cycle, the heat transfer coefficients decrease dramatically due to large portion of dry-out (95%), and the velocities decrease as well due to less heat input. These discontinuities can be eliminated by modeling the dry-out process in a gradual and smooth way, and this modeling approach is still under development by the author. In Figure 7-12, the sharp jumps of heat transfer coefficients indicate the end of dry-out at each selected location. The dips and spikes of the heat transfer coefficient reflect the alternation of liquid and vapor slugs in time. In the heat exchanger without inlet restriction, along with the oscillation of velocities, the heat transfer coefficients are also oscillatory; while in the heat exchanger with inlet restriction, each heat transfer coefficient stays rather steady in the non-dry-out region. In Figure 7-13, the local heat transfer coefficients are averaged over one periodic cycle and plotted against the normalized channel length (only the heat transfer region) for

both heat exchangers. It can be seen that the major improvement of heat transfer comes from the very upstream region of a channel. Within that region in the heat exchanger with inlet restriction, fluid velocity is constantly below 0.5m/s. Due to the small velocity, the fluid stays in the laminar region and has very low heat transfer coefficient. Within the same region inside of the heat exchanger without inlet restriction, due to the high intensity of periodic flow reversal, the velocity oscillates between ±1 m/s. Larger oscillation of velocity ends the dry-out quicker and forces more fluid to enter the turbulent region. As a result, heat transfer coefficient is enhanced. Based on the heat transfer coefficient results in time, the cooling capacities at each time can be calculated. These transient capacities of both heat exchangers are shown in Figure 7-14. Corresponding to the heat transfer characteristic shown in Figure 7-12 and Figure 7-13, the major capacity improvement is achieved at the upstream end where fluid velocity is relatively low. The average capacity of the heat exchanger with inlet restriction is 3.09 kW which is 4.6% lower than the capacity (3.24kW) of the heat exchanger without inlet restriction. Revisiting Figure 7-4, the capacities of both heat exchangers under FGBR mode at the lowest superheat are 3.27 kW (without inlet restriction) and 3.13 kW (with inlet restriction), respectively. Simulated capacities match with the experimental results fairly accurately.

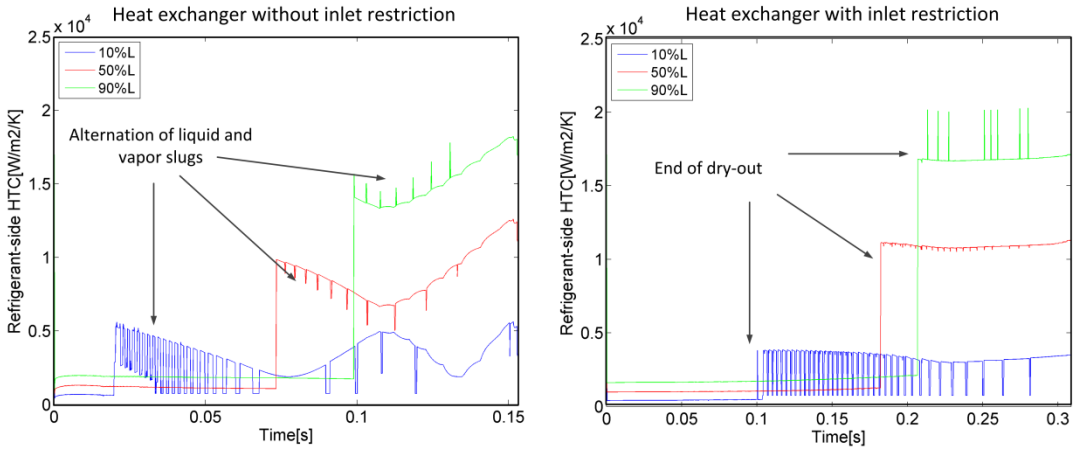


Figure 7-12 Refrigerant side heat transfer coefficient development within one periodic cycle in two heat exchangers

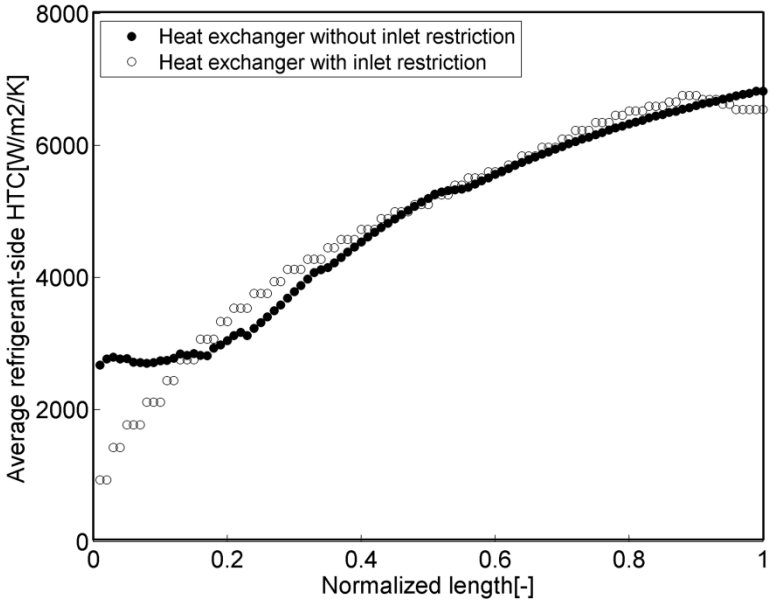


Figure 7-13 Refrigerant side heat transfer coefficient is enhanced by boiling instability especially at the low velocity region

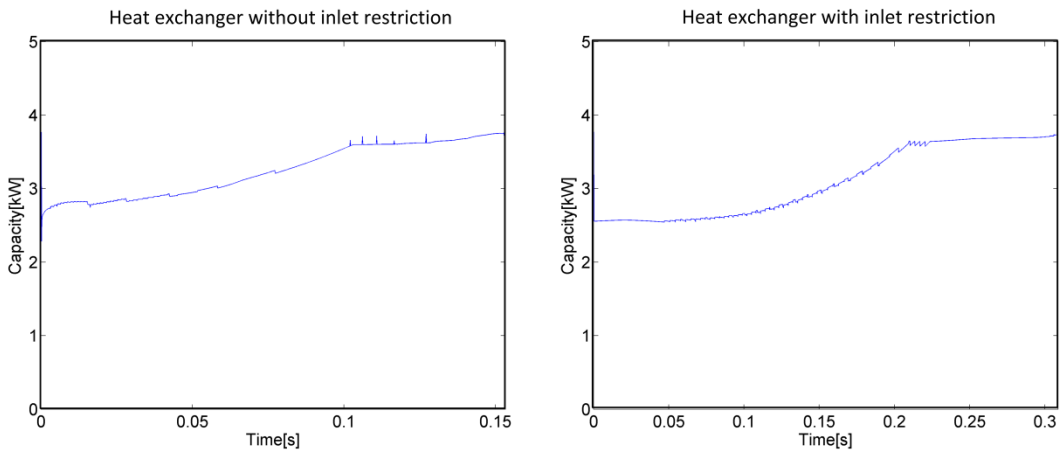


Figure 7-14 Transient capacities within one periodic cycle of two heat exchangers

## 7.5 SUMMARY AND CONCLUSIONS

This chapter presents the effect of boiling instability on the heat transfer performance of a microchannel evaporator. Two heat exchangers with identical geometries in the heat transfer areas are employed and an artificial upstream flow resistance is added for one of them. The heat exchanger without artificial flow resistance is subject to more severe boiling instability and consequently generates four times more reverse flow than the other one (measured in FGBR mode). It has been demonstrated that high boiling instability helps to improve heat exchanger UA and cooling capacity in both FGB and FGBR mode.

Numerical simulations of bubble dynamics coupled with heat transfer are also carried out for both heat exchangers. Results demonstrate that in the heat exchanger with higher boiling instability, the refrigerant side heat transfer coefficients oscillate periodically which is synchronized with the velocity oscillation. The velocity oscillation turns out to

enhance heat transfer especially in the upstream part of the channel by ending dryout sooner and pushing more flow into the turbulent region.

# Chapter 8 CONTRIBUTIONS AND RECOMMENDED FUTURE WORK

## 8.1 CONTRIBUTIONS OF THIS RESEARCH

Majority of the previous research on boiling instabilities and flow reversal focused on electronic cooling applications. Since the working fluids, operating conditions and material of microchannel evaporators used in air conditioning systems are significantly different from those of microchannel heat sinks used for electronics cooling, the goal of this dissertation is to present a comprehensive study of reverse flow in microchannel evaporators as a part of an air conditioning system.

Flow regimes inside of an aluminum microchannel which is a part of an operating microchannel evaporator have been visualized for the first time in the literature. When two-phase refrigerant is fed into the microchannel (DX mode), churn flow, bubbly/slug flow and annular flow occur alternatively with variable duration. Flow reversal is witnessed occasionally and only in bubbly/slug flow regime. When only liquid refrigerant is supplied into the microchannel (FGBR mode), forward flow and reverse flow alternate periodically and reverse flow occupies more than one third of the cycle time.

A mechanistic model which is capable of simulating multiple-bubble dynamics has been developed and validated by visualization results. This model can be used to explain the mechanism of reverse flow in microchannels: at the beginning of a cycle, fresh liquid refrigerant enters a channel filled with vapor; liquid accelerates in the channel due to smaller downstream resistance; rapid expansion of vapor slugs accelerates the

downstream fluid, which increases the downstream frictional resistance; as downstream resistance continues to build up, the highest pressure in the channel gradually propagates from the inlet to downstream, and the resulting positive pressure gradient causes the flow reversal; after continuous evaporation and depletion of working fluid from both inlet and outlet, the downstream resistance decreases and fresh liquid enters the empty tube again to start a new cycle. The model demonstrates that the expansion rate of vapor slugs is the driving force of the reverse flow and it depends on heat flux, channel geometry (mainly D and L) and refrigerant thermophysical properties (mainly $v_{fg}$ and $h_{fg}$).

The effect of channel geometry (D and L) on flow reversal in microchannel evaporators has been investigated experimentally (fixed heat flux and superheat). It has been found that smaller channel diameter and shorter channel length result in more reversed vapor flow at a higher frequency. The experimental results validate the model prediction (quantitatively for the prediction of the flow rate of reversed vapor and qualitatively for the frequency). Simulation demonstrates that smaller channel diameter creates more rapid growth of vapor slugs and allocates more flow resistance to the downstream. As a result, the incoming flow is quickly decelerated and the positive pressure gradient ends up covering larger upstream areas. Simulation also shows that there is relatively greater buildup of upstream resistance due to a higher refrigerant velocity in the longer channel, especially at the beginning of a periodic cycle when large dryout area exists.

The effect of refrigerant thermophysical properties ($v_{fg}$ and $h_{fg}$) on flow reversal in microchannel evaporators has been investigated experimentally (fixed heat flux and superheat). Experiments with R134a and R245fa show that the refrigerant with higher

specific volume difference induces more flow reversal. Experiments using R134a, R1234yf and R32 demonstrate that increasing heat of vaporization reduces the flow rate of the reversed vapor, but when normalizing this flow rate by the mass flow rate of supplied refrigerant, it becomes insensitive to heat of vaporization. Frequency of flow reversal increases as the heat of vaporization of the refrigerant decreases. The experimental results validate the model prediction (quantitatively for the prediction of the flow rate of reversed vapor and qualitatively for the frequency (except for the pair of R134a and R245fa)). Simulations demonstrate that higher specific volume difference creates faster growth of vapor slugs and allocates more flow resistance to the downstream section. As a result, more incoming flow is reversed. Simulations also show that the ratio of flow rate of reversed vapor and mass flow rate of the supplied liquid is not a strong function of heat of vaporization because the effects of heat of vaporization on both flow rates have similar magnitude.

The effect of reverse flow on the heat transfer performance of microchannel evaporators has been investigated experimentally and numerically. Two heat exchangers with identical geometries in the heat transfer areas are used and an artificial upstream flow resistance is added to one of them. Distributions in both heat exchangers are kept nearly uniform, thus will not contribute to the difference of heat transfer performance between these two heat exchangers. The heat exchanger without artificial flow resistance is subject to more severe boiling instability and consequently generates four times more reverse flow than the other one (measured in FGBR mode). It has been demonstrated that high boiling instability helps to improve heat exchanger UA (up to 25%) and cooling capacity (up to 13%) in both FGB and FGBR mode. Numerical simulations reveal that

the velocity oscillation in the heat exchanger without inlet restriction turns out to enhance heat transfer especially in the upstream part of the channel by ending dryout sooner and pushing more flow into the turbulent region.

## 8.2 RECOMMENDED FUTURE WORK

It is recommended that future work on this topic should be extended to microchannel evaporators with horizontal tubes and vertical headers, which is normally used in a reversible air conditioning and heat pump system. Reverse flow in this evaporator configuration might be more detrimental compared with the evaporator orientation examined in this research. As shown in Figure 8-1, the reversed vapor will always accumulate in the top portion of the inlet header, obstructing the liquid feeding to the microchannels in that region. In this case, reducing the amount of reduced vapor might substantially improve refrigerant distribution thus the heat transfer performance of the evaporator.

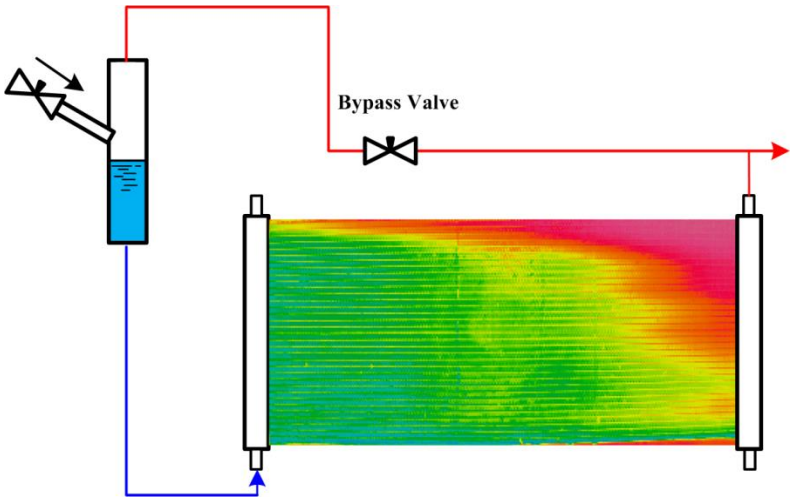


Figure 8-1 Reversed vapor obstructs liquid feeding to the microchannels in the top portion of the evaporator (FGB mode)

On the simulation side, coupling pressure oscillation in the inlet header with the pressure at the channel inlet is recommended. Accounting for the compressible volume in the inlet header in the model is expected to significantly improve the prediction accuracy especially for the frequency of reverse flow. How to handle the non-synchronized flow reversal from hundreds of parallel microchannels might be a difficult part of the model. Visualization in this research along with the visualization made by Tuo and Hrnjak indicate high level of synchronization of reverse flow from different channels but only qualitatively. Other possible improvements of the model are followings: 1) model the mass transfer from both the liquid bridge and the liquid film, 2) model the liquid film thinning and depletion process, in order to simulate dry-out and superheat effect, 3) include thermal mass of the wall in the model, 4) investigate the effect of conditions of the channel surface, surface tension and viscosity on flow reversal.

# REFERENCES


Ablanque, N., Oliet, C., Rigola, J., Perez-Segarra, C. D., & Oliva, A. (2010). Two-phase flow distribution in multiple parallel tubes. International Journal of Thermal Sciences, 49(6), 909-921.

Abiev, R. S. (2011). Modeling of pressure losses for the slug flow of a gas–liquid mixture in mini-and microchannels. Theoretical Foundations of Chemical Engineering, 45(2), 156.

Agostini, B., Revellin, R., & Thome, J. R. (2008). Elongated bubbles in microchannels. Part I: Experimental study and modeling of elongated bubble velocity. International Journal of Multiphase Flow, 34(6), 590–601. doi:10.1016/j.ijmultiphaseflow.2007.07.007

Ahmad, M., Berthoud, G., & Mercier, P. (2009). General characteristics of two-phase flow distribution in a compact heat exchanger. International Journal of Heat and Mass Transfer, 52(1), 442-450.

Akbar, M.K., Plummer, D.A. & Ghiaasiaan, S.M. (2003). On gas–liquid two-phase flow regimes in microchannels. International Journal of Multiphase Flow, 29 (5), 855–865.

Balasubramanian, P., & Kandlikar, S. G. (2005). Experimental study of flow patterns, pressure drop, and flow instabilities in parallel rectangular minichannels. Heat Transfer Engineering, 26(3), 20-27.

Barber, J., Brutin, D., Sefiane, K., Gardarein, J. L., & Tadrist, L. (2011). Unsteady-state fluctuations analysis during bubble growth in a “rectangular” microchannel. International Journal of Heat and Mass Transfer, 54(23), 4784-4795.

Beaver, A.C., Yin, J., Bullard, C.W., & Hrnjak, P.S. (1999). An experimental investigation of transcritical carbon dioxide systems for residential air-conditioning. ACRC Report CR-18, University of Illinois at Urbana-Champaign

Belmares, M., Park, Y., Hydrodynamic Modeling of Flow Reversal in Micro-channel Flow Boiling, In: Int. Refrig. and Air Conf. at Purdue (2014), No. 2383.

Bergles, A. E., & Kandlikar, S. G. (2005). On the Nature of Critical Heat Flux in Microchannels. Journal of Heat Transfer, 127(1), 101. doi:10.1115/1.1839587

Bogojevic, D., Sefiane, K., Duursma, G., & Walton, A. J. (2013). Bubble dynamics and flow boiling instabilities in microchannels. International Journal of Heat and Mass Transfer, 58(1), 663-675.

Bowers, C., Wujek, S., and Hrnjak, P., "Quantification of Refrigerant Distribution and Effectiveness in Microchannel Heat Exchangers Using Infrared Thermography" (2010). International Refrigeration and Air Conditioning Conference. Paper 1016.

Brauner, N., & Maron, D. M. (1992). Identification of the range of 'small diameters' conduits, regarding two-phase flow pattern transitions. International Communications in Heat and Mass Transfer, 19(1), 29-39.

Brix, W., Kærn, M. R., & Elmegaard, B. (2009). Modelling refrigerant distribution in microchannel evaporators. International Journal of refrigeration, 32(7), 1736-1743.

Brix, W., Kærn, M. R., & Elmegaard, B. (2010). Modelling distribution of evaporating CO 2 in parallel minichannels. international journal of refrigeration, 33(6), 1086-1094.

Brutin, D. (2003). Ecoulements liquides en microtubes et ébullition convective en minicanaux: étude expérimentale et modélisation (Doctoral dissertation, Université de Provence-Aix-Marseille I).

Brutin, D., & Tadrist, L. (2004). Pressure drop and heat transfer analysis of flow boiling in a minichannel: Influence of the inlet condition on two-phase flow stability. International Journal of Heat and Mass Transfer, 47(10-11), 2365–2377. doi:10.1016/j.ijheatmasstransfer.2003.11.007

Brutin, D., Topin, F., & Tadrist, L. (2003). Experimental study of unsteady convective boiling in heated minichannels. International Journal of Heat and Mass Transfer, 46(16), 2957–2965. doi:10.1016/S0017-9310(03)00093-0

Byun, H. W., & Kim, N. H. (2011). Refrigerant distribution in a parallel flow heat exchanger having vertical headers and heated horizontal tubes. Experimental Thermal and Fluid Science, 35(6), 920-932.

Chang, K. H., & Pan, C. (2007). Two-phase flow instability for boiling in a microchannel heat sink. International journal of heat and mass transfer, 50(11), 2078-2088.

Chen, L., Tian, Y. S., & Karayiannis, T. G. (2006). The effect of tube diameter on vertical two-phase flow regimes in small tubes. International Journal of Heat and Mass Transfer, 49, 4220–4230. doi:10.1016/j.ijheatmasstransfer.2006.03.025

Chen, T., & Garimella, S. V. (2006). Measurements and high-speed visualizations of flow boiling of a dielectric fluid in a silicon microchannel heat sink. International Journal of Multiphase Flow, 32(8), 957–971. doi:10.1016/j.ijmultiphaseflow.2006.03.002

Chen, T., & Garimella, S. V. (2011). Local heat transfer distribution and effect of instabilities during flow boiling in a silicon microchannel heat sink. International Journal of Heat and Mass Transfer, 54(15), 3179-3190.

Consolini, L., & Thome, J. R. (2009). Micro-channel flow boiling heat transfer of R-134a, R-236fa, and R-245fa. Microfluidics and nanofluidics, 6(6), 731-746.

Churchill, S. W. (1977). Friction-factor equation spans all fluid-flow regimes. Chemical engineering, 84(24), 91-92.

Elbel, S.W., & Hrnjak, P.S. (2004). Flash gas bypass for improving the performance of transcritical R744 systems that use microchannel evaporators, Int. J. Refrigeration, 27(7): 724-735. doi:10.1016/j.ijrefrig.2004.07.019

Field, B. S., & Hrnjak, P. (2011, January). A mechanistic model of two-phase pressure drop in microchannels. In ASME 2011 International Mechanical Engineering Congress and Exposition (pp. 411-419). American Society of Mechanical Engineers.

Gedupudi, S. , Kenning, D.B.R, & Karayiannis, T.G.(2014). Flow boiling in rectangular microchannels: 1-D modelling of the influence of inlet resistance on flow reversal, in: 4th Micro and Nano Flows Conference, UCL, London, UK, 7–10 September, 2014.

Gedupudi, S., Zu, Y. Q., Karayiannis, T. G., Kenning, D. B. R., & Yan, Y. Y. (2011). Confined bubble growth during flow boiling in a mini/micro-channel of rectangular cross-section Part I:

Experiments and 1-D modelling. International Journal of Thermal Sciences, 50(3), 250–266. doi:10.1016/j.ijthermalsci.2010.09.001

Gnielinski, V. (1976). New equations for heat and mass-transfer in turbulent pipe and channel flow. International chemical engineering, 16(2), 359-368.

Harirchian, T., & Garimella, S. V. (2008). Microchannel size effects on local flow boiling heat transfer to a dielectric fluid. International Journal of Heat and Mass Transfer, 51(15-16), 3724–3735. doi:10.1016/j.ijheatmasstransfer.2008.03.013

He, H., Li, P. F., Yan, R. G., & Pan, L. M. (2016). Modeling of reversal flow and pressure fluctuation in rectangular microchannel. International Journal of Heat and Mass Transfer, 102, 1024-1033.

Hetsroni, G., Mosyak, A., Pogrebnyak, E., & Segal, Z. (2005). Explosive boiling of water in parallel micro-channels. International Journal of Multiphase Flow, 31(4), 371–392. doi:10.1016/j.ijmultiphaseflow.2005.01.003

Hetsroni, G., Mosyak, A., Pogrebnyak, E., & Segal, Z. (2006). Periodic boiling in parallel micro-channels at low vapor quality. International Journal of Multiphase Flow, 32(10-11), 1141–1159. doi:10.1016/j.ijmultiphaseflow.2006.06.005

Hrnjak, P. (2004). Developing adiabatic two phase flow in headers—distribution issue in parallel flow microchannel heat exchangers. Heat Transfer Engineering, 25(3), 61-68.

Huh, C., Kim, J., & Kim, M. H. (2007). Flow pattern transition instability during flow boiling in a single microchannel. International Journal of Heat and Mass Transfer, 50(5-6), 1049–1060. doi:10.1016/j.ijheatmasstransfer.2006.07.027

Hwang, S. T., Soliman, H. M., & Lahey, R. T. (1988). Phase separation in dividing two-phase flows. International journal of multiphase flow, 14(4), 439-458.

Hwang, Y., Jin, D. H., & Radermacher, R. (2007). Refrigerant distribution in minichannel evaporator manifolds. HVAC&R Research, 13(4), 543-555.

Idelehik, I.E. (1994). Handbook of Hydraulic Resistance, 3rd Ed, Chaps 3 and 4. CRC Press, Florida.

Incropera, Frank P.; DeWitt, David P. (2002). Fundamentals of Heat and Mass Transfer (5th ed.). Hoboken: Wiley. pp. 486, 487.

Kandlikar, S. G. (2005). High flux heat removal with microchannels—a roadmap of challenges and opportunities. Heat Transfer Engineering, 26(8), 5-14.

Kandlikar, S. G., Kuan, W. K., Willistein, D. A., & Borrelli, J. (2006). Stabilization of flow boiling in microchannels using pressure drop elements and fabricated nucleation sites. Journal of Heat Transfer, 128(4), 389-396.

Kandlikar, S. G. (2003, January). Microchannels and minichannels: history, terminology, classification and current research needs. In ASME 2003 1st International Conference on Microchannels and Minichannels (pp. 1-6). American Society of Mechanical Engineers.

Karayiannis, T. G., & Mahmoud, M. M. (2016). Flow boiling in microchannels: Fundamentals and applications. Applied Thermal Engineering.

Karayiannis, T.G., Shiferaw, D., Kenning, D.B.R., Saturated flow boiling in small to micro-diameter metallic tubes: experimental results and modelling, in: ECI International Conference on Heat Transfer and Fluid Flow in Microscale, Whistler, 21e26 September 2008.

Kattan, Nakhlé, J. R. Thome, and D. Favrat. "Flow boiling in horizontal tubes: part 3—development of a new heat transfer model based on flow pattern." Journal of Heat Transfer 120.1 (1998): 156-165.

Kenning, D. B. R., Wen, D. S., Das, K. S., & Wilson, S. K. (2006). Confined growth of a vapour bubble in a capillary tube at initially uniform superheat: Experiments and modelling. International Journal of Heat and Mass Transfer, 49(23-24), 4653–4671. doi:10.1016/j.ijheatmasstransfer.2006.04.010

Kew, P. A., & Cornwell, K. (1997). Correlations for the prediction of boiling heat transfer in small-diameter channels. Applied Thermal Engineering, 17(8), 705-715.

Khovalyg, D., Hrnjak, P. S., & Jacobi, A. M. (2015). Interactions Between Parallel Unevenly Heated Minichannels During Flow Boiling Of R134A. Heat Transfer Engineering, 7632(October), 1–57. doi:10.1080/01457632.2015.1097954

Kim, Man-Hoe, and C. W. Bullard. "Air-side thermal hydraulic performance of multi-louvered fin aluminum heat exchangers." International journal of refrigeration 25.3 (2002): 390-400.

Koşar, Ali, Chih-Jung Kuo, and Yoav Peles. "Suppression of boiling flow oscillations in parallel microchannels by inlet restrictors." Journal of Heat Transfer 128.3 (2006): 251-260.

Kulkarni, T., Bullard, C. W., and Cho, K. (2004). Header design tradeoffs in microchannel evaporators. Applied Thermal Engineering, 24(5), 759-776.

Kuan, W. K., & Kandlikar, S. G. (2007). Experimental study on the effect of stabilization on flow boiling heat transfer in microchannels. Heat Transfer Engineering, 28(8-9), 746-752.

Kuang, Y. W., Wang, W., Miao, J. Y., Yu, X. G., Zhang, H. X., & Zhuan, R. (2017). Flow boiling of ammonia and flow instabilities in mini-channels. Applied Thermal Engineering, 113, 831-842.

Kuo, C.-J., & Peles, Y. (2008). Flow Boiling Instabilities in Microchannels and Means for Mitigation by Reentrant Cavities. Journal of Heat Transfer, 130(7), 72402. doi:10.1115/1.2908431

Kuo, C. J., & Peles, Y. (2009). Pressure effects on flow boiling instabilities in parallel microchannels. International Journal of Heat and Mass Transfer, 52(1), 271-280.

Lee, J. K., & Lee, S. Y. (2004). Distribution of two-phase annular flow at header–channel junctions. Experimental thermal and fluid science, 28(2), 217-222.

Lee, J., & Mudawar, I. (2005). Two-phase flow in high-heat-flux micro-channel heat sink for refrigeration cooling applications: Part I—pressure drop characteristics. International Journal of Heat and Mass

Lee, S., & Mudawar, I. (2016). Investigation of flow boiling in large micro-channel heat exchangers in a refrigeration loop for space applications. International Journal of Heat and Mass Transfer, 97, 110-129.

Li, H., & Hrnjak, P. (2013). Effect of lubricant on two-phase refrigerant distribution in microchannel evaporator. SAE International Journal of Materials and Manufacturing, 6(2013-01-1508), 567-575.

Li, H., & Hrnjak, P. (2014a). Lubricant effect on performance of R134a MAC microchannel evaporators (No. 2014-01-0692). SAE Technical Paper.

Li, H., & Hrnjak, P. (2014b). Effect of flow regime in the horizontal inlet header on refrigerant-oil mixture distribution in a MAC microchannel evaporator (No. 2014-01-0701). SAE Technical Paper.

Li, H., & Hrnjak, P. (2015a). Quantification of liquid refrigerant distribution in parallel flow microchannel heat exchanger using infrared thermography. Applied Thermal Engineering, 78, 410-418.

Li, H., & Hrnjak, P. (2015b). An experimentally validated model for microchannel heat exchanger incorporating lubricant effect. International journal of refrigeration, 59, 259-268.

Li, H., & Hrnjak, P. (2017). Modeling of bubble dynamics in single diabatic microchannel. International Journal of Heat and Mass Transfer, 107, 96-104.

M.S. Plesset, S.A. Zwick, The growth of a vapor bubble in superheated liquid, J. Appl. Phys. 25 (1954) 493–501.

Mikic, B.B., & Rohsenow, W.M. (1969). Bubble growth rates in non-uniform temperature field, Progress in Heat and Mass Transfer, 2, 283-292.

Niño, V. G., Hrnjak, P. S., & Newell, T. A. (2003). Two-phase flow visualization of R134A in a multiport microchannel tube. Heat Transfer Engineering, 24(1), 41-52.

Prajapati, Y. K., Pathak, M., & Kaleem Khan, M. (2015). A comparative study of flow boiling heat transfer in three different configurations of microchannels. International Journal of Heat and Mass Transfer, 85, 711–722. doi:10.1016/j.ijheatmasstransfer.2015.02.016

Prajapati, Y. K., Pathak, M., & Khan, M. K. (2017). Bubble dynamics and flow boiling characteristics in three different microchannel configurations. International Journal of Thermal Sciences, 112, 371-382.

Qu, W., & Mudawar, I. (2004). Transport Phenomena in Two-Phase Micro-Channel Heat Sinks. Journal of Electronic Packaging, 126(2), 213. doi:10.1115/1.1756145

Revellin, R., & Thome, J. R. (2007). A new type of diabatic flow pattern map for boiling heat transfer in microchannels. Journal of Micromechanics and Microengineering, 17, 788–796. doi:10.1088/0960-1317/17/4/016

Revellin, R., Agostini, B., & Thome, J. R. (2008). Elongated bubbles in microchannels. Part II: Experimental study and modeling of bubble collisions. International Journal of Multiphase Flow, 34, 602–613. doi:10.1016/j.ijmultiphaseflow.2007.07.006

Szczukiewicz, S., Borhani, N., & Thome, J. R. (2013). Two-phase heat transfer and high-speed visualization of refrigerant flows in 100× 100 μm 2 silicon multi-microchannels. International Journal of Refrigeration, 36(2), 402-413.

Tadrist, L. (2007). Review on two-phase flow instabilities in narrow spaces. International Journal of Heat and fluid flow, 28(1), 54-62.

Thome, J. R., Dupont, V., & Jacobi, a. M. (2004). Heat transfer model for evaporation in microchannels. Part I: presentation of the model. International Journal of Heat and Mass Transfer, 47(14-16), 3375–3385. doi:10.1016/j.ijheatmasstransfer.2004.01.006

Triplett, K. A., Ghiaasiaan, S. M., Abdel-Khalik, S. I., & Sadowski, D. L. (1999). Gas–liquid two-phase flow in microchannels Part I: two-phase flow patterns. International Journal of Multiphase Flow, 25(3), 377-394.

Tuo, H., & Hrnjak, P. (2013a). Periodical reverse flow and boiling fluctuations in a microchannel evaporator of an air-conditioning system. International Journal of Refrigeration, 36(4), 1263–1275. doi:10.1016/j.ijrefrig.2013.02.001

Tuo, H., & Hrnjak, P. (2013b). New approach to improve performance by venting periodic reverse vapor flow in microchannel evaporator. International Journal of Refrigeration, 36(8), 2187–2195. doi:10.1016/j.ijrefrig.2013.05.020

Tuo, H., & Hrnjak, P. (2013c). Effect of the header pressure drop induced flow maldistribution on the microchannel evaporator performance. international journal of refrigeration, 36(8), 2176-2186.

Tuo, H., & Hrnjak, P. (2014a). Visualization and measurement of periodic reverse flow and boiling fluctuations in a microchannel evaporator of an air-conditioning system. International Journal of Heat and Mass Transfer, 71, 639–652. doi:10.1016/j.ijheatmasstransfer.2013.10.024

Tuo, H., & Hrnjak, P. (2014b). Effect of venting the periodic reverse vapor flow on the performance of a microchannel evaporator in air-conditioning systems. International Journal of Heat and Mass Transfer, 69, 66-76.

Veziroglu, T. N., & Lee, S. S. (1969, September). Boiling flow instabilities in parallel channels. In Proceedings of the Institution of Mechanical Engineers, Conference Proceedings (Vol. 184, No. 3, pp. 7-17). SAGE Publications.

Vist, S., & Pettersen, J. (2004). Two-phase flow distribution in compact heat exchanger manifolds. Experimental thermal and fluid science, 28(2), 209-215.

Wang, G., Cheng, P., & Bergles, A. E. (2008). Effects of inlet/outlet configurations on flow boiling instability in parallel microchannels. International Journal of Heat and Mass Transfer, 51(9), 2267-2281.

Wu, H. Y., & Cheng, P. (2003). Visualization and measurements of periodic boiling in silicon microchannels. International Journal of Heat and Mass Transfer, 46(14), 2603–2614. doi:10.1016/S0017-9310(03)00039-5

Wu, H. Y., & Cheng, P. (2004). Boiling instability in parallel silicon microchannels at different heat flux. International Journal of Heat and Mass Transfer, 47(17-18), 3631–3641. doi:10.1016/j.ijheatmasstransfer.2004.04.012

Xu, J., Zhou, J., & Gan, Y. (2005). Static and dynamic flow instability of a parallel microchannel heat sink at high heat fluxes. Energy Conversion and Management, 46(2), 313-334.

Xu, J., Shen, S., Gan, Y., Li, Y., Zhang, W., & Su, Q. (2005). Transient flow pattern based microscale boiling heat transfer mechanisms. Journal of Micromechanics and Microengineering, 15(6), 1344.

Zhang, T., Tong, T., Chang, J. Y., Peles, Y., Prasher, R., Jensen, M. K., … Phelan, P. (2009). Ledinegg instability in microchannels. International Journal of Heat and Mass Transfer, 52(25-26), 5661–5674. doi:10.1016/j.ijheatmasstransfer.2009.09.008

Zou, Y., & Hrnjak, P. S. (2013a). Experiment and visualization on R134a upward flow in the vertical header of microchannel heat exchanger and its effect on distribution. International Journal of Heat and Mass Transfer, 62, 124-134.

Zou, Y., & Hrnjak, P. S. (2013b). Refrigerant distribution in the vertical header of the microchannel heat exchanger–measurement and visualization of R410A flow. international journal of refrigeration, 36(8), 2196-2208.

Zou, Y., Li, H., & Hrnjak, P. (2014). Lubricant impact on R134a distribution and microchannel heat exchanger performance (No. 2014-01-0706). SAE Technical Paper.